INFORMATION TO USERS

This manuscript has been reproduced from the microfilm master. UMI films the text directly from the original or copy submitted. Thus, some thesis and dissertation copies are in typewriter face, while others may be from any type of computer printer.

The quality of this reproduction is dependent upon the quality of the copy submitted. Broken or indistinct print, colored or poor quality illustrations and photographs, print bleedthrough, substandard margins, and improper alignment can adversely affect reproduction.

In the unlikely event that the author did not send UMI a complete manuscript and there are missing pages, these will be noted. Also, if unauthorized copyright material had to be removed, a note will indicate the deletion.

Oversize materials (e.g., maps, drawings, charts) are reproduced by sectioning the original, beginning at the upper left-hand corner and continuing from left to right in equal sections with small overlaps. Each original is also photographed in one exposure and is included in reduced form at the back of the book.

Photographs included in the original manuscript have been reproduced xerographically in this copy. Higher quality 6" x 9" black and white photographic prints are available for any photographs or illustrations appearing in this copy for an additional charge. Contact UMI directly to order.

UMI

A Bell & Howell Information Company
300 North Zeeb Road, Ann Arbor MI 48106-1346 USA
313/761-4700 800/521-0600

LOW-NOISE RECEIVERS, MICROMACHINED ANTENNAS AND LOW-LOSS TRANSITIONS FOR MILLIMETER-WAVE APPLICATIONS

by

Gildas Gauthier

A dissertation submitted in partial fulfillment
of the requirements for the degree of
Doctor of Philosophy
(Electrical Engineering)
in The University of Michigan
1999

Doctoral Committee:

Professor Gabriel M. Rebeiz, Chairperson
Research Scientist Jack R. East
Professor Linda P.B. Katehi
Associate Professor Kamal Sarabandi
Associate Professor Kim A. Winick

To my family

ACKNOWLEDGEMENTS

I would like to thank my advisor, Professor Gabriel Rebeiz, who allowed me to start and finish this Ph.D. research. I am would like to thank him for the few hours spent in the streets of Madrid, the bars of Granada and the cafes of Paris. I am thankful to my dissertation committee members Professors Linda Katehi, Kamal Sarabandi and Kim Winick, and Dr. Jack East.

I am very thankful to Daimler Benz, Darpa, Hughes and the Army Research Office for providing the financial support during these five years at the University of Michigan.

I am grateful to everybody from the Radiation Laboratory, faculty, staff and students, and particularly the past and present generations of students who made and are making their way through the TICS Lab and the Radiation Laboratory: Walid Ali-Ahmad, Curtis Ling, Brian Kormanyos, Dan Filipovic and Steve Gearhart, who built up the laboratory from their hands, and for their great help when I first came to Michigan. Special thanks to Tom Budka, may we go canoeing and fishing one more time on Lake Superior. Prof. Sanjay Raman more than greatly contributed to my research. Special thanks also to Tayfun Ozdemir, Andy Brown, Leo DiDomenico, Rashaunda Henderson, Katherine Herrick, Sergio Pacheco, Tom Ellis, Steve Robertson, John Papapolymerou, and to the whole soccer team.

Some people were always present and have become real friends. These words are nothing compared to what we have done together and i hope they know it:

Stéphane "Valerian" Legault, Jean-Pierre "Tintin" et Nancy "Milou" Raskin. Special "Fouloude d'Or" is given to Stéphane Chrétien. The French crowd cocktail will go on shaking on its own with, in order of appearance: Alan Courtay, J.C. Chanteloup, J.O. Plouchart, Gérald Haenning, Anne Sauve, Bernard Bunner, Marie-Anne Descalles, Jérome Guillen, Pierre Blondy, Catherine Bauby, Olivier Boivineau and Jean-Marc Fontaine.

Distant but continuous and sincere support came from overseas: Dominique Snyers and Patrice Coupé and of course my brothers and wives: Pierre-Yves and Marimar, Christian and Caroline.

I dedicate this work to my father, Yves, who fought against illness while I was here, and my mother, Marie-Thérèse, for her presence and strength, and to Sue Hong.

Thank you for being here.

TABLE OF CONTENTS

DEDICATION ii

ACKNOWLEDGEMENTS iii

LIST OF FIGURES viii

LIST OF TABLES xvi

CHAPTER

I. INTRODUCTION 1

1.1 Millimeter-Wave Planar Technologies 2
1.2 Planar Integrated Receivers 6
1.3 Millimeter-Wave Microstrip Antennas 9
1.4 Overview of Thesis 12

II. A PLANAR 90 GHz SCHOTTKY-DIODE MILLIMETER-WAVE RECEIVER 14

2.1 Antenna Design 15
2.2 Receiver Design 18
2.3 Millimeter-Wave Measurements 22
2.4 Conclusion 30

III. A 154 GHz UNIPLANAR SUBHARMONIC SCHOTTKY-DIODE RECEIVER 31

3.1 Double Folded-Slot Antenna 32
3.1.1 Antenna Design 32
3.1.2 70-110 GHz Impedance Measurements 37
3.1.3 90-100 GHz Radiation Patterns Measurements . . . 38
3.2 Receiver Design 39
3.2.1 150 GHz DFS Antenna 39
3.2.2 Diode 41
3.2.3 Mixer Design 42

3.3 Millimeter-Wave Measurements 45
3.3.1 Receiver Fabrication 45
3.3.2 150 GHz Radiation Patterns Measurements 48
3.3.3 140-170 GHz Conversion Loss Measurements 48
3.4 Conclusion 52

IV. MICROSTRIP ANTENNAS ON SYNTHESIZED LOW DIELECTRIC CONSTANT SUBSTRATES 54

4.1 The Micromachining Approach 55
4.2 Quasi-Static Measurements of the Effective Dielectric Constant 56
4.3 Radiation Efficiency Measurements 58
4.3.1 Description of Method 58
4.3.2 RF Chain Design and Calibration 60
4.3.3 Measurement Procedure 61
4.3.4 Radiation Efficiency Prediction: the Quality Factor Approach 67
4.4 Radiation Patterns 72
4.5 Conclusion 72

V. A 94 GHz APERTURE-COUPLED MICROMACHINED MICROSTRIP ANTENNA 73

5.1 Antenna Design 74
5.1.1 Antenna 74
5.1.2 CPW to Microstrip Line Transition 77
5.2 Input Impedance 79
5.3 Radiation Efficiency 83
5.4 Radiation Patterns 86
5.5 Mutual Coupling 88
5.6 Conclusion 91

VI. W-BAND SINGLE LAYER VERTICAL TRANSITIONS . . 95

6.1 W-Band Finite Ground Coplanar Waveguide (fgc) to Microstrip Line Transition 96
6.1.1 Transition Design 97
6.1.2 W-band Measurements 102
6.2 W-band cpw-to-cpw Transition 105
6.2.1 Transition Design 105
6.2.2 W-band Measurements 107
6.3 W-band Microstrip-to-Microstrip Transition 111
6.3.1 Transition Design 111
6.3.2 W-band Measurements 114

6.4 Conclusion 116

VII. CONCLUSIONS AND FUTURE WORK 118

7.1 Conclusions 118
7.2 Future Work 122

APPENDICES 127

BIBLIOGRAPHY 142

LIST OF FIGURES

Figure

1.1 Comparison between coplanar waveguide cpw (a), finite ground coplanar waveguide (b) and microstrip (c) propagation modes. 3

1.2 Block diagram of a typical millimeter-wave front-end transceiver for communication systems. 5

1.3 Surface waves are triggered by total internal reflection of the power radiated above the critical angle for ungrounded substrates (a) and grounded substrates (b). 6

1.4 Sketch of an extended hemispherical dielectric lens (a) and off-axis properties (b). The mains beam is scanned when the antenna is moved off-axis. 7

1.5 Uniplanar cpw-based antennas: double-slot (a), double folded-slot (b) and slot-ring (c). 8

1.6 Various microstrip antenna geometries: microstrip line fed (a), probe fed (b) and aperture-coupled (c). 9

1.7 Surface wave cut-off frequencies for low- ($\epsilon_r = 4$) and high- ($\epsilon_r = 12$) dielectric constant grounded dielectric slab. In both cases, the dominant TM_0 mode has a zero cut-off frequency. 11

1.8 Micromachining fabrication processes based on anisotropic wet etching (a) and reactive ion etching (b). 12

2.1 View of the 90 GHz receiver (a) and layout of the cpw-fed double-slot antenna (b). 16

2.2 Calculated double-slot radiation patterns inside the silicon lens for a slot length of $0.28\lambda_0$ ($0.70\lambda_g$) and a slot separation of $0.14\lambda_0$ ($0.35\lambda_g$). 17

2.3 Calculated far-field directivity and gaussicity on a 12.7 mm diameter silicon lens at 94 GHz. 17

2.4 Sum-mode (a) and difference-mode (b) configurations of a double-slot antenna fed in series (a) or in parallel (b). 18

2.5 The impedance environment of the Schottky diode and the measured values on a 2 GHz model over a ±5% frequency range. 19

2.6 The fabricated 90 GHz receiver. For dimensions, see layout in Figure 2.1. 21

2.7 Measured and calculated E- and H-plane patterns at 88 GHz (a) and 94 GHz (b). 23

2.8 Video responsivity measurement set-up. 24

2.9 Measured and calculated video responsivity at 90 GHz. 24

2.10 The 90 GHz millimeter-wave quasi-optical setup (a) and measurement set-up (b). 26

2.11 Measured DSB conversion loss and noise temperature of the double-slot receiver. 27

3.1 A radar for automotive applications: a 3-dB beamwidth of 1.5° is required to resolve a car at 100 m. 32

3.2 Electric field orientations in a regular slot (a) and a resonant folded slot (b). The folded slots are 180° long, and the electric fields undergo a phase reversal at the antenna feed points. 34

3.3 Photograph of the fabricated 94 GHz double folded-slot antenna used for input impedance measurements. 34

3.4 Calculated feed patterns of the double folded-slot antenna into the silicon substrate at 94 GHz and 96 GHz. 35

3.5 Double folded-slot antenna input impedance measured (-) and calculated (- -) from 70-110 GHz. 35

3.6 Double folded-slot phase conditions at second resonance (94 GHz) and first resonance (79 GHz). The DFS is used at the second resonance for symmetrical patterns. 36

3.7 Comparison between measured and calculated E- and H-plane patterns at 94 GHz. 38

3.8 The 150 GHz double folded-slot antenna dimensions (a), S11 (b) and input impedance (c) simulated using Momentum from 140 GHz to 170 GHz (c). The input impedance is 20+j1 Ω at 154 GHz. 40

3.9 Picture of the University of Virginia SCT1T7-D20 Schottky diodes. 41

3.10 The layout of the subharmonic mixer (a) and impedance environment (b). 43

3.11 Method-of-Moment simulations of the input LO (a) and RF (b) impedances presented by the circuit at the diode junctions. R_d^* is the conjugate of the diode impedance. 44

3.12 Calculated SSB conversion loss for a 148-180 GHz RF and a 0.2-2.0 GHz IF with and without matching networks. 44

3.13 Picture of the fabricated subharmonic receiver. Dimension are given in the text in Section 3.2. 46

3.14 View of the complete subharmonic receiver. 47

3.15 W-band measurement set-up for conversion loss measurements. . . . 47

3.16 Measured E- and H-plane patterns at 150 GHz (a) and 154 GHz (b). The measured cross-polarization levels in the E- and H-planes were below -25 dB. 49

3.17 Measured DSB conversion loss and noise temperature of the subharmonic receiver versus frequency at 142-170 GHz for an IF frequency of 0.2 GHz and 1.4 GHz (a), and DSB conversion loss versus LO power available at the probe tip at 146 GHz, 150 GHz and 158 GHz (b). 50

3.18 Measured LO and IF mismatch losses. 51

4.1 Procedure to realize low-ϵ_r regions: the high-ϵ_r substrate (a) is drilled in a local area on a rectangular or triangle lattice (b). The patch is made out of copper tape (c). 55

4.2 Microwave test fixture used at 12-13 GHz. 57

4.3 The RF chain at 12.5-13.5 GHz. 60

4.4 Fabricated microstrip antenna (0.70×0.92 cm) on a Duroid substrate, $\epsilon_r = 10.8$, h=0.635 mm. The antenna is on localized low-ϵ_r dielectric ($\epsilon_r = 2.3$). 61

4.5 Comparision of the three antennas studied: $\epsilon_r = 10.8$ antenna (a), $\epsilon_r = 2.3$ synthesized antenna (b) and $\epsilon_r = 2.2$ antenna (c). The dimensions are in centimeters on the same scale. 62

4.6 Measured input impedances of microstrip antennas on $\epsilon_r = 2.2$, synthesized $\epsilon_r = 2.3$ and $\epsilon_r = 10.8$. 63

4.7 Measured radiation efficiencies of microstrip antennas on $\epsilon_r = 2.2$ (o), synthesized $\epsilon_r = 2.3$ (+), $\epsilon_r = 10.8$ (∗), and horn antenna (•). Calculated values are ♠ for $\epsilon_r = 2.2$ and ♢ for $\epsilon_r = 10.8$. 65

4.8 Predicted radiation efficiency of microstrip antennas on $\epsilon_r = 2.2$ (a) and $\epsilon_r = 10.8$ (b) substrates versus substrate thickness. 68

4.9 Radiation patterns of microstrip antennas on $\epsilon_r = 2.2$ at 12.9 GHz, synthesized $\epsilon_r = 2.3$ at 12.8 GHz, and $\epsilon_r = 10.8$ at 12.8 GHz. E-plane, H-plane (-) and cross-polarization patterns (- -) are shown. . 71

5.1 Perspective view (a) and cross-section (b) of the aperture-coupled micromachined microstrip antenna. All dimensions are in microns. . 75

5.2 Top view of the microstrip antenna design and of the cpw-to-microstrip transition. 76

5.3 Effective dielectric constant as a function of the silicon removed under a square patch on silicon, for various L/H ratios, where L is the patch width and H the substrate thickness. 77

5.4 Comparison between measured and simulated (IE3D) S-parameters of the cpw-to-microstrip transition. 78

5.5 Pictures of the microstrip antenna (a), micromachined cavity (b), coupling-slot (c) and feed line (d). The four pictures are not at the same scale. 80

5.6 Measured and simulated (IE3D) input impedance of the microstrip antenna built on a full silicon substrate of 100 μm thick (a) and on a 200 μm thick silicon wafer in which a 150 μm deep cavity has been etched (b). 81

5.7 Radiometric measurement set-up at 85-100 GHz. 83

5.8 Measured radiation efficiency of a microstrip patch antenna built on a full 100 μm silicon wafer (a), and of a micromachined microstrip antenna (b). 85

5.9 Integration of the bismuth bolometer to measure radiation patterns (a) and picture of the bismuth bolometer (b). 86

5.10 Measured radiation patterns of the micromachined microstrip antenna at 94 GHz. 87

5.11 Front (−) versus back (− −) radiation measured in the E-plane from 90 to 102 GHz. 87

5.12 Definition of the E- and H-planes of the aperture-coupled microstrip antenna. 88

5.13 Layout of the 2 × 2 antenna array to measure the mutual coupling with one single cavity (a) and individuals cavities (b). All dimensions are in microns. 89

5.14 Quasi-static simulations of the electric fields around the patch antenna on a micromachined silicon substrate. The fields are confined inside the cavity in the E-plane direction (a), and silicon beams are used to isolate two adjacent elements (b). 90

5.15 Picture of the four individual cavities with crossed silicon beams. . . 91

5.16 Measured mutual coupling comparison for the single cavity design (a) and individual cavities design (b). S12, S13, S14 correspond to the E-, H-, and 45°-plane directions, respectively. 92

5.17 Measured mutual coupling comparison in the E- (a) and H-plane (b) directions. 93

6.1 View of the w-band transitions: straight-stub cpw-to-microstrip (a), radial-stub cpw-to-microstrip (b), vertical cpw overlay (c) and vertical microstrip overlay (d). 96

6.2 CPW-to-microstrip transition and the equivalent three-line microstrip coupler used to analyze and design the transition. 97

6.3 Field configuration of the microstrip mode (A), even cpw mode (B) and odd cpw mode (C) in a three-line coupler. 98

6.4 Voltage and current definitions in the three-line coupler. 98

6.5 CPW-to-microstrip transition with straight coupling stubs (a) and with radial coupling stubs (b). 101

6.6 Pictures of the two fabricated back-to-back fgc-to-microstrip transitions showing the straight-stub design (a) and the radial-stub design (b). 103

6.7 CPW-to-microstrip straight-stub (a) and radial-stub (b) transitions S-parameters (-) vs. Method-of-Moment simulation (- -). 104

6.8 Perspective view of the cpw-to-cpw single-layer transition (a), and electric field configuration for the even and the odd cpw-mode (b). . 106

6.9 Layout of the two back-to-back cpw-to-cpw transitions (a) and close view of one single transition (b). All dimensions are in microns. . . 108

6.10 Picture of the fabricated back-to-back cpw-to-cpw transition, top (a) and bottom (b). Dimensions are found on Figure 6.9. 109

6.11 Measured and simulated (IE3D) W-band S-parameters of two back-to-back cpw-to-cpw transitions shown in Figure 6.9. 110

6.12 Layout of two back-to-back cpw-to-microstrip transitions including: a microstrip line of 2900 μm long (Reference Circuit) (a), and two back-to-back vertical microstrip-to-microstrip transitions (VMMT) (b). 112

6.13 Picture of the fabricated back-to-back microstrip-to-microstrip transition, top (a) and bottom (b). Dimensions are found on Figure 6.12. 113

6.14 Measured and simulated (IE3D) S-parameters of two back-to-back cpw-to-microstrip transitions including a long microstrip line section (Reference Circuit). Also included is the measured of two back-to-back vertical microstrip-to-microstrip transitions as shown in Figure 6.12(b). 114

6.15 Measured S-parameters of two back-to-back vertical microstrip-to-microstrip transitions versus the coupling region length, L. 115

7.1 Radar configuration. 119

7.2 Integrated millimeter-wave imaging receiver based on double folded-slot antennas for automotive applications. 121

7.3 Two-by-two 10-40 GHz micromachined phased array. 122

7.4 Conceptual diagram and picture of the 16 element phased array. . . 123

7.5 Perspective view (a) and cross-section (c) of the 94 GHz power cube. 125

A.1 Perspective view of the single- (a) and dual-polarized (b) microstrip antenna on membranes. 129

A.2 Cross-section and detail of the thin-film membrane. 130

A.3 Lay-out of the single- (a) and dual-polarized (b) microstrip antenna used for input impedance measurements. 131

A.4 Picture of the 77 GHz dual-polarized microstrip antenna. 133

A.5 Measured and calculated input impedance of the single- (a) and isolation of the dual-polarized (b,c) microstrip antenna at 70-90 GHz. . 134

A.6 Lay-out of the dual-polarized microstrip antenna used for radiation patterns measurements. 135

A.7 Video responsivity of the Schottky diodes at 77 GHz (a) and measured peak power versus frequency (b). 136

A.8 Measured polarization sensitivity for both HH- and VV-ports at 76-78 GHz. 138

A.9 Measured E-plane and H-plane patterns for both HH- and VV-ports at 78 GHz. 139

A.10 Uniplanar cpw-fed microstrip antenna on membrane. 140

A.11 Calculated radiation efficiency of a patch antenna and of an ideal dipole on a thin-film membrane ($\epsilon_r = 1.05$ substrate) versus substrate thickness at 77 GHz. 140

LIST OF TABLES

Table

2.1 A detailed breakdown of the loss mechanism and comparison with measured results at 90 GHz. 28

3.1 A detailed breakdown of the loss mechanism and comparison with measured results at 140-170 GHz. 51

4.1 Comparison between the two methods to measure dielectric constants for different machined hole densities. The last column indicates measurements with no drilled holes. 57

4.2 Measured and calculated radiation efficiencies at resonance for different substrates. 65

CHAPTER I

INTRODUCTION

Over the past decade, advances in integrated circuits (IC) technologies, VLSI technological development, semiconductor processes, digital processing and radio frequency (RF) circuits have contributed to the widespread commercialization of wireless communications: development of cellular, cordless and PCS communication services (GSM, DEST) as well as commercial radio applications, networking (LAN, WLAN) and satellite communications. Standard frequency bands for mobile local and satellite communications extend from 900 MHz to 2.4 GHz. The fast growth of the wireless communication industry and market, and the increased demand for affordable, portable mobile communication systems with a higher number of functions, have motivated innovations in the design and integration of RF circuits at even higher frequencies (10 to 100 GHz). Nowadays, emerging applications in commercial, military and scientific communication systems are introducing new challenges to the technological development of millimeter-wave components and circuits. The existing infrastructure (silicon and GaAs foundries), maturing modeling tools and design methods contribute to this trend.

The millimeter-wave (30 GHz-300 GHz) and submillimeter-wave (300 GHz-3 THz) bands offer well-known advantages over microwave frequencies: smaller wavelengths

allowing higher-gain antennas, smaller apertures and larger bandwidths. Historically millimeter-wave circuits were developed for military radar, imaging and tracking systems, and were also applied to scientific areas such as radio-astronomy and more recently, remote sensing of the atmosphere, oceans and earth, taking advantage of the transmission windows in the atmosphere at millimeter-wave frequencies. Traditionnally, millimeter-wave circuits and systems, mainly heterodyne SIS receivers, relied on waveguide technology, prohibiting their use in large quantities due to their weight and fabrication cost. Besides, millimeter-wave sources were heavy and expensive. Also, planar circuits did not provide an alternative to waveguide-based systems since at millimeter-wave frequencies, substrates were costly and lossy, preventing the design of high performance circuits. This thesis investigates millimeter-wave low-loss, compact and lightweight planar geometries which provide simple solutions to design high-performance millimeter-wave integrated front-end receivers and high-efficiency planar antennas.

1.1 Millimeter-Wave Planar Technologies

The recent efforts towards planar millimeter-wave technologies promise low-cost, light, small, compact, displaying high-performance, monolithic integrated systems for a wide variety of applications. Coplanar waveguides (cpw) and microstrip lines are most commonly used to propagate electromagnetic waves in planar circuits. In coplanar waveguides, the lines are etched out of the ground plane on the same side of the substrate, and the electromagnetic fields are therefore confined partly in the air, partly in the dielectric (Fig. 1.1(a)). The fundamental mode propagating in cpw lines is quasi-TEM. However, the ground-to-ground spacing has a higher limit above which quasi-TEM propagation does not take place and is disturbed by line

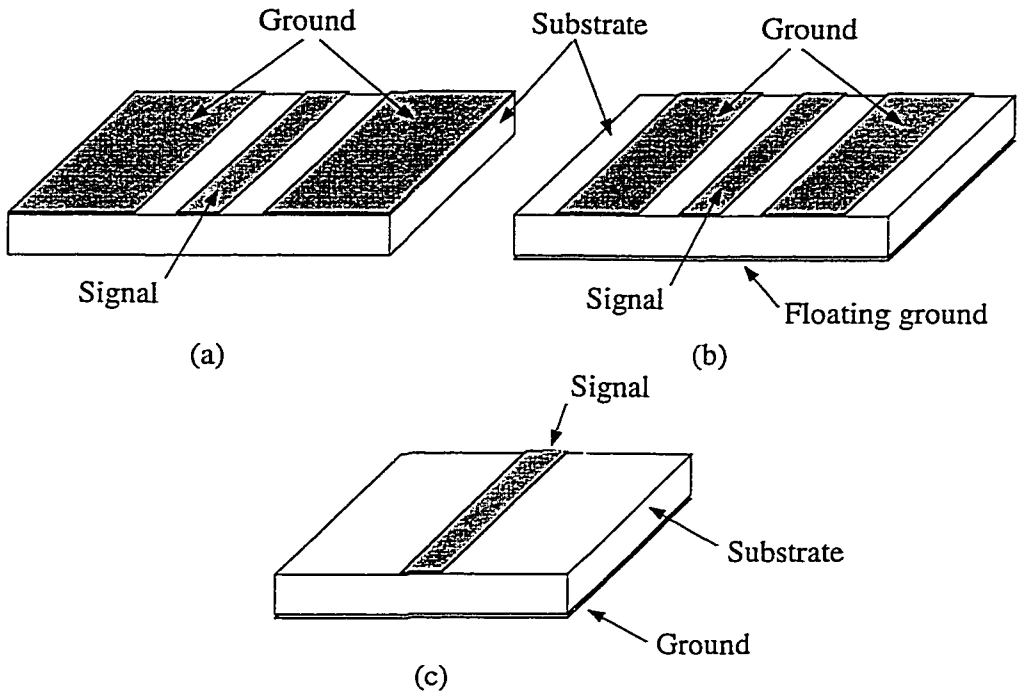

Figure 1.1: Comparison between coplanar waveguide cpw (a), finite ground coplanar waveguide (b) and microstrip (c) propagation modes.

radiation, resulting in increased losses. This maximum ground-to-ground spacing is approximately $\lambda_g/10$ where λ_g is the guided wavelength [1]. When cpw lines are used on a substrate backed with a floating ground plane, the infinite extension of the cpw grounds on the top surface allows the propagation of unwanted parallel plate modes inside the substrate. An alternative to cpw lines is the finite ground coplanar waveguide (fgc), where the cpw grounds are of finite width (Fig. 1.1(b)). The fgc line looks like a three-strip waveguide: the central strip carries the RF signal, and the two outer metal strips are the fgc ground. The latter have to be equalized with air-bridges to prevent the propagation of odd-modes in the structure [2]. Also, the total width of the fgc line is empirically chosen to be small compared to the frequency of operation, typically $\lambda_g/4$ [3]. The presence of three microstrip strips on the top surface and of a floating ground plane on the bottom surface can

trigger different microstrip modes in the structure. Careful attention must therefore be given to the characteristic impedance of each mode, fgc or microstrip, especially at discontinuities such as transitions, bends or T-junctions. In microstrip lines, a ground plane is required on the other side of the substrate (Fig. 1.1(c)). For substrates with a dielectric constant above $\epsilon_r = 6$, the fields are mostly confined inside the dieletric. The maximum substrate height to be used with microstrip lines is close to $\lambda_d/10 - \lambda_d/8$ in order to avoid the propagation of surface waves inside the substrate, where λ_d is the wavelength inside the dielectric. At a given frequency, the guided wavelength of a transmission line with the same characteristic impedance is then smaller for microstrip lines. Microstrip lines are also more dependant on the substrate thickness than cpw lines.

Dielectric and conductor losses are mostly responsible for the attenuation in cpw and microstrip lines. In cpw lines, the current distribution is along the edges of the central conductor and of the grounds. This results that cpw lines have a larger attenuation per unit length due to high conductor losses. At 30 GHz, the attenuation is typically 0.45 dB/cm for a 50 Ω microstrip line on 300 μm-thick silicon, and 1.0 dB/cm for a 50 Ω cpw line on 500 μm-thick silicon [1]. However, cpw lines allow easy series and parallel connections and do not require via holes. Both technologies are compatible with standard IC fabrication techniques, (photolithography, electroplating, front-side/back-side alignments) including state-of-the-art micromachining processes especially developed for the fabrication of MEMS (Micro-Electromechanical Systems) components. Figure 1.2 shows the block diagram of a typical transceiver used in mobile communications systems. Nowadays, all basic components of the system can be designed and built from planar technologies: transistors, amplifiers, mixers, oscillators, doublers and multipliers, phase detectors and phase shifters, diplexers,

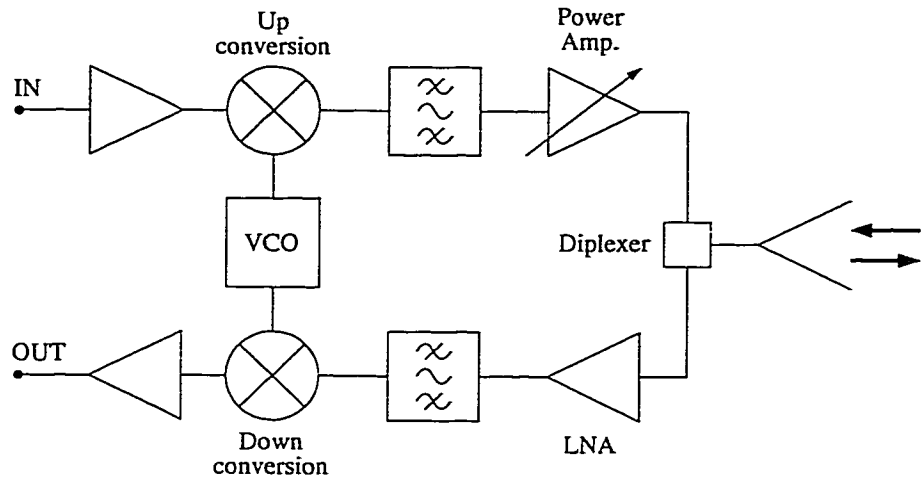

Figure 1.2: Block diagram of a typical millimeter-wave front-end transceiver for communication systems.

switches, power dividers/combiners, and planar antennas.

The radiation properties of planar antennas integrated on silicon or GaAs substrates have been extensively studied theorically and experimentally for the past 30 years, particularly the four basic antennas: dipole, double-dipole, slot and double-slot [4]. A single radiating element printed on top of a semi-infinite substrate radiates mostly inside the dielectric, to the ratio $\epsilon_r^{3/2}$. For silicon ($\epsilon_r = 11.7$), it means that 98% of the power is radiated inside the substrate. One consequence of this effect is the triggering of surface waves propagating inside the substrate: all the power radiated above the critical angle defined by $sin(\theta_c) = n_1/n_2$ is trapped by total internal reflection at the dielectric/air interface (Fig. 1.3).

At millimeter-wave frequencies, the high dielectric constant of the substrates used ($\epsilon_r = 11.7$ for silicon) implies that surface waves are more easily triggered in the substrate and become dominant, therefore limiting the radiation efficiency, radiation patterns and bandwidth. Also, the absolute gain drops very quickly as the substrate height increases [4]. Detailed analysis [5, 6, 7] showed that, for low-loss operation, the

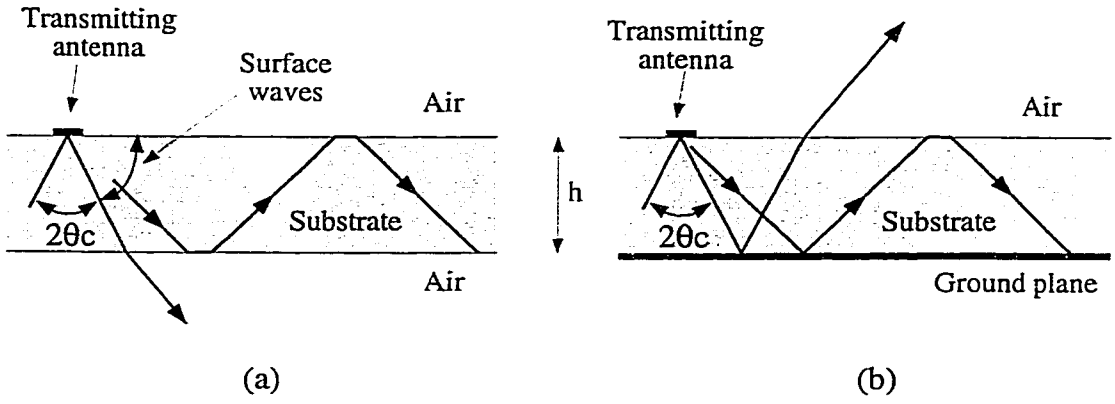

Figure 1.3: Surface waves are triggered by total internal reflection of the power radiated above the critical angle for ungrounded substrates (a) and grounded substrates (b).

silicon substrate thickness should be less than $0.04\lambda_0$ for slot antennas and $0.01\lambda_0$ for dipole antennas [8]. This results in unreasonably thin substrates at millimeter-wave frequencies. Furthermore, the patterns radiated on such substrates is bi-directional, and a reflecting ground plane (with a dipole antennas) and a backing cavity (with a slot antenna) should be used to make the patterns uni-directional.

1.2 Planar Integrated Receivers

Integrated-circuit uniplanar receivers consisting of a planar antenna and matching networks are often built on a standard substrate without any backing ground plane. In this case the cpw technology is the most appropriate. It allows for the use of millimeter-wave flip-chip devices (Schottky diodes and high-speed transistors) and components (MMIC mixers and amplifiers). Also, one can monolithically integrate the same devices [9, 10, 11]. Basically, the fabrication techniques of millimeter-wave cpw-based integrated receivers are now not a limitation to mass production, and the main effort has to be focused on reducing the antenna radiation and transmission-line propagation losses on high-ϵ_r substrates to achieve high-performance systems.

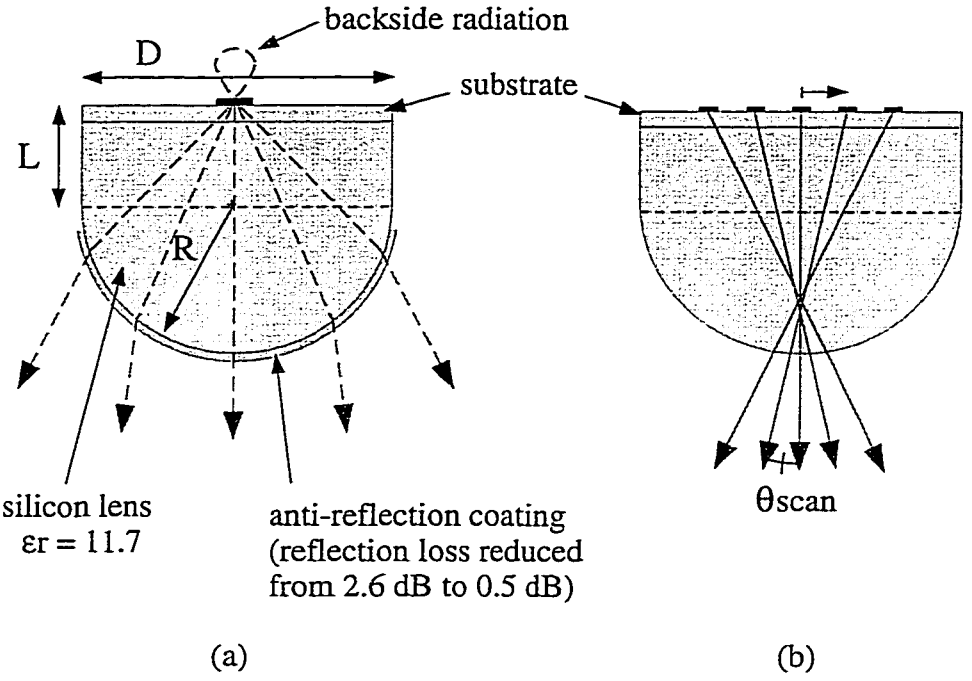

Figure 1.4: Sketch of an extended hemispherical dielectric lens (a) and off-axis properties (b). The mains beam is scanned when the antenna is moved off-axis.

Dielectric lenses have been introduced in optical systems to suppress the substrate air/dielectric interface, therefore synthesizing a semi-infinite dielectric half-space [12, 13, 14]. The best results are obtained if the lens has roughly the same dielectric constant as the substrate (Fig. 1.4). At first, hemispherical lenses were used but they are not suitable for microwave and millimeter-wave frequencies: they suffer from off-axis aberrations in imaging systems and the coupling to plane waves is poor. Recent extensive theoretical and experimental studies by Filipovic *et al.* [15, 16] have shown that extended hemispherical lenses, consisting of a dielectric hemisphere of radius R with a cylindrical extension L, have very interesting quasi-optical properties: increased directivity, good coupling to gaussian beams, and excellent off-axis properties [17]. A particular case of the extended hemispherical lens is the hyperhemispherical lens, where $L = R/n$. For hyperhemispherical lenses, the planar

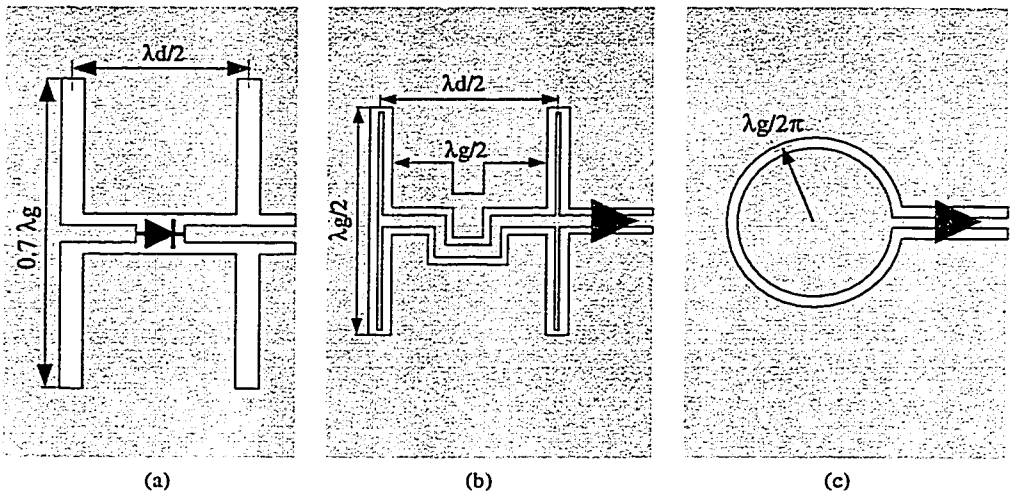

Figure 1.5: Uniplanar cpw-based antennas: double-slot (a), double folded-slot (b) and slot-ring (c).

antenna gain is increased by n^2. Figure 1.4(a) sketches the geometry of extended hemispherical lenses with the resulting focusing effect. When moving the antenna off-axis, the beam will be scanned off-axis. This geometrical effect results from phase front conditions (Fig. 1.4(b)). Detailed theoretical and experimental analysis can be found in Filipovic's thesis [18]. The high dielectric constant of silicon ($\epsilon_r = 11.7$) creates a large mismatch between the lens and the free-space environment ($\epsilon_r = 1$). In transmission line theory, the interface silicon/air can be seen as an impedance step: the characteristic impedance of the plane wave in air is Z_0=377 Ω, while the characteristic impedance is $Z_{Si}=Z_0/\sqrt{\epsilon_r}$ or Z_{Si}=110 Ω in silicon. The reflection loss at the interface is then Γ=-2.6 dB. This loss can be suppressed by coating the lens with a $\lambda_m/4$ matching cap layer of dielectric constant $\epsilon_m = \sqrt{\epsilon_{Si}}$, or $\epsilon_m = 3.4$, acting like a quarterwave transformer (Fig. 1.4(a)). At 94 GHz and 150 GHz, a 430 μm- and 260 μm-thick Stycast layer ($\epsilon_r = 4$) is recommended [19].

Three planar cpw-fed antennas have been commonly used in millimeter-wave receivers (Fig. 1.5): the double-slot, the double folded-slot and the slot-ring antennas.

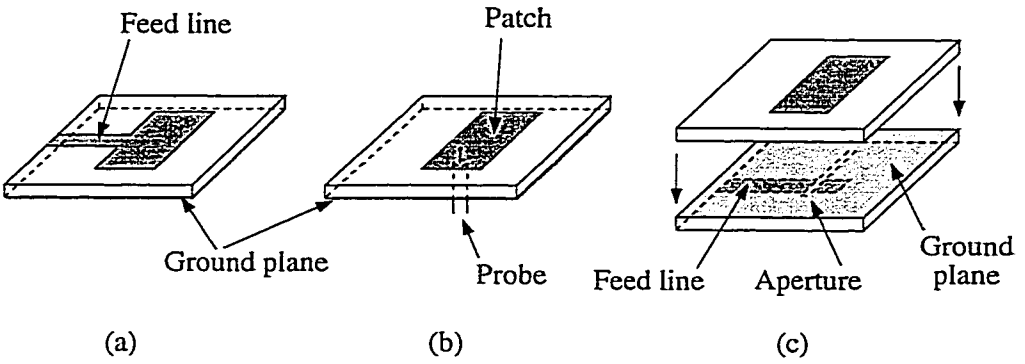

Figure 1.6: Various microstrip antenna geometries: microstrip line fed (a), probe fed (b) and aperture-coupled (c).

The slot-ring antenna is very attractive for dual-polarized and array applications for its small size and symmetry. However it has a high input impedance, typically around 100-120 Ω, and therefore an input matching network is required for most applications. The slot-ring antenna has been successfully demonstrated in an integrated millimeter-wave monopulse receiver [20, 21]. The double-slot and double folded-slot antennas will be described in details in Chapters 2 and 3, respectively.

1.3 Millimeter-Wave Microstrip Antennas

The microstrip antenna is a very attractive solution for all applications requiring compact, low-cost and high-performance planar apertures, particularly imaging arrays and collision avoidance radars. Like microstrip lines, it consists simply of a metal patch on top of a dielectric substrate, with a ground plane on the other side of the substrate. Microstrip antennas provide a wide variety of designs, and can be applied to many types of planar and conformal surfaces. For example conformal microstrip antennas on cylinders or cones are of great interest for phased arrays used on wings in flight applications. Microstrip antennas can also be fed in many different ways (Fig. 1.6). Microstrip-line fed and probe-fed microstrip antennas are

commonly employed for simplicity reasons. Aperture-coupled microstrip antennas are more complex to design but offer more advantages in array systems, because the ground plane isolates the patch antenna from the feeding network.

At millimeter-wave frequencies, however, many limitations have to be overcome in order to design high-efficiency microstrip antennas on silicon or GaAs substrates. The reason is that microstrip antennas on high dielectric constant substrates ($\epsilon_r > 6$) suffer from very narrow bandwidths (less than 2%), low efficiency and poor radiation patterns due to the triggering of surface waves in the dielectric. Figure 1.7 shows the cut-off frequencies of surface modes versus the thickness of grounded substrates for $\epsilon_r = 4$ and $\epsilon_r = 12$. It can be seen that high-order surface waves can be avoided by using substrates with a thickness of less than $0.15\lambda_0$ ($0.30\lambda_d$) for $\epsilon_r = 4$, and $0.9\lambda_0$ ($0.26\lambda_d$) for $\epsilon_r = 12$, where λ_d is the dielectric wavelength in the dielectric ($\lambda_d = \lambda_0/\sqrt{\epsilon_r}$). Also, the dominant TM_0 mode has a zero cut-off frequency in all cases. However, the power lost to TM_0 surface wave can be reduced by using thin substrates, typically $\lambda_d/10$. At 94 GHz for silicon ($\epsilon_r = 11.7$), this corresponds to around 100 μm thick substrates. However, while it is possible to design good RF circuits on thin high dielectric constant substrates, the radiation efficiency of microstrip antennas will be greatly reduced.

The radiation efficiency of microstrip antennas is the ratio of the radiated power to the total input power, $\eta = P_r/P_T$ with $P_T = P_r + P_d + P_c + P_s$, P_d and P_c are the dielectric and conductor losses, respectively, and P_s is the power lost to surface waves. In order to understand how the radiation efficiency depends on the substrate thickness h, it is interesting to view the microstrip antenna as two slots, or magnetic current sources $\lambda_g/2$ apart at the frequency of resonance. This model is simple but describes accurately the behaviour of microstrip antennas. The radiation resistance

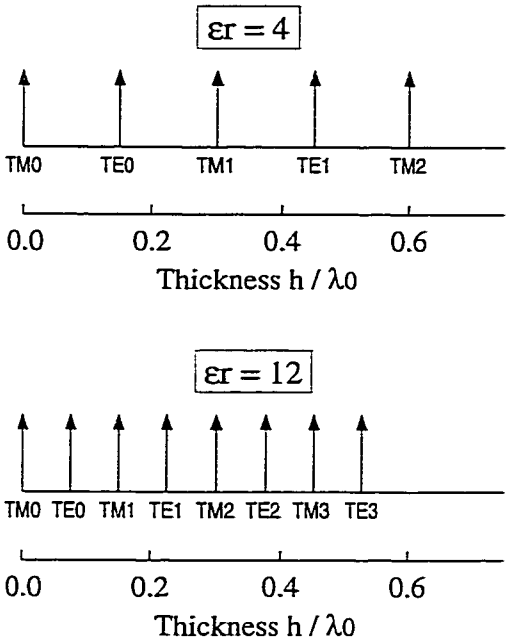

Figure 1.7: Surface wave cut-off frequencies for low- ($\epsilon_r = 4$) and high- ($\epsilon_r = 12$) dielectric constant grounded dielectric slab. In both cases, the dominant TM_0 mode has a zero cut-off frequency.

of resonant slots has been calculated and is, for small substrate heights h,

$$R_r = 120\lambda_0/(1 - k_0h^2/24) \tag{1.1}$$

and the power radiated

$$P_r = V_0^2/2R_r \tag{1.2}$$

where k_0 is the wave number and V_0 the input voltage [22]. The slot radiation resistance R_r is an inverse function of h, and the power radiated P_r increases with h. Therefore, microstrip antenna radiation efficiency increases with substrate height h. However, for thick substrates, surface mode losses become dominant and limit the radiation efficiency. To maximize the antenna radiation efficiency, a trade-off has to be found between different effects: surface waves which require thin substrates, radiation efficiency which requires thick substrates, dielectric and conductor losses. For microstrip antennas on silicon, the optimum substrate thickness is a broad function

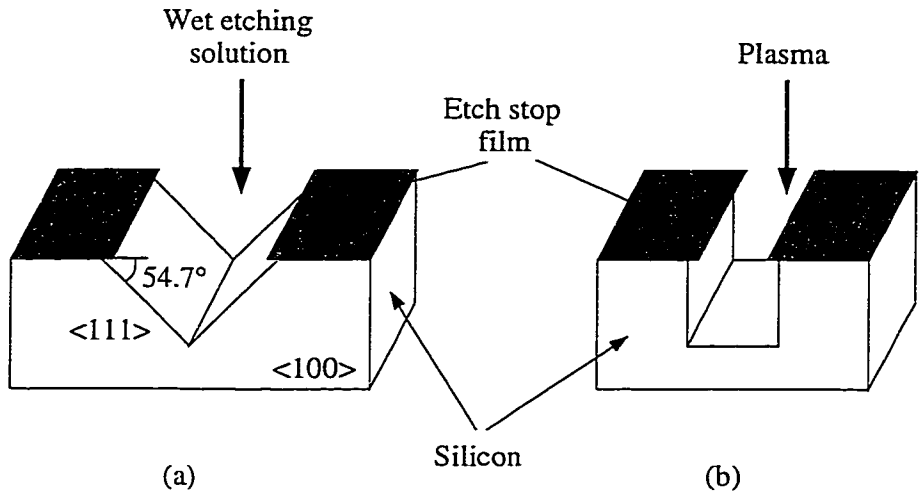

Figure 1.8: Micromachining fabrication processes based on anisotropic wet etching (a) and reactive ion etching (b).

of h, and is $h = \lambda_d/12 - \lambda_d/8$.

A recent solution is the use of micromachining fabrication techniques to locally synthesize a low dielectric constant region around the antenna by artificially removing the dielectric substrate. The micromachining fabrication processes have been developped for MEMS and are now well established techniques in microfabrication. The easiest technique to remove silicon is by using chemical wet etching, either with TMAH or KOH. The etching is anisotropic along the $< 111 >$ crystal planes (Fig. 1.8(a)). TMAH has more undercut than KOH but results in smoother surfaces in cavities. Also, vertical walls can be obtained with Reactive Ion Etching (RIE) (Fig. 1.8(b))

1.4 Overview of Thesis

This thesis comprises seven chapters, and one appendix. In Chapter 2, a 90 GHz Schottky-diode uniplanar receiver based on a cpw-fed double-slot antenna is presented. The receiver is placed on an extended hemispherical high-resistivity silicon

substrate lens, and the design is very small, less than 1.1 x 4 mm including the RF/IF filter. The LO is injected quasi-optically. In Chapter 3, a 140-170 GHz Schottky-diode subharmonic receiver based on the same approach is described. A double folded-slot antenna is used together with a back-to-back- diode subharmonic mixer, allowing on-wafer LO injection by W-band probes.

Micromachining techniques using closely spaced holes have been used underneath a microstrip antenna on a high dielectric constant substrate ($\epsilon_r = 10.8$) to synthesize a localized low dielectric constant environment ($\epsilon_r = 2.3$). The approach is demonstrated at 13 GHz and is detailed in Chapter 4. In Chapter 5, an aperture-coupled micromachined microstrip antenna operating at 94 GHz is described. The design consists of two stacked silicon substrates: 1) the top substrate, which carries the microstrip antenna, is micromachined to improve the radiation performance of the antenna, and 2) the bottom substrate, which carries the microstrip feed line and the coupling slot.

Interconnections and low-loss transitions based on electromagnetic coupling are investigated in Chapter 6. It is shown that cpw and microstrip circuits can be combined through the use of these low-loss transitions to achieve highly integrated millimeter-wave front-end receivers. Finally, Appendix 1 summarizes the design, fabrication and measurement of single and dual-polarized microstrip antennas on thin- film membranes.

CHAPTER II

A PLANAR 90 GHz SCHOTTKY-DIODE MILLIMETER-WAVE RECEIVER

Integrated-circuit receivers consisting of a planar antenna integrated with a matching network and a planar Schottky-diode or a three-terminal device offer an attractive advantage over the waveguide-based receivers at millimeter-wave frequencies. They are smaller, lighter and less expensive to build than waveguide systems, and can be easily produced in large numbers for low-cost applications and millimeter-wave imaging systems. A candidate for a potential of excellent millimeter-wave performance is the double-slot antenna. This antenna was proposed by Kerr et al. [23] and later used in conjunction with a hyperhemispherical quartz substrate lens in an SIS receiver at 492 GHz [24]. The double-slot antenna approach has also been used with thick dielectric substrates to cancel the power loss to the dominant TM_0 mode [25, 26].

In this chapter, the design was improved by: 1) using a coplanar-waveguide (cpw) transmission-line between the slot antennas instead of a microstrip line and 2) placing the slot antenna on an extended hemispherical high-resistivity silicon substrate lens to result in high gain patterns and high Gaussian-coupling efficiency [15, 16]. The cpw ground-planes are equalized using air-bridge technology and the design requires

no via holes or a backing ground-plane. The uniplanar design is compatible with monolithic integration of state-of-the-art Schottky-diodes and high-speed transistors.

2.1 Antenna Design

The cpw-fed double-slot antenna receiver is shown in Figure 2.1. In this design, the length of the slot antenna controls the H-plane pattern and the separation between the slot antennas controls the E-plane pattern. The patterns are calculated assuming a sinusoidal magnetic current distribution on the slot-antenna and using an array-factor in the E-plane direction. The wavelength of the sinusoidal current distribution in the slot is the guided wavelength given by $\lambda_g = \lambda_0/\sqrt{\epsilon_g}$ with $\epsilon_g = (1+\epsilon_r)/2$ and $\epsilon_r = 11.7$ for high resistivity silicon [16, 27]. The slot antennas are chosen to be $0.28\lambda_0$-long ($0.70\lambda_g$) with a separation of $0.14\lambda_0$ ($0.35\lambda_g$), where λ_0 is the free-space wavelength at 90 GHz (λ_0=3.33 mm), and λ_g the guided wavelength. This results in a symmetrical pattern with a 10-dB beamwidth around 48° (Fig. 2.2) and an associated directivity of 11.1 dB inside the silicon dielectric lens. The calculated cross-polarization level is lower than -30 dB in the 45°-plane. The dielectric lens approach eliminates the power loss to substrate modes and makes the pattern unidirectional into the dielectric lens [7]. The power radiated to the back-side is minimal, only 9% (0.4 dB), and the level of the peak backside patterns is -16 dB. Therefore no back-cavity is used to recover this power loss.

The far-field pattern of the double-slot antenna/extended hemispherical lens system is calculated using a ray-tracing technique inside the silicon lens and aperture field integration on the silicon-lens contour. For a complete description of this method, the reader is referred to the work of Filipovic *et al.* [15]. The double-slot antenna is placed on a 12.7 mm diameter silicon lens with an extension length of

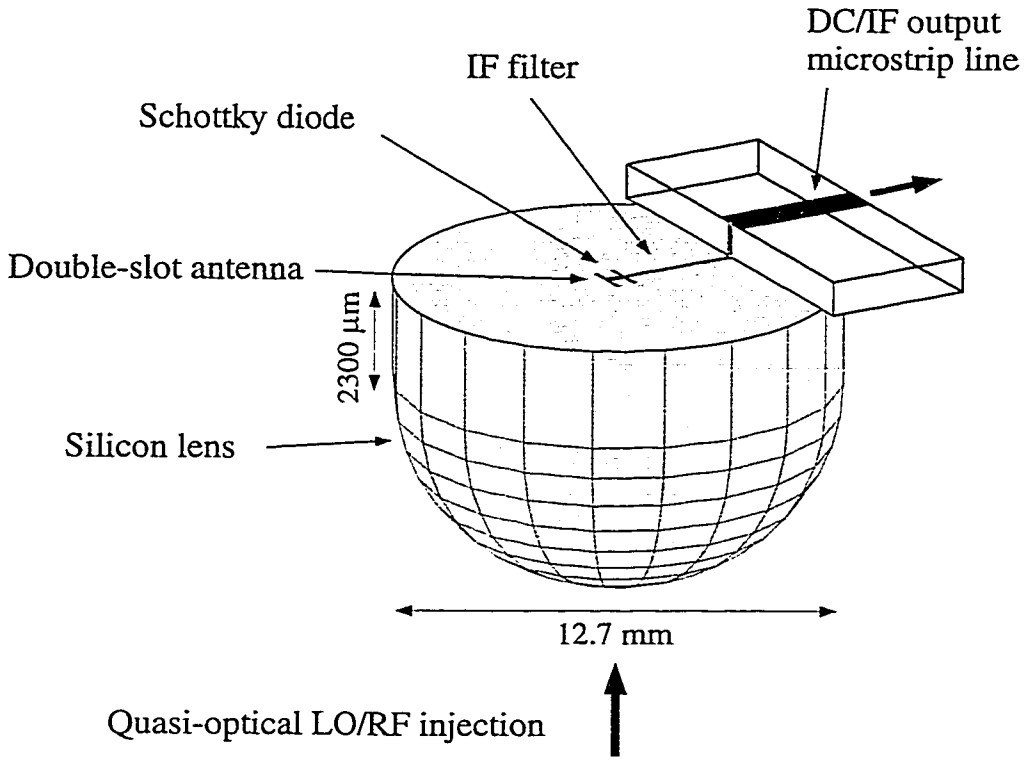

(a)

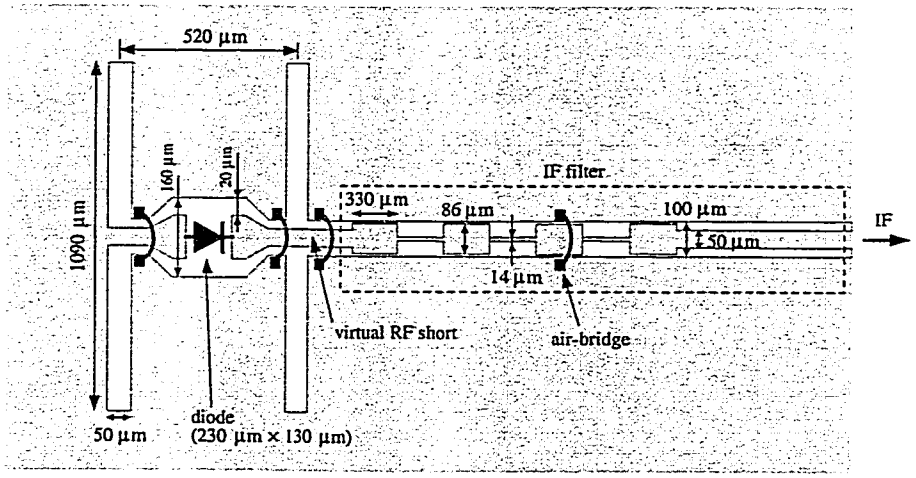

(b)

Figure 2.1: View of the 90 GHz receiver (a) and layout of the cpw-fed double-slot antenna (b).

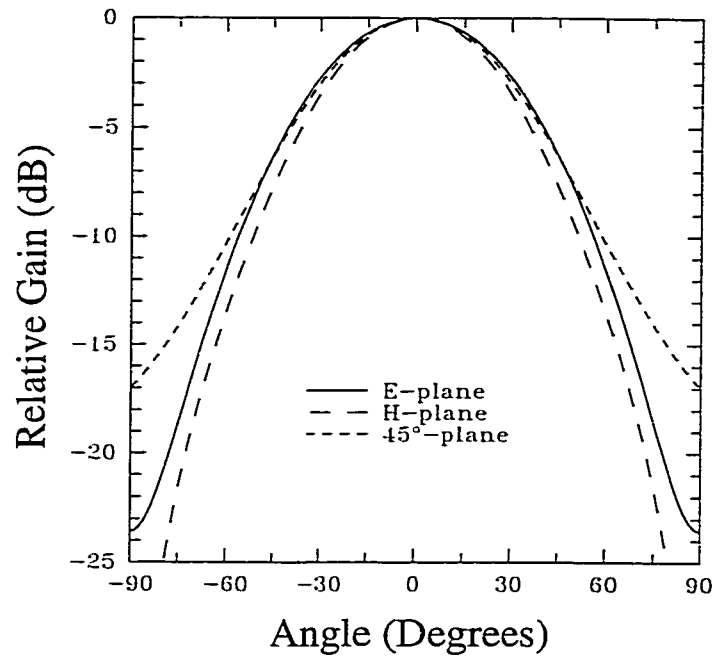

Figure 2.2: Calculated double-slot radiation patterns inside the silicon lens for a slot length of $0.28\lambda_0$ ($0.70\lambda_g$) and a slot separation of $0.14\lambda_0$ ($0.35\lambda_g$).

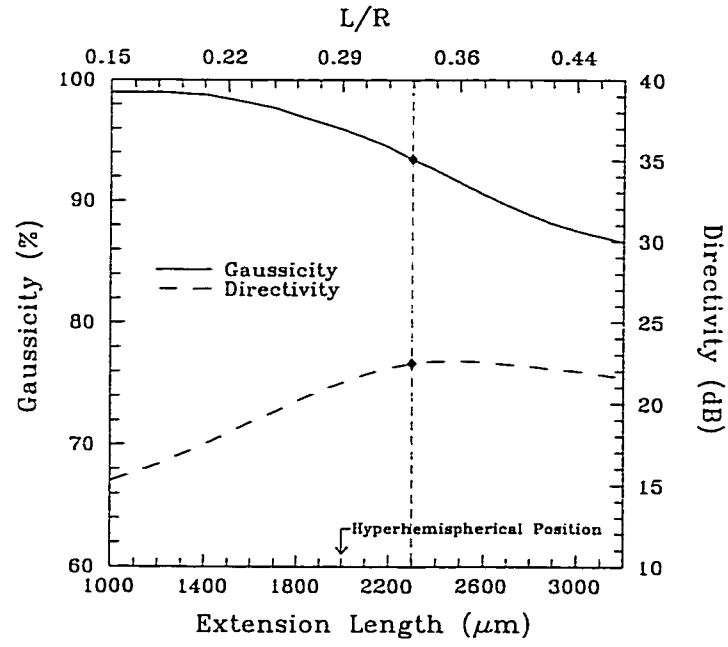

Figure 2.3: Calculated far-field directivity and gaussicity on a 12.7 mm diameter silicon lens at 94 GHz.

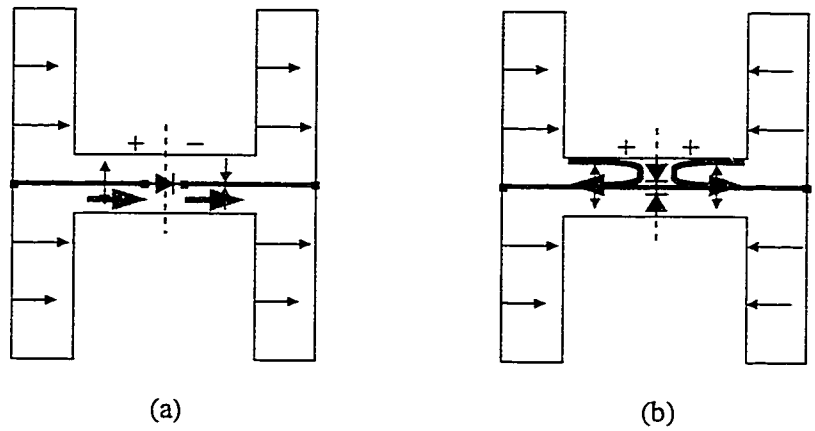

Figure 2.4: Sum-mode (a) and difference-mode (b) configurations of a double-slot antenna fed in series (a) or in parallel (b).

2300 μm ($L/R = 0.33$) behind the hemispherical center of the lens. This results in a directivity of 22 dB and a 94% coupling efficiency of the antenna to a Gaussian beam, or gaussicity (Fig. 2.3). It is clear that the extended hemispherical lens results in high gain patterns with a slight reduction in gaussicity compared to the hyper-hemispherical position. The gaussicity does not include power loss to the back-side (0.4 dB) and the reflection loss at the silicon-air interface. The reflection loss is calculated to be 1.8 dB for no matching-cap layer on the silicon lens and 0.4 dB for a $\lambda_m/4$ matching-cap layer with uniform thickness [15, 19], where λ_m is the mean wavelength between silicon and air and is given by $\lambda_m = \sqrt{\lambda_0 \lambda_{Si}}$. It is important to note that a high directivity and a Gaussian coupling efficiency of 88% is also achieved if the double-slot antenna is placed on an elliptical silicon lens [15].

2.2 Receiver Design

The Schottky-diode is placed in series between the slot antennas to result in a sum-mode pattern (Fig. 2.5(a)). The series placement of the diode insures that the current feeds both slot antennas in phase. Therefore, the double-slot antenna

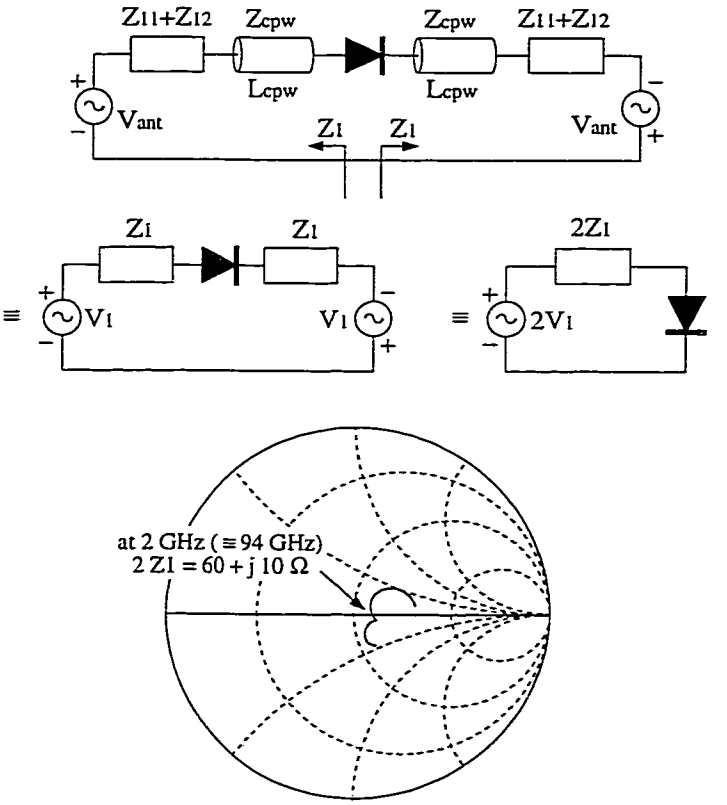

Figure 2.5: The impedance environment of the Schottky diode and the measured values on a 2 GHz model over a ±5% frequency range.

radiation patterns are the single slot patterns multiplied by the array factor. In the shunt placement, the diodes are placed across the cpw feed line (Fig. 2.5(b)). The current is flowing in the diodes when the two slot antennas are out-of-phase, resulting in difference-mode patterns with a null in the broadside direction.

The cpw line dimensions are s=50 μm and w=25 μm at the slot-antenna feed-points resulting in a line impedance of 50 Ω on a semi-infinite silicon substrate. The ground-to-ground cpw-line spacing is 100 μm, which allows low-loss quasi-TEM propagation at 100 GHz and limits the line radiation [1]. The ground-planes of the cpw line are equalized using air-bridges just near the feed-points of the slot-antennas. The cpw is widened in the middle so as to accommodate a planar (hybrid) Schottky-diode. The planar diode is an Alpha 32654 and is silver-epoxied to the cpw line. The cpw line is short-circuited to the ground-plane at the left slot antenna and this provides the DC return for biasing the diode. On the right slot-antenna, the cpw line is connected to a low-pass IF filter. The IF filter is designed to present a short-circuit at the slot antenna input at 90 GHz. The slot antenna self and mutual impedances on an infinite dielectric have been calculated [27, 28, 24], and the second resonance ($0.28\lambda_0$-long antenna) provides a wideband self impedance (Z_{11}), around 30 Ω, on silicon substrates. The impedance at the diode terminals is given by a series combination of the slot antenna input impedance as shown in Figure 2.5.

However, in this case, Z_1 is difficult to calculate due to the widening geometry of the cpw line and the relatively large GaAs substrate of the hybrid Schottky-diode (400×130×200 μm). A 2 GHz model was built and the *measured* input impedance at the diode terminals is 60+j10 Ω (Fig. 2.5). This was done by using an appropriate Balun, and by using a small piece of Stycast [29] over the cpw transmission line to model the parasitic effect of the hybrid GaAs diode. The 2 GHz model was placed on

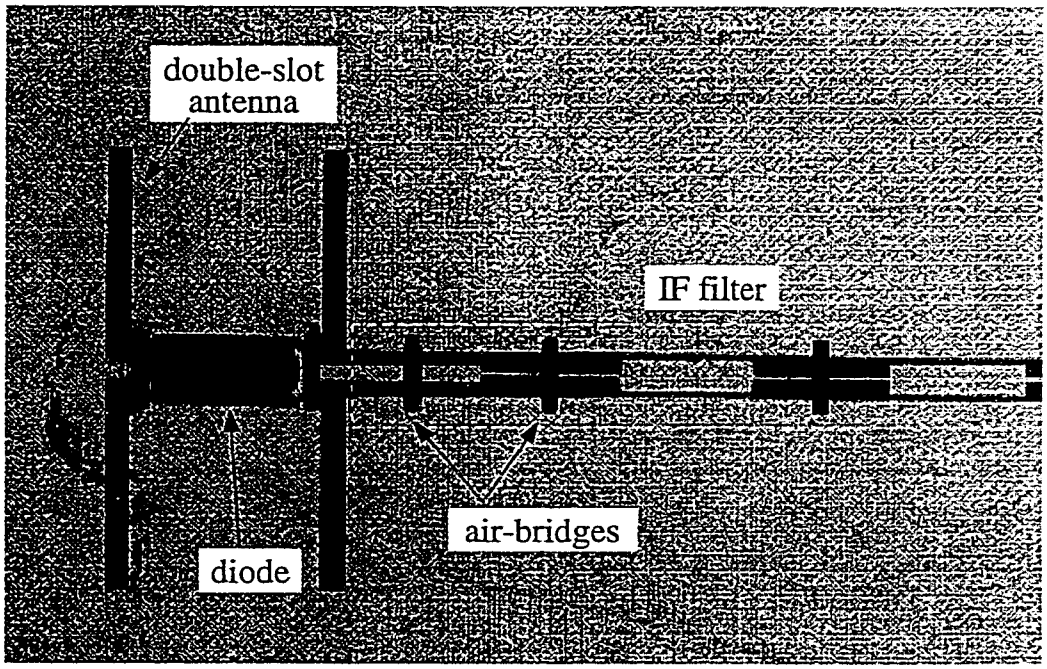

Figure 2.6: The fabricated 90 GHz receiver. For dimensions, see layout in Figure 2.1.

a large Stycast block ($\epsilon_r = 12$) surrounded by an RF absorber and time gating was used to eliminate the reflections from the Stycast-absorber interface. The measured input impedance at the second harmonic is 17+j14 Ω. Both measured impedances have a comfortable ±5% bandwidth.

The nominal diode capacitances are $C_{j0} = 18\ fF$ and $C_p = 14\ fF$ and the measured DC parameters are R_s=8 Ω, $n = 1.1$, $\Phi_b = 0.78$ V and $I_s = 1.6 \times 10^{-14}$ A. This yields a figure-of-merit cutoff frequency given by $f_T = 1/2\pi R_s(C_{j0}+C_p)$ of 620 GHz. The mixer theoretical SSB conversion loss [28] is simulated using a harmonic balance analysis [30] and calculated to be 7.0±0.1 dB at an LO frequency of 90 GHz, an IF frequency of 1.4 GHz, a DC bias of 0.5 V, a DC current of 3 mA and an available LO power at the diode terminals of 2-3 mW. The calculated diode RF impedance is 37-j30 Ω and therefore, the RF mismatch between the double-slot

antenna and the diode is around 1.5 dB. The calculated output IF impedance is 70-75 Ω. The IF network consists of a 7-section low-pass cpw filter with a corner frequency of 53 GHz and a short-circuit rejection of -24 dB at 90 GHz. The filter is of alternating low (27 Ω) and high (78 Ω) impedance sections and the corresponding cpw geometry is obtained from LineCalc [31]. The IF filter is 3.5 mm long with a measured DC series resistance of 6 Ω. The filter is followed by a $\lambda/4$ microstrip matching network at 1.4 GHz on a low-loss Duroid Substrate [32] with an impedance of 60 Ω.

2.3 Millimeter-Wave Measurements

The receiver was built using standard photolitographic techniques for 86-94 GHz operation on a high resistivity silicon substrate (2000 $\Omega - cm$). The antennas and cpw lines are evaporated gold $5000 - 6000$ $\AA$ thick (two skin depths at 90 GHz), and the air-bridges are fabricated using an electroplating technique (Fig. 2.6). The air-bridges are 1-1.2 μm thick, 15 μm wide, 100 μm long and with a height of 1.4 μm over the cpw transmission line. The planar diode is hybrid mounted on the cpw line using silver epoxy (Epo-Tek H20E). It is possible to build an identical receiver monolithically on a GaAs substrate with a planar millimeter-wave Schottky-diode [33].

The double-slot antenna was centered on a 12.7 mm diameter extended hemispherical high-resistivity (>2000 Ω.cm) silicon lens. Figure 2.7 shows the measured patterns at 88 GHz and 94 GHz for an extension length of 2300 μm. The E and H-plane patterns are symmetrical with low sidelobe levels, a high Gaussian coupling efficiency and agree very well with theory. The measured cross-polarization level is below -25 dB in the 45°-plane and below -30 dB in both E- and H-plane pat-

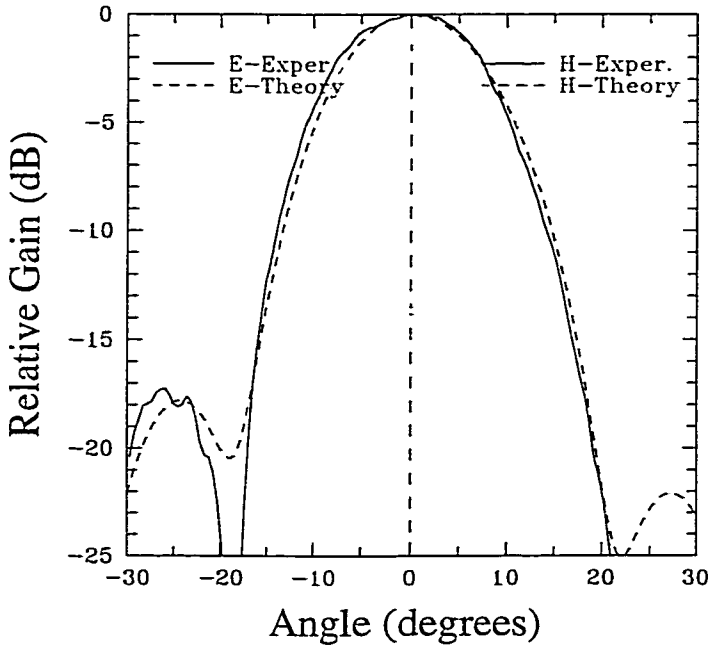

(a)

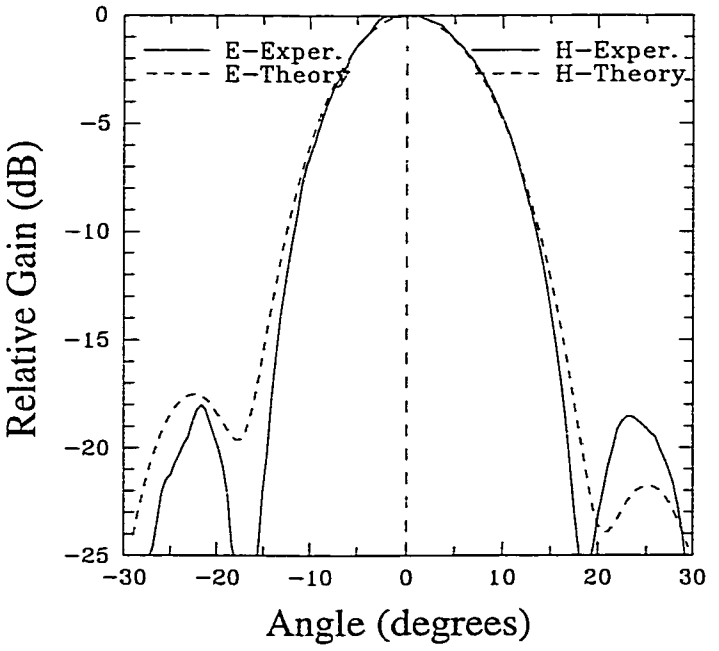

(b)

Figure 2.7: Measured and calculated E- and H-plane patterns at 88 GHz (a) and 94 GHz (b).

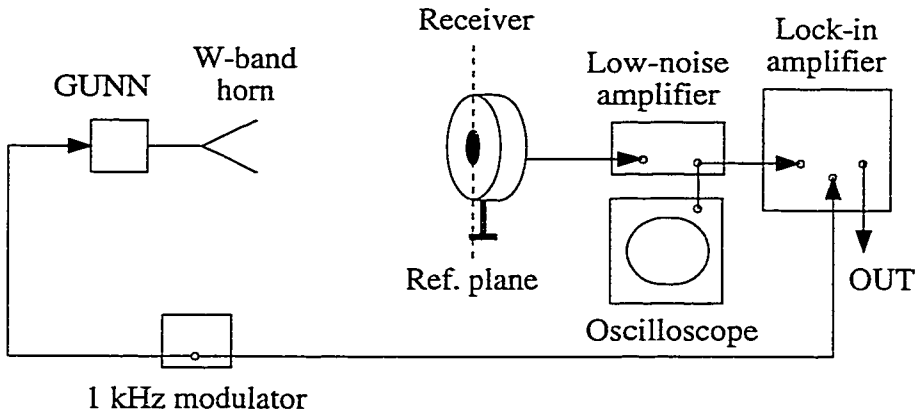

Figure 2.8: Video responsivity measurement set-up.

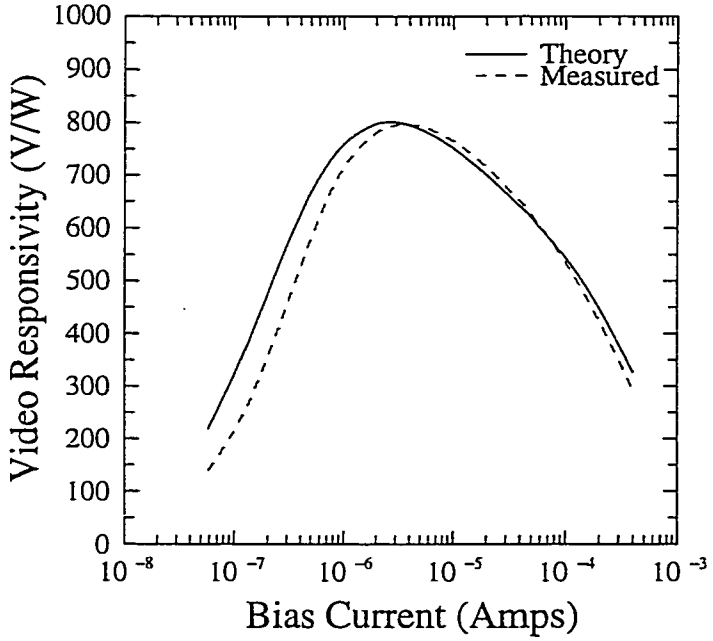

Figure 2.9: Measured and calculated video responsivity at 90 GHz.

terns. The *forward* pattern directivity is calculated to be 22.3±0.2 dB at 94 GHz and 21.3±0.2 dB at 88 GHz by averaging the measured E, H and 45°-plane patterns. The calculated *forward* directivity neglects the radiated power behind the lens and agrees quite well with the theoretical forward directivity [15]. This results in an aperture efficiency (coupling to a plane wave) of 85±4% at 94 GHz for a 12.7 mm diameter silicon lens.

The system video responsivity is defined as the measured low frequency voltage in a 120 $k\Omega$ load divided by the total 94 GHz RF power incident on the 12.7 mm lens aperture (see [33] for more detail). The total RF incident power is calculated by multiplying the incident power density at the plane of the lens by the aperture of the lens. The video responsivity includes the antenna aperture efficiency (coupling to a plane wave, 0.77% at 90 GHz [16]), the antenna backside power loss (0.4 dB), the lens reflection loss without a matching cap layer (1.8 dB) and the absorption loss in the high-resistivity silicon lens (0.7-0.8 dB). The measurement set-up is described in Figure 2.8. The measurements show a high system video responsivity (800±40 V/W) at a bias current of 20 μA (no matching-cap layer was used) due to the good RF match between the double-slot antenna and the planar diode (Fig. 2.9). The video responsivity referenced to the Schottky diode terminals can be calculated by normalizing out the antenna loss and is 2000 V/W.

With this design, it is possible to inject the local oscillator from the back side of the silicon lens. The penalty paid is a 91% loss of the available LO power since the double-slot antenna radiates most of its power into the dielectric lens. In our case, a high-performance quasi-optical set-up is used to inject the LO with minimal loss. The quasi-optical set-up is done using a Martin-Pupplett (MP) interferometer at an IF frequency of 1.4 GHz (Fig. 2.10). An f/1.4 objective Rexolite lens with a 10 cm

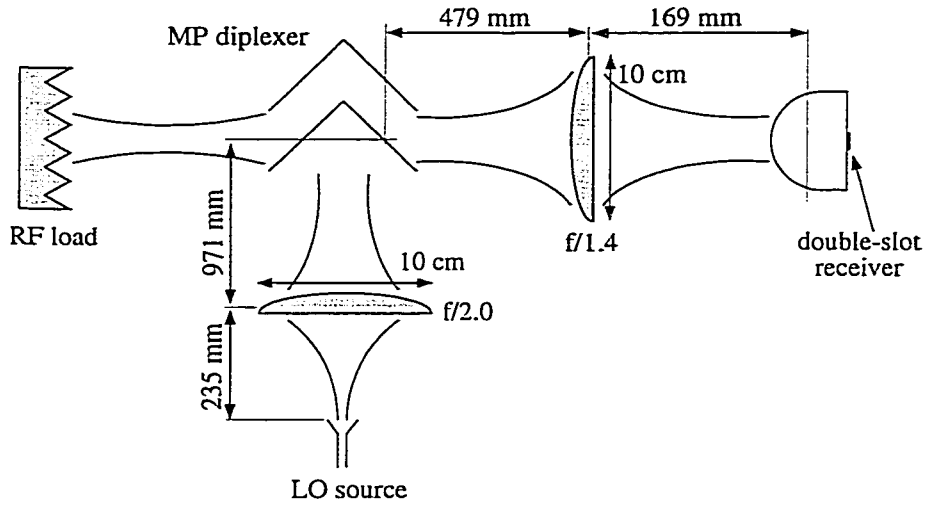

(a)

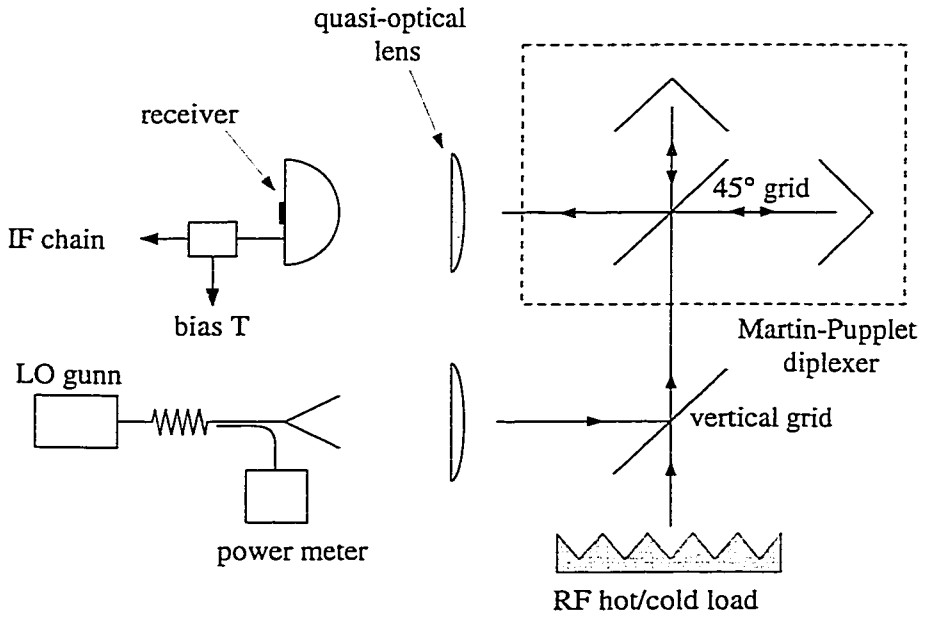

(b)

Figure 2.10: The 90 GHz millimeter-wave quasi-optical setup (a) and measurement set-up (b).

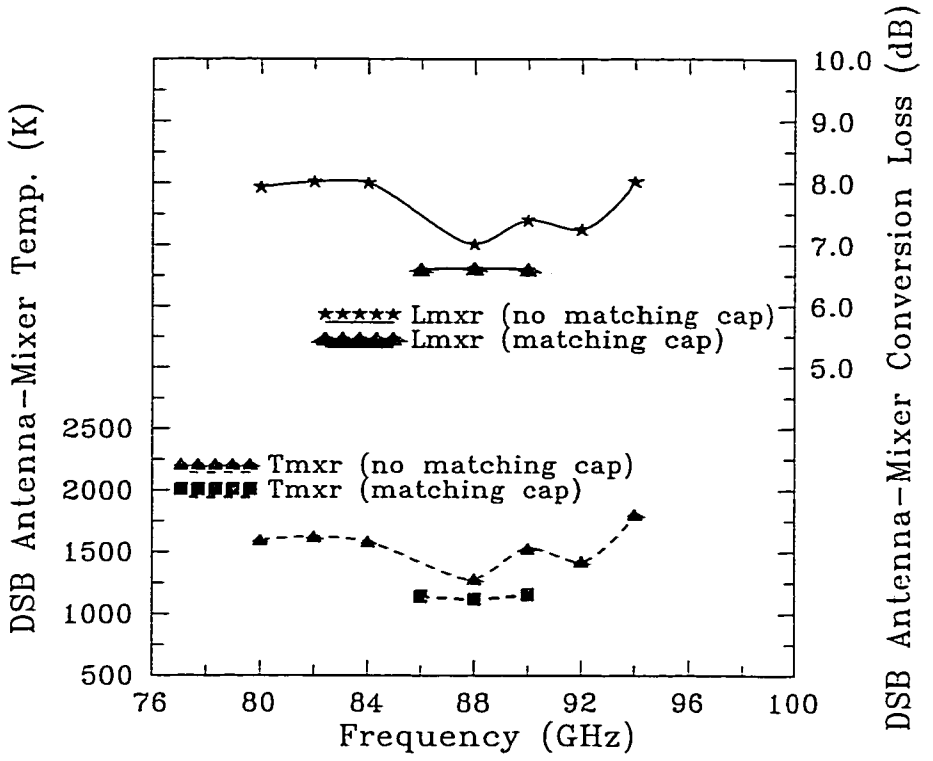

Figure 2.11: Measured DSB conversion loss and noise temperature of the double-slot receiver.

Antenna	
Calculated Back-Side Power Loss	0.4 dB
Calculated Gaussian Coupling Efficiency	0.3 dB
Estimated Lens Absorption Loss	0.7-0.8 dB
Residual Lens-Air Reflection Loss	0.7 dB*
*Can be reduced to 0.4 dB with quarter wavelength matching layer.	
Mixer	
Calculated SSB Diode Conversion Loss	5.5 dB
RF Mismatch between Diode and Antenna	1.5 dB*
*Can be eliminated with better impedance design.	
IF Section	
Calculated IF-Filter Ohmic Loss	0.4 dB*
*Can be eliminated with shorter IF filters.	
Total Calculated SSB Conversion Loss	9.5-9.6 dB
Measured SSB Conversion Loss	9.3±0.3 dB

Table 2.1: A detailed breakdown of the loss mechanism and comparison with measured results at 90 GHz.

diameter is placed 169 mm away from the aperture of the lens. This allows the 5.5 mm Gaussian-beam of the extended hemispherical system to pass unattenuated through the MP diplxer and couple efficiently to the hot-cold load. The local oscillator is transmitted by a standard gain horn and through an f/2 and f/1.4 Rexolite lens (Fig. 2.10). The quasi-optical system is optimized at each measurement frequency by tuning the MP interferometer and slightly changing the distances between the silicon lens and the f/1.4 objective lens. The 1.4 GHz IF chain is composed of a circulator with a cooled load at the isolated port, a bias-T and low-noise amplifiers. The IF chain has a gain of 98.6 dB and a noise-temperature of 94 K with a bandwidth of 100 MHz. The reader is referred to [34] for a detailed description on the calculation of the antenna-mixer performance.

The measured DSB conversion loss and noise temperature are presented in Figure 2.11. The reflection and absorption loss (estimated at 0.45 dB and 0.25 dB,

respectively) of the 10 cm f/1.4 Rexolite objective lens have been normalized out of the measurements. The measured IF reflection is 0.2-0.3 dB and is also normalized out of the measurements [34]. A DSB conversion loss and noise temperature of the antenna-mixer of 7.0±0.3 dB and 1300±50 K is measured without a matching cap layer at 88-90 GHz. The DSB performance improved to 6.3±0.3 dB and 1000±50 K with a non-optimum matching cap layer. The DSB mesurements include the antenna loss to the backside (0.4 dB), the antenna Gaussian coupling efficiency (0.3 dB), the silicon lens absorption loss (0.7-0.8 dB), the lens-air reflection loss (see below), the diode conversion loss and the IF-filter ohmic loss. The non-optimal matching cap layer is melted polyethylene (190 μm-thick, $\epsilon_r = 2.3$) [33] and the conversion loss was improved by 0.7±0.1 dB instead of 1.4 dB due to the incorrect thickness and dielectric constant used. The optimum matching cap layer should be 430 μm-thick for a dielectric constant of $\epsilon_r = 3.4$ ($\epsilon_r = \sqrt{\epsilon_{Si}}$). Therefore, a residual lens-air reflection loss of 0.7±0.1 dB is part of the measured performance at 86-90 GHz with a non-optimal matching cap layer. Also, the use of a matching cap layer reduces internal reflections inside the silicon lens, resulting in the absence of ripples in the measurements (Fig. 2.11).

The best performance was achieved for a DC bias of 0.73 V and a DC current of 2.4 mA. The available optimal LO power at the lens aperture is 5-7 mW. The available LO power at the diode terminals is 2-3 mW after taking into account the total antenna loss. These values are in good agreement with the harmonic balance results. A detailed loss breakdown is given in Table 2.1. It is seen that the measured performance agrees very well with theory. The IF-filter ohmic loss (0.4 dB) is due to the 6 Ω series resistance in the 70 Ω IF circuit and can be eliminated in future designs. The silicon-lens/air reflection loss can be reduced to 0.4 dB with the use

of a correct matching-cap layer. It is seen that the double-slot antenna on a silicon dielectric lens contributes only 1.8 dB of losses to the overall system performance when the correct matching cap layer is used. The quasi-optical double-slot antenna receiver could therefore result in a system with an optimal SSB conversion loss of 7.3 dB (5.5 dB SSB mixer loss and 1.8 dB antenna-lens loss).

2.4 Conclusion

A high-performance millimeter-wave receiver based on a cpw-fed double-slot antenna is described. The geometry is compatible with planar Schottky-diodes and high-speed transistors. The receiver is small, occupying less than 1.1×4 mm of space on a silicon (or GaAs) wafer, but requires a quasi-optical LO injection. The double-slot antenna on an extended hemispherical silicon lens results in a very high Gaussian coupling efficiency (94%), and contributes only 1.8 dB of losses to the overall system performance. The measured SSB system conversion loss at room temperature is 9.3±0.3 dB and is very competitive with non-tuned millimeter-wave waveguide receivers at a fraction of the cost.

CHAPTER III

A 154 GHz UNIPLANAR SUBHARMONIC SCHOTTKY-DIODE RECEIVER

Automotive electronic applications require light, small and low-cost circuits at millimeter-wave frequencies. The current frequency of design for automotive systems is 77 GHz in Europe and other countries (such as USA). The far-field beamwidth of an aperture is given by the Fraunhoffer beam divergence and is $\theta = \lambda/D$, where D is the aperture diameter. Therefore, at this frequency, 15 cm lenses are required to achieve the appropriate resolution at 100 m (1.5^0 3-dB beamwidth). If 154 GHz is used, then the same beamwidth can be achieved using a 7.5 cm lens (Fig. 3.1). This would make the automotive radar much smaller and more practical for modern automobiles.

In this chapter, a 150 GHz uniplanar subharmonic receiver is developed relying on planar antennas and subharmonic mixers. Harmonic mixers downconvert an RF signal which is close to the n-th harmonic of the local oscillator (LO). Subharmonic mixers correspond to the special case where a back-to-back Schottky diode pair is used, and the LO is nearly half of the RF ($n = 2$). Subharmonic mixers result in nearly as good a conversion loss and noise temperature as fundamental mixers. In a subharmonic mixer, the LO can be injected on-wafer, so that large quasi-

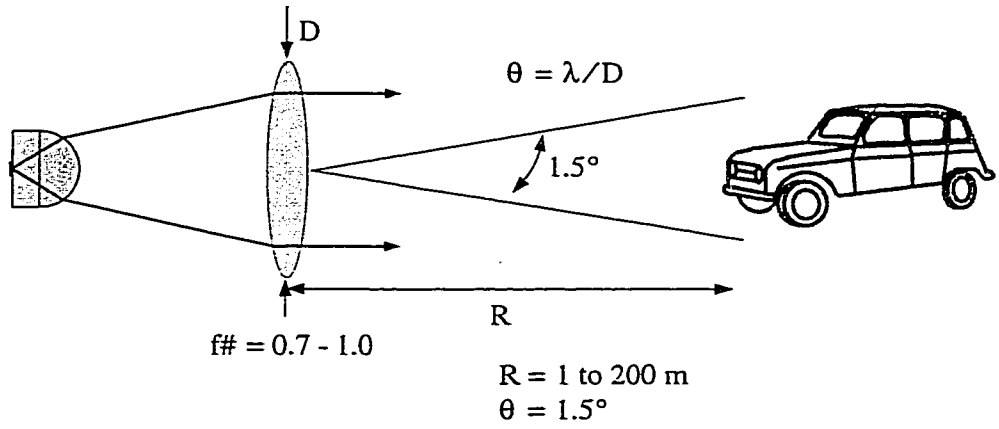

Figure 3.1: A radar for automotive applications: a 3-dB beamwidth of 1.5° is required to resolve a car at 100 m.

optical diplexers are avoided. A double folded-slot antenna is chosen for its low input impedance. The design is compatible with monolithic integration of state-of-the-art Schottky-diodes and high-speed transistors, for millimeter and submillimeter-wave automotive systems.

3.1 Double Folded-Slot Antenna

3.1.1 Antenna Design

In Chapter 2, a double-slot antenna was used in the receiver system. It was seen that the double-slot antenna is simple to design, with an input impedance approximately from 30 Ω to 70 Ω by tuning the slot widths and lengths. However, the double-slot antenna is only compatible with two-terminal devices since the detector is placed in series between the two slots (Fig. 1.5). The slot-ring antenna has been previously described in Chapter 1 and is compatible with three-terminal devices. It can be used with active devices (such as HEMTs) and allows for immediate RF amplification after the antenna. However, the slot-ring antenna is characterized by a high input impedance of around 120 Ω, so it requires a matching network when used

with relatively low input impedance receivers such as Schottky diodes and HEMT amplifiers at 70-150 GHz [21].

The limitations of the double-slot antenna (not compatible with RF amplification) and of the slot-ring antenna (high input impedance) can be overcome with the use of a double-folded slot antenna. The double folded-slot (DFS) antenna is an array of two folded-slot antennas (Fig. 3.2) placed approximately one half dielectric wavelength ($\lambda_d/2$) apart. Each folded-slot antenna acts like a $\lambda_g/2$-long folded cpw line, where λ_g is the guided wavelength, so that the fields in the input and the output ports are 180° out of phase [35]. The two folded-slot antennas are fed in phase using a $\lambda_g/2$-long (180°-long) cpw line, resulting in symmetrical radiation patterns in the broadside direction. However, the physical separation of the antennas should be $\lambda_d/2$ for good radiation patterns in the dielectric, and is therefore shorter than the $\lambda_g/2$ feed line. This problem is easily solved by bending the $\lambda_g/2$ feed line as shown in Figure 3.3. It is also seen that the double folded-slot antenna is fed on one side allowing easy integration of three-terminal devices or MMICs for RF amplification and reception.

The folded-slot antenna is the dual of the folded dipole antenna and therefore has a wide impedance bandwidth. Simulations based on Momentum [31] indicate that the DFS antenna has a very wide impedance bandwidth with a relatively low input impedance of 20-30 Ω. However, the patterns of the DFS antenna degrade away from the design frequency because the folded slots are not fed in phase anymore. The DFS antenna has been used in a 20-22 GHz receiver/radiometer [36], and in the quasi-optical measurement of a 250 GHz planar bandpass filter [37].

The 150 GHz cpw-fed double folded-slot antenna is characterized with a 94 GHz model shown in Figure 3.3. The antenna is placed on a semi-infinite silicon substrate ($\epsilon_r = 11.7$). The folded slots are 33 μm wide and 640 μm long. The DFS center

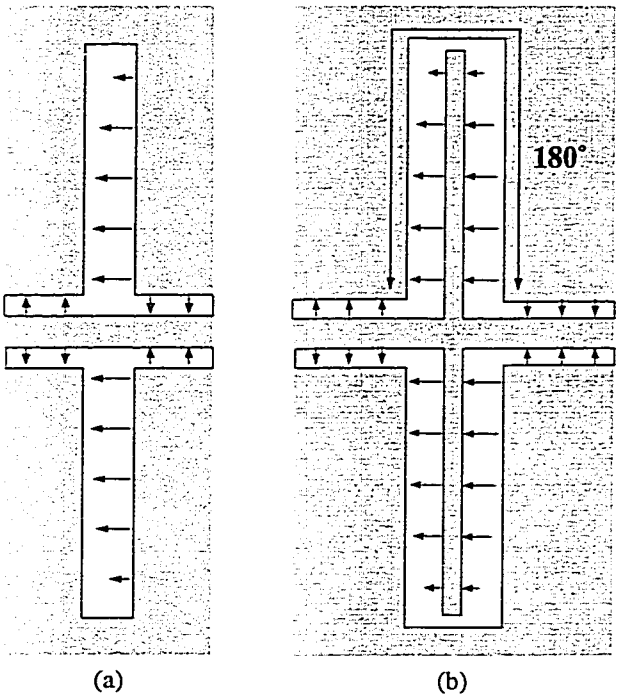

Figure 3.2: Electric field orientations in a regular slot (a) and a resonant folded slot (b). The folded slots are 180° long, and the electric fields undergo a phase reversal at the antenna feed points.

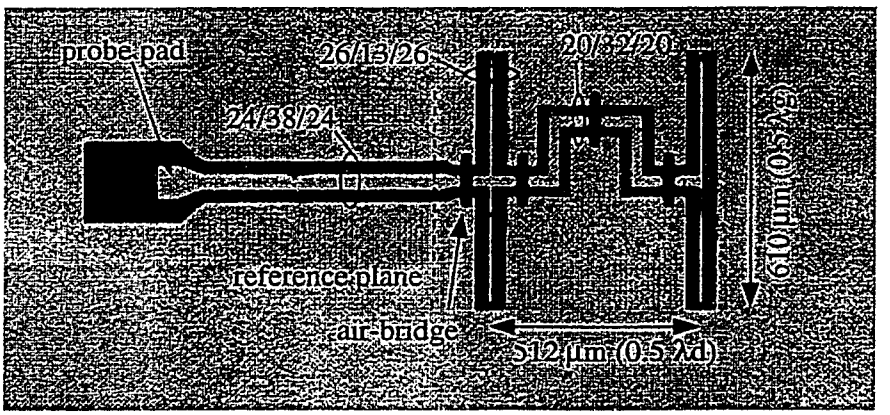

Figure 3.3: Photograph of the fabricated 94 GHz double folded-slot antenna used for input impedance measurements.

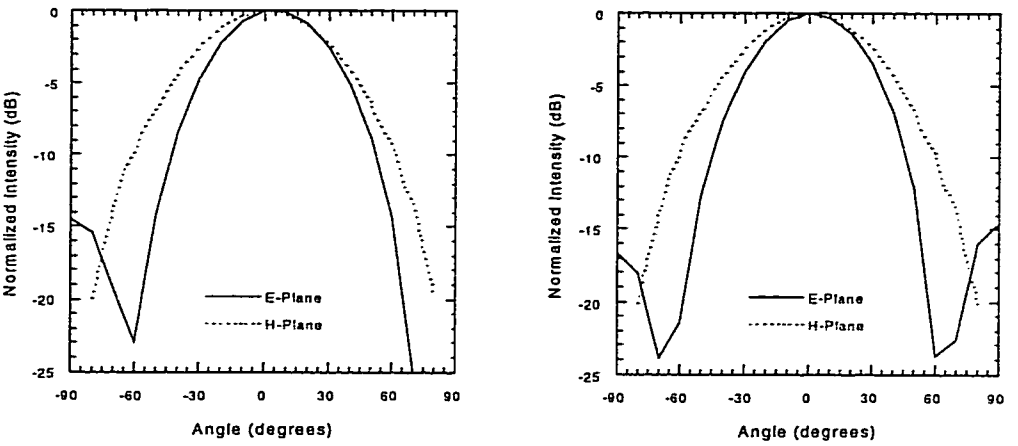

Figure 3.4: Calculated feed patterns of the double folded-slot antenna into the silicon substrate at 94 GHz and 96 GHz.

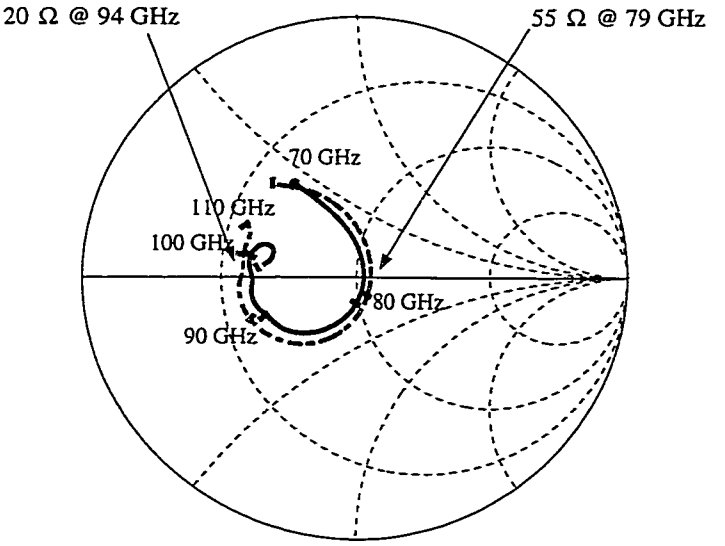

Figure 3.5: Double folded-slot antenna input impedance measured (-) and calculated (- -) from 70-110 GHz.

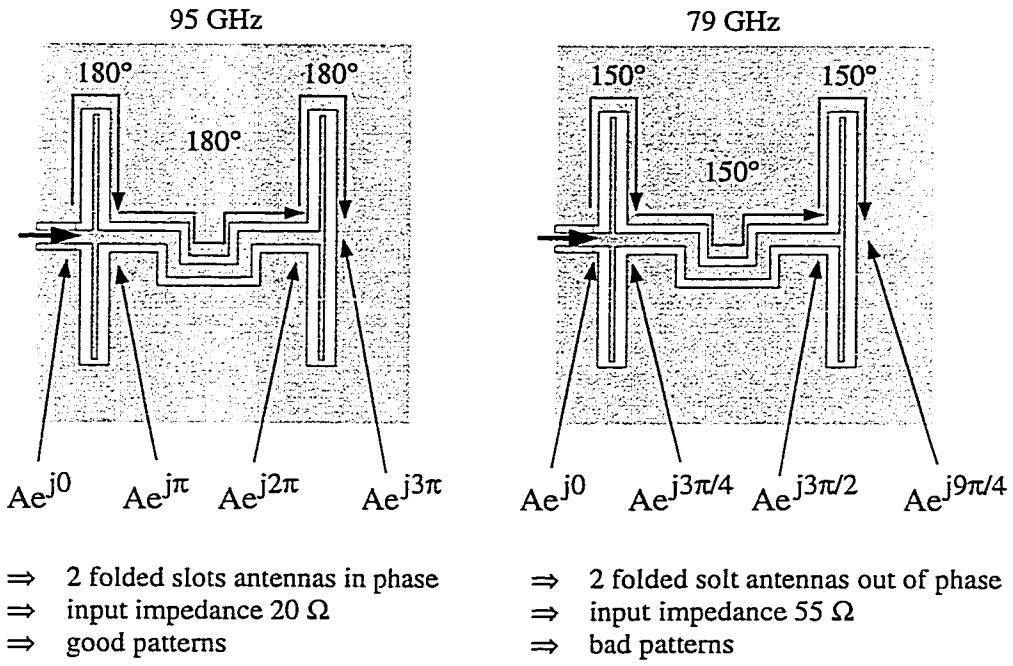

Figure 3.6: Double folded-slot phase conditions at second resonance (94 GHz) and first resonance (79 GHz). The DFS is used at the second resonance for symmetrical patterns.

conductor widths and gaps are 11 μm. The total folded-slot circumference is then 1300 μm corresponding to $1.027\lambda_g$, where λ_g is the quasi-static guided wavelength given by $\lambda_g = \lambda_0/\sqrt{\epsilon_{eff}}$ and $\epsilon_{eff} = (1+\epsilon_r)/2$. The physical distance between the two folded-slots is $0.505\lambda_d$ (472 μm) where λ_d is the dielectric wavelength, given by $\lambda_d = \lambda_0/\sqrt{\epsilon_r}$. The cpw feed line center conductor is 16 μm wide, the cpw gap spacing is 10 μm, corresponding to a 50 Ω characteristic impedance. The total cpw line length is then $0.505\lambda_g$ (640 μm, or 180°) in order to feed the two folded slots in phase as described earlier. Airbridges are required along the feedline to equalize the ground planes and suppress excitation of slot-line mode. The input cpw line has the same dimensions (s=16 μm, w=10 μm) and is a 50 Ω line.

Figure 3.4 shows the calculated feed patterns inside the dielectric substrate at 94 GHz and 96 GHz. The main and side lobes are symmetrical at 96 GHz, which is

an indication that both antennas are fed in phase (and the feed line is 180°-long). At 94 GHz however, the feed patterns are suffering from a slight phase difference between the two slots.

3.1.2 70-110 GHz Impedance Measurements

The 94 GHz double-folded slot antenna is fabricated on a 540 μm thick, high-resistivity silicon substrate. The cpw ground plane and center conductor are 6000 $\AA$ of evaporated gold, or approximately 2.5 skin-depths at 94 GHz. The 25 μm wide airbridges are 4 μm thick electroplated gold 3.5 μm high above the cpw line. The double-folded slot input impedance is measured on-wafer from 70-118 GHz using a W-band HP8510 network analyzer. The network analyzer is calibrated at the antenna input ports using TRL calibration techniques [38]. The antenna is placed on a 13 mm thick Stycast [29] spacer ($\epsilon_r = 12$) and the internal reflections inside the block are eliminated using time-transform and time-gating. The double-folded slot was simulated using Momentum [31] with a semi-infinite silicon substrate, and the air-bridges were included in the simulation. Figure 3.5 shows the simulated and measured input impedance from 70-110 GHz. The double-folded slot shows a very wideband low input impedance of 20±j20 Ω from 90-110 GHz, with excellent agreement between theory and experiment (Fig. 3.5). The double folded-slot antenna is then an attractive solution for wideband millimeter-wave circuits that include low-impedance detectors (Schottky diodes, SIS junctions) and amplifiers (HEMTs).

Figure 3.5 shows that the DFS antenna is used at the second resonance like most planar antennas, for the wider bandwidth that is provides. The input impedance of the double folded-slot antenna is 20 Ω at 94 GHz, and close to 50 Ω at 79 GHz. However, at 79 GHz, the feed line and the two folded-slots are approximately 215°

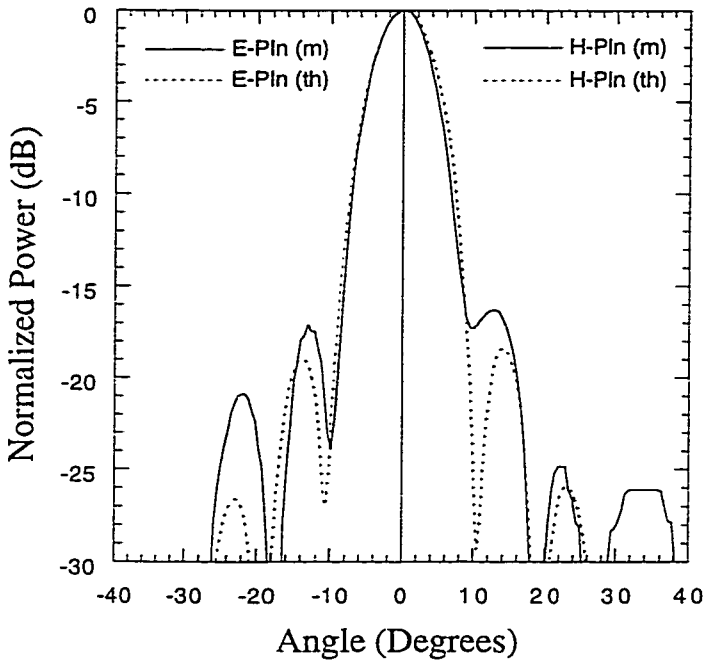

Figure 3.7: Comparison between measured and calculated E- and H-plane patterns at 94 GHz.

long instead of 180° long at 94 GHz, which means that the two folded-slot antennas are not fed in phase, resulting in poor and non-symmetrical radiation patterns despite a good impedance match (Fig. 3.6). The double folded-slot antenna at its second resonance is a *low* input impedance antenna (20 Ω at 94 GHz), providing excellent broadside patterns.

3.1.3 90-100 GHz Radiation Patterns Measurements

The far-field radiation patterns of the double folded-slot antenna were measured by Prof. Sanjay Raman at 94 GHz [39]. The double folded-slot antenna is integrated with an RF 60 Ω bolometric detector placed 250 μm away from the antenna port with a 2000 $\AA$-thick layer of SiO was also used between the bolometer and the silicon substrate for thermal isolation. The RF choke is provided by two capacitors located $\lambda_g/4$ and $3\lambda_g/4$ away from the bolometer. The video responsivity of the RF

bolometer detector is 5 V/W at a bias of 1 mA and a video frequency of 1 kHz. The circuit was placed on the backside of a 24 mm diameter silicon extended hemispherical lens, at the second focal plane of the synthesized elliptical lens. No matching cap layer was used at the air-dielectric interface.

The double folded-slot antenna radiation patterns were measured from 90-100 GHz. Figure 3.7 shows a comparison between the measured DFS radiation patterns at 94 GHz and theoretical radiation patterns for an equivalent double-slot antenna. The most symmetric patterns are obtained at 94 GHz, while they become asymmetric at frequencies above and below, due to the degradation of the DFS pattern into the dielectric lens. The -3 dB and -10 dB beamwidths are 8° and 16°, respectively, at 92 GHz, and decrease as frequency increases. The co-polarized directivity calculated from the measured radiation patterns at 94 GHz is 27.2±0.2 dB, corresponding to a maximum aperture efficiency of 92±3%. The sidelobe levels remain below -15 dB from 92-100 GHz. The double-folded slot antenna backed with the dielectric lens hence results in a diffraction limited beam at 94-96 GHz. It provides a comfortable 10% measured pattern bandwidth from 90-100 GHz.

3.2 Receiver Design

3.2.1 150 GHz DFS Antenna

The DFS antenna scaled to 150 GHz is 380 μm long ($0.5\lambda_g$ or 180° at 154 GHz), with a separation of 320 μm ($0.5\lambda_d$) (Fig. 3.8). As seen in the previous section, it results in good patterns and also low cross-polarization levels ($\leq$-23 dB) [35]. The simulated input impedance of the DFS antenna using EESOF Momentum [31] is 20+j1 Ω at 154 GHz (Fig. 3.8). The DFS antenna presents two advantages: it has a very wideband input impedance which is around 20 Ω and is an excellent match to

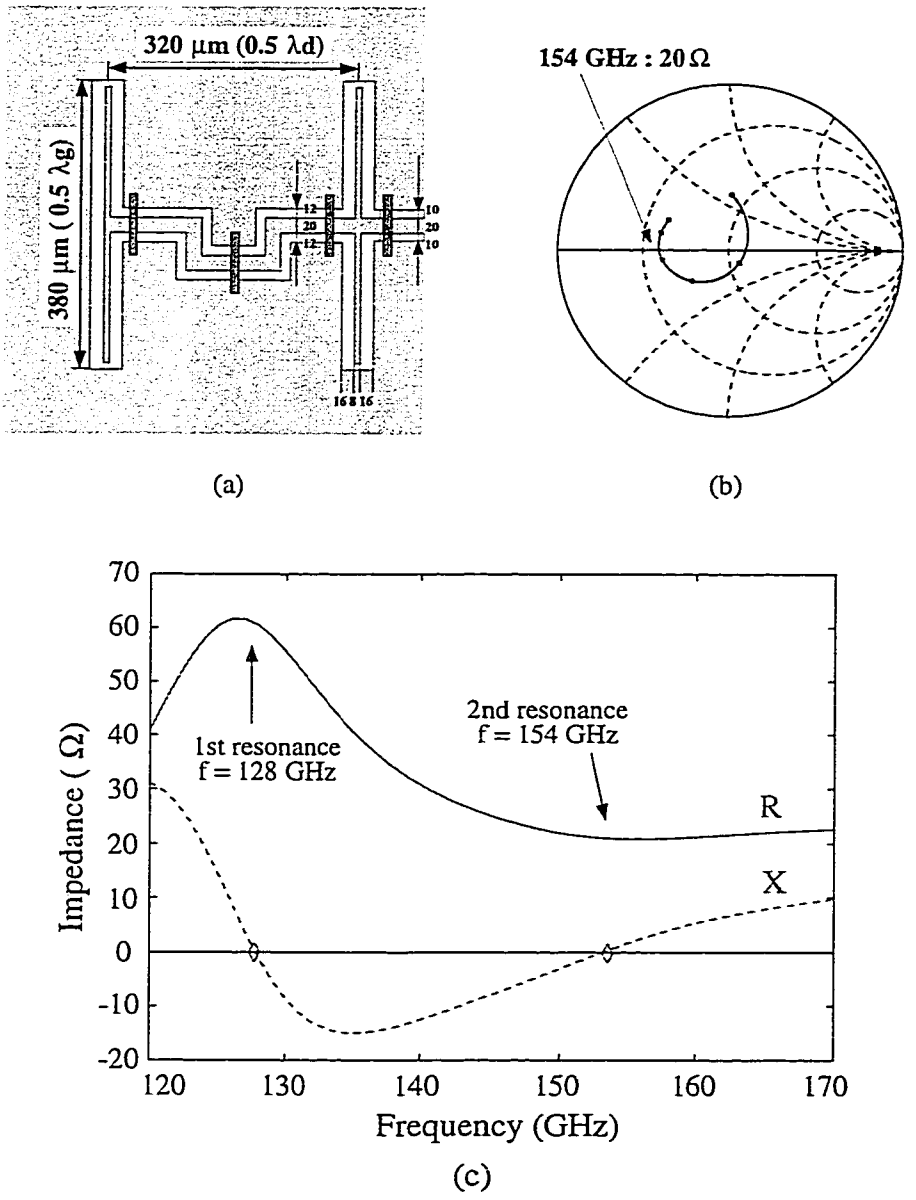

Figure 3.8: The 150 GHz double folded-slot antenna dimensions (a), S11 (b) and input impedance (c) simulated using Momentum from 140 GHz to 170 GHz (c). The input impedance is 20+j1 Ω at 154 GHz.

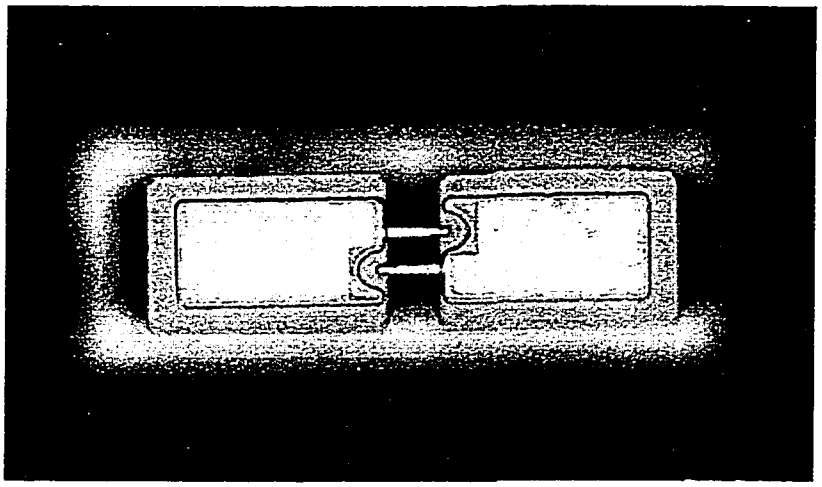

Figure 3.9: Picture of the University of Virginia SCT1T7-D20 Schottky diodes.

the diode RF impedance (22-j28 Ω). Furthermore, the DFS antenna is a DC open circuit, and no DC filter is needed in the RF line to block the DC bias component of the diode.

3.2.2 Diode

The subharmonic receiver is based on a Schottky diode mixer provided by the University of Virginia (SCT1T7-D20), and consists of two back-to-back diode junctions (Fig. 3.9) with very low junction and parasitic capacitances (C_{j0}=2.5 fF, C_p=11 fF). The DC parameters are obtained by curve fitting from the measured IV curve and are R_s=6.5 Ω, n=1.163, Φ_b=0.842, γ=0.5, and $I_0 = 4 \times 10^{-14}$ A, resulting in a figure-of-merit cutoff frequency of $f_c = 1/2\pi R_s(C_{j0} + C_p)$=1.8 THz. The RF, LO and IF input impedances of the diode are simulated using an adapted version of Kerr's subharmonic mixer analysis [28, 30] and are: Z_{RF}=22-j30 Ω, Z_{LO}=37-j100 Ω, and Z_{IF}=100-120 Ω at an RF of 154.2 GHz, an LO power of 77 GHz and an IF of 0.2 GHz, respectively. The minimum SSB conversion loss for such a diode is simulated to be 8.5-9.0 dB at a 2-4 mW of available LO power, over the 150-154 GHz

range. In this case, the RF (LO) port impedance is taken to be 20 Ω (50 Ω). The IF port is taken to be matched to 100 Ω, and no matching networks are used.

3.2.3 Mixer Design

The mixer design is very compact (2×2 mm) and LO and RF matching networks are not included for simplicity (Fig. 3.10). The 70-85 GHz LO signal is injected on-wafer with a W-band picoprobe, and is shorted at the RF port by a 417 μm long ($\lambda_{gLO}/4$) open stub. The RF line between the DFS antenna and the diode is 800 μm long (λ_{gRF}), which has 0.8 dB of insertion loss. The RF signal is shorted at the LO port by a 420 μm ($\lambda_{gRF}/2$) long shorted stub. The shorted stub also provides the DC and IF short. The RF choke consists of two 0.2 pF capacitors placed $\lambda_{gRF}/2$ apart in the IF port, resulting in a 10 GHz cut-off frequency. The 0.1-2.0 GHz IF signal is also extracted on-wafer using a K-band probe. The design takes into account the packaged diode feeding lines which are estimated to be 70° (or 35°)-long at the RF (or LO) frequency. The substrate is high resistivity Silicon ($\epsilon_r = 11.7$) capped by 2500 Å of Si_3N_4, resulting in an effective dielectric constant of $\epsilon_{eff} = 6.0$ at 77 GHz and 154 GHz. In all cases, the cpw line impedance is 52 Ω (s=24 μm and w=15 μm). The cpw attenuation was measured at 70-110 GHz, and the extrapolated loss at 150 GHz is 0.9 dB/mm. Figure 3.10(a) shows the layout and Figure 3.10(b) the impedance environment of the complete subharmonic receiver, with the RF, LO and IF regions.

The network is simulated with Momentum [31] in order to calculate the input impedances presented by the network at the diode ports at IF, LO and RF frequencies. As mentionned before, the calculated RF, LO and IF impedances of the back-to-back diodes alone are 20-j30 Ω, 37-j100 Ω and 120 Ω, respectively, for matched RF,

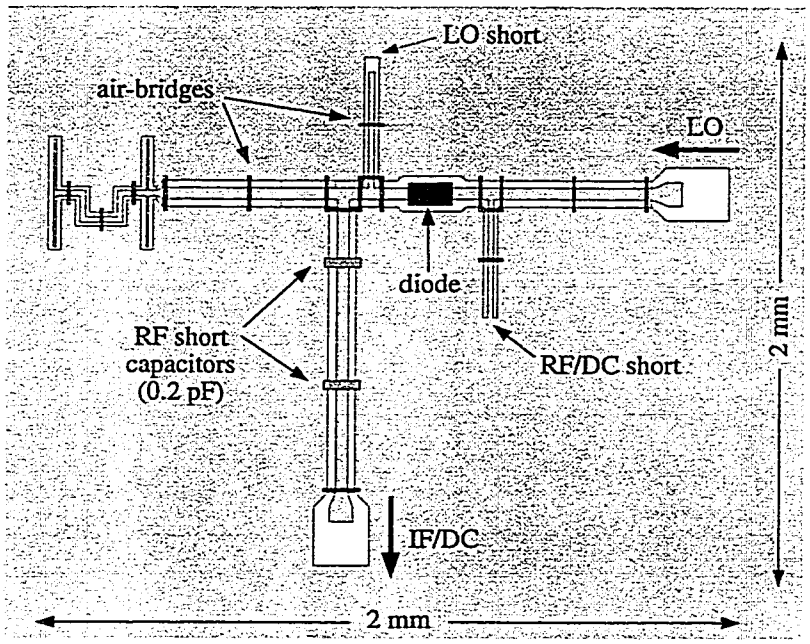

(a)

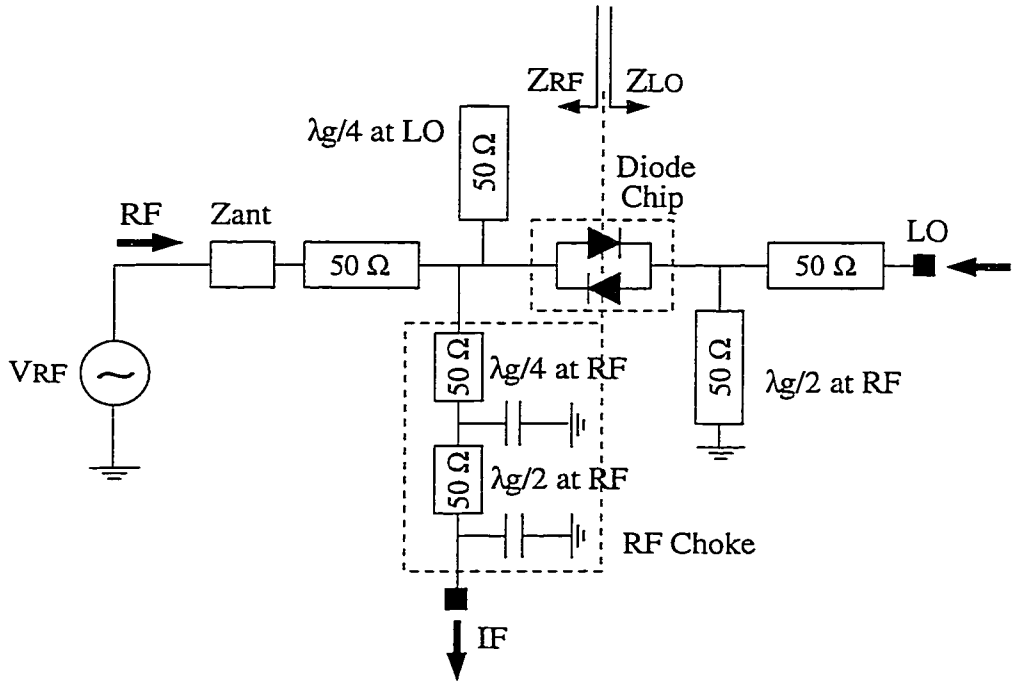

(b)

Figure 3.10: The layout of the subharmonic mixer (a) and impedance environment (b).

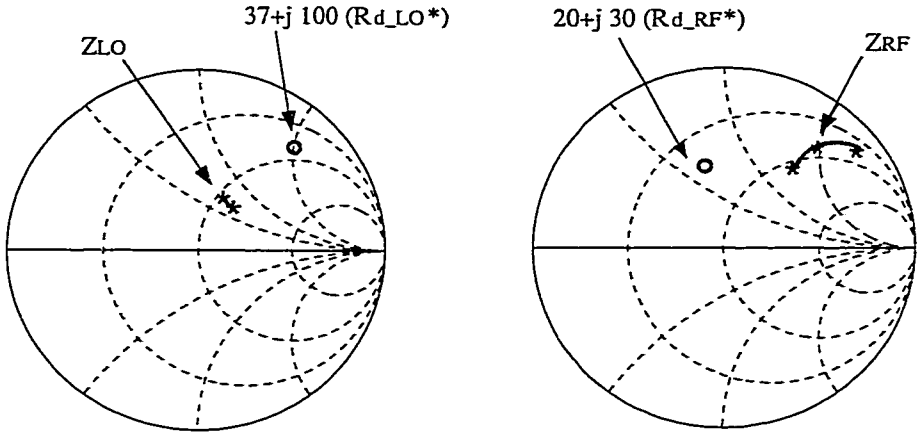

LO network impedance
70-80 GHz
(a)

RF network impedance
150-160 GHz
(b)

Figure 3.11: Method-of-Moment simulations of the input LO (a) and RF (b) impedances presented by the circuit at the diode junctions. R_d^* is the conjugate of the diode impedance.

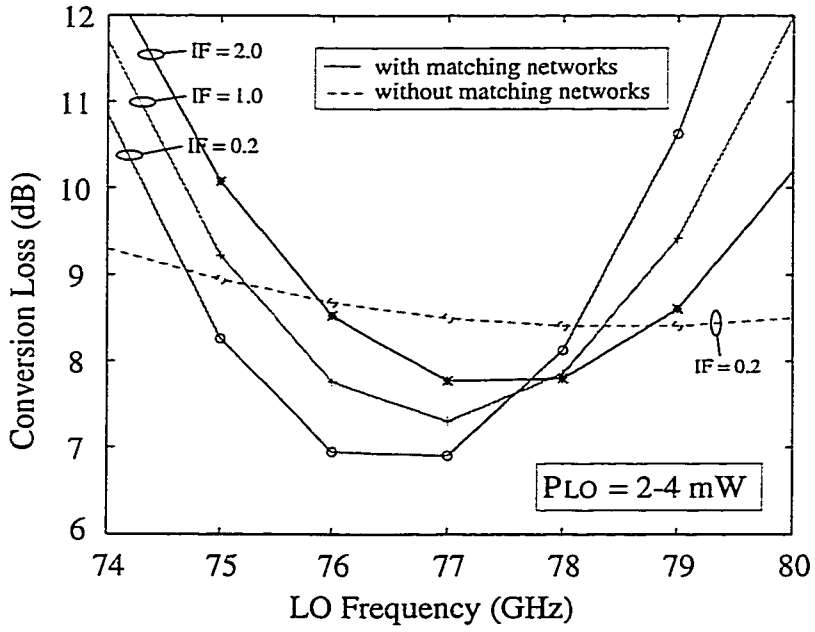

Figure 3.12: Calculated SSB conversion loss for a 148-180 GHz RF and a 0.2-2.0 GHz IF with and without matching networks.

LO and IF conditions. At the RF frequency, the network is designed by first simulating the shorted stub on the LO side (the RF short) and then adding the diode RF input impedance in series with the stub impedance. Second, the RF network, which includes the DFS antenna, the cpw line, the LO short and the IF-port T-junction, is designed to present the conjugate match impedance. Notice that the shorted stub and the diode feeding lines have a significant influence on the input impedance and cannot be neglected. The LO network is designed in a similar approach.

Figure 3.11 shows the deembedded input impedances of the RF and LO networks at the diode junctions. It is seen that the RF and LO input impedances present a good match to the diode RF and LO input impedances, respectively, and therefore matching networks are not included. Figure 3.12 shows the calculated SSB conversion loss of the diodes when the RF and LO network input impedances are well matched to the diode input impedances. The calculated SSB conversion loss is 7-8 dB at 152-154 GHz for an IF of 0.2-2.0 GHz. However, matching networks introduce additional cpw line losses (around 1.0 dB) and reduce the bandwidth of operation. It has therefore been decided to design a wideband subharmonic receiver and matching networks were not included. The simulated SSB conversion loss with no RF and LO matching networks is 9.0±0.5 dB at 148-160 GHz for an available LO power of 2-4 mW.

3.3 Millimeter-Wave Measurements

3.3.1 Receiver Fabrication

The receiver is built using standard photolitographic techniques, and the metalization is 6000 Å of evaporated gold (3 skin depths at 150 GHz). The cpw grounds are equalized with electroplated air-bridges (20 μm wide, 3 μm thick, 3 μm high), and

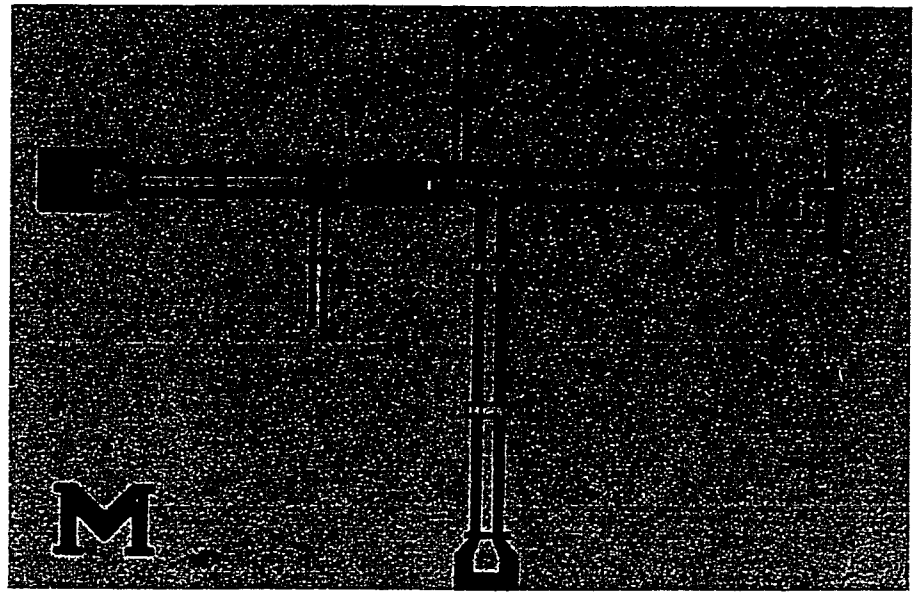

Figure 3.13: Picture of the fabricated subharmonic receiver. Dimension are given in the text in Section 3.2.

the Schottky diode is connected to the cpw lines using Epo-Tek H20E silver epoxy. The receiver is placed on the back side of a 12.7 mm-diameter extended hemispherical silicon lens. The extension length is 2450 μm to reach an intermediate position close to the elliptical position, whith a coupling to a Gaussian beam of 91% and a directivity of approximately 25 dB. A $\lambda_m/4$-thick stycast matching-cap layer was used to reduce the silicon lens reflection losses, where $\lambda_m = \lambda_0/\sqrt{\epsilon_m}$ and $\epsilon_m = \sqrt{\epsilon_r}$. The matching cap layer was fabricated by Janos Technologies [40] by coating the silicon lens with stycast ($\epsilon_r = 4$). The coating was dried and thinned to the proper thickness of 260 μm using laser machining.

A complete view of the receiver on the lens is shown in Figure 3.14. The 70-85 GHz LO is injected using a W-band Picoprobe (model 120-GSG-150-BT) with an insertion loss of 1.25 dB (Fig. 3.15). The IF chain is calibrated at 0.2 GHz and 1.4 GHz, with a gain and noise temperature of 93.8 dB and 110 K, and 93.6 dB and 103 K, respectively.

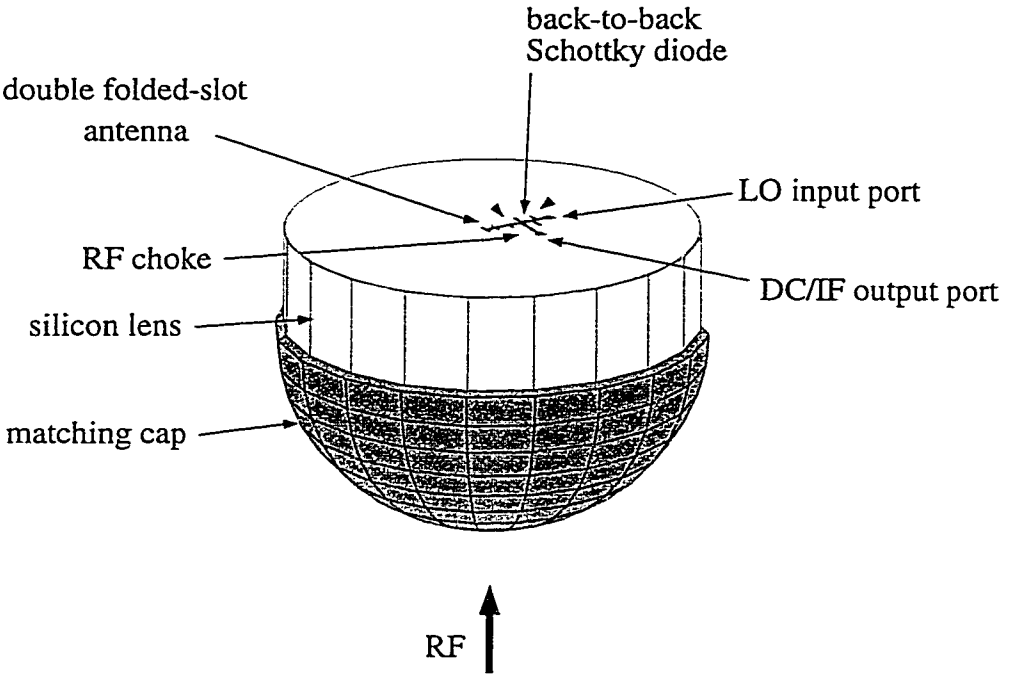

Figure 3.14: View of the complete subharmonic receiver.

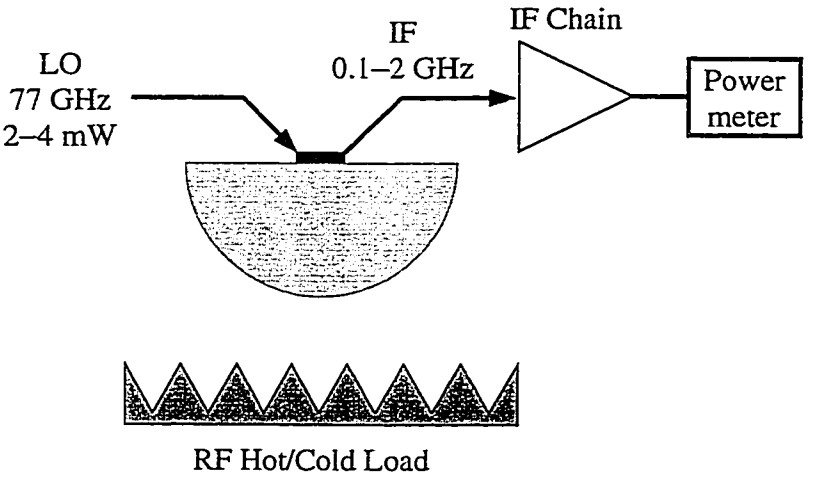

Figure 3.15: W-band measurement set-up for conversion loss measurements.

3.3.2 150 GHz Radiation Patterns Measurements

The far-field radiation patterns of the double folded-slot antenna placed nearly at the elliptical position of a 12.7 mm diameter silicon lens are measured at 150-154 GHz. The diode is biased at 0.860 V for a current of 100 μA. The RF source is a 77 GHz GUNN oscillator used with a frequency doubler. The RF signal is modulated at 1 kHz, and the detected signal is measured using a lock-in amplifier. Figure 3.16 shows the measured E- and H-plane patterns at 150 GHz and 154 GHz. The patterns are symmetrical even with the presence of small amounts of spurious radiation down to the -17 dB level, attributed to the cpw feed line and cpw stubs in the RF circuit. The -3 dB and -10 dB beamwidths are 8° and 15° at 154 GHz, resulting in a co-polarized directivitiy of 27.2±0.2 dB, calculated by averaging the measured E and H-plane patterns, and a maximum aperture efficiency of 92±3%. The sidelobe levels remain below -15 dB at 150-154 GHz and the measured cross-polarization levels in the E- and H-planes are below -25 dB.

3.3.3 140-170 GHz Conversion Loss Measurements

The subharmonic receiver DSB conversion loss and noise temperature are measured using the hot/cold load method for an IF frequency of 0.2 GHz and 1.4 GHz and are presented in Figure 3.17. A receiver DSB conversion loss of 12±0.5 dB is measured at 144-152 GHz, for an available LO power of 8-10 mW at the probe tip. The conversion loss is less than 13 dB at 140-170 GHz, resulting in a 20% bandwidth. The measured DSB system noise temperature is 4500±1000 K at 140-170 GHz, and 4000±500 K at 144-152 GHz for a room temperature system. Figure 3.17 shows that 7-10 dBm (5-10 mW) of available LO power are to pump the diodes for optimal conversion loss.

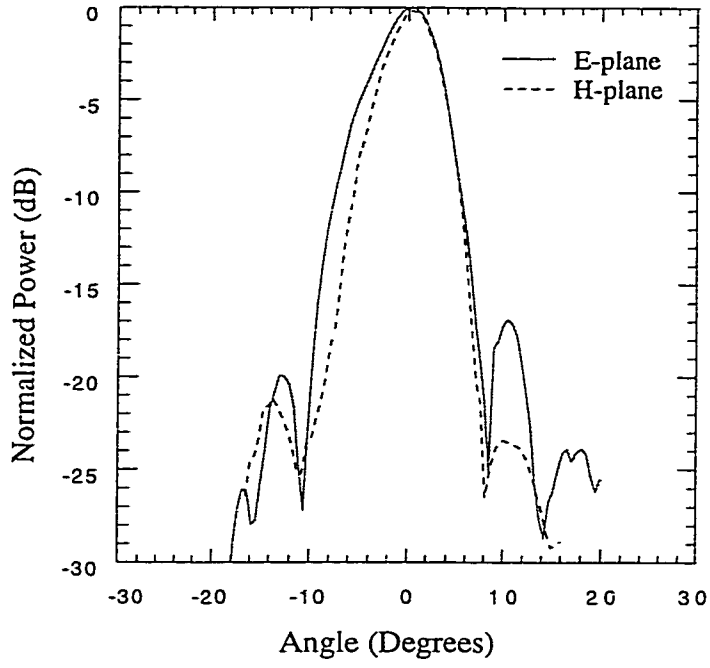

(a)

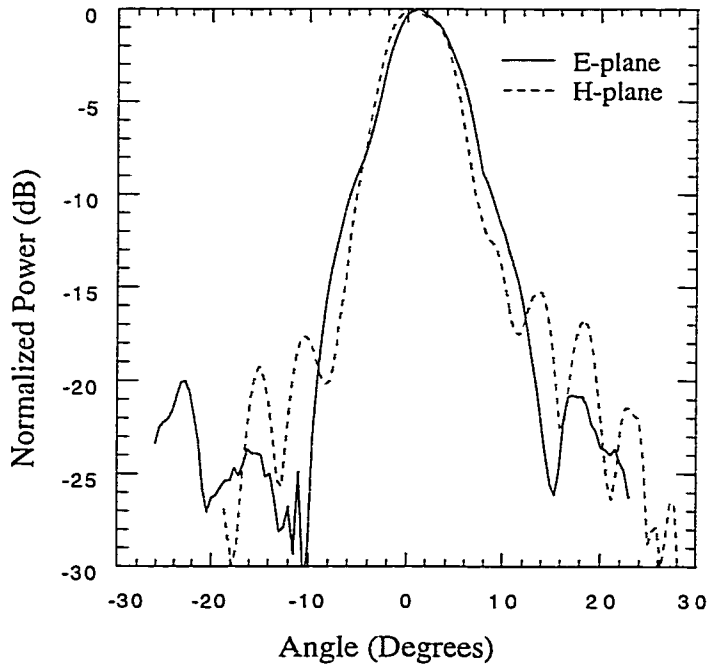

(b)

Figure 3.16: Measured E- and H-plane patterns at 150 GHz (a) and 154 GHz (b). The measured cross-polarization levels in the E- and H-planes were below -25 dB.

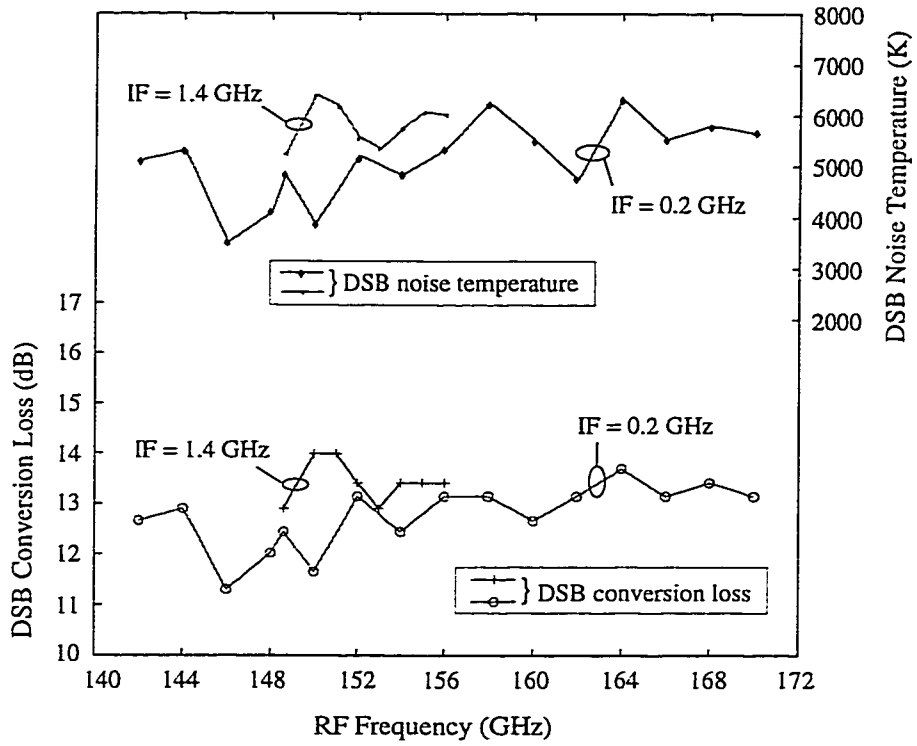

(a)

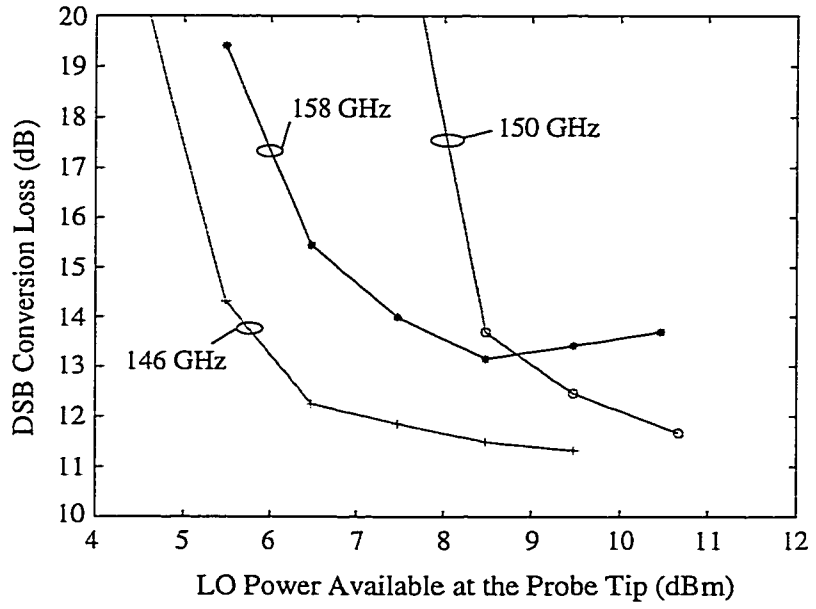

(b)

Figure 3.17: Measured DSB conversion loss and noise temperature of the subharmonic receiver versus frequency at 142-170 GHz for an IF frequency of 0.2 GHz and 1.4 GHz (a), and DSB conversion loss versus LO power available at the probe tip at 146 GHz, 150 GHz and 158 GHz (b).

DFS Antenna and Dielectric Lens	
Calculated Back-Side Power Loss	0.5 dB
Estimated Lens Absorption Loss	1.1 dB
Residual Lens-Air Reflection Loss	1.0 dB
DFS Ohmic Loss	1.0^{+} dB
Mixer	
Calculated SSB Diode Conversion Loss	9.0 dB
RF CPW Attenuation Losses	0.8 dB
IF Section	
IF Probe and Atternuation Losses	0.2-0.3 dB
Total Calculated SSB Conversion Loss	$13.7\text{-}13.8^{+}$ dB
Measured SSB Conversion Loss	15±0.5 dB

Table 3.1: A detailed breakdown of the loss mechanism and comparison with measured results at 140-170 GHz.

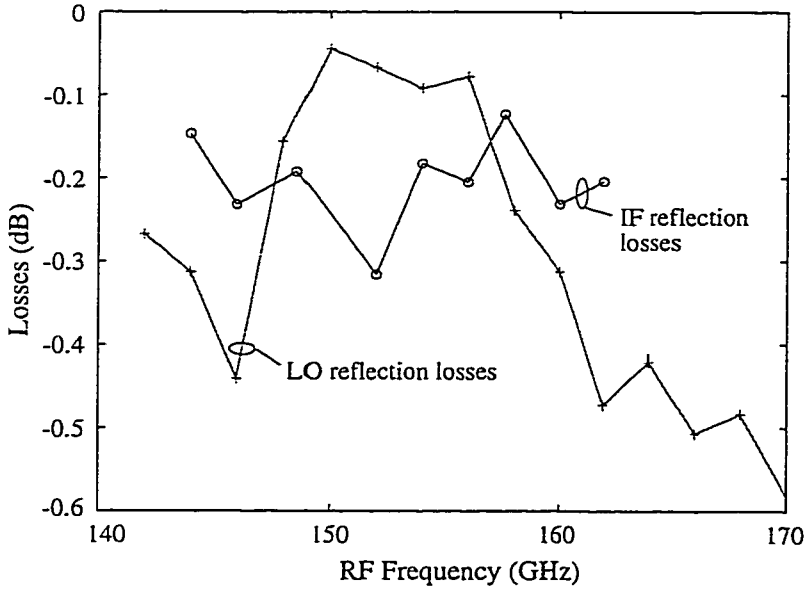

Figure 3.18: Measured LO and IF mismatch losses.

The measurement includes the IF mismatch and probe losses (0.2-0.3 dB) as seen in Figure 3.18, the backside radiation losses (calculated to be 0.5 dB) and the silicon lens absorption losses, calculated to be 1.1 dB. The absorption of high-resistivity silicon is 0.145 Np/cm at 150 GHz [41]. Also, the cpw attenuation loss between the antenna and the mixer is included in the measurement and is estimated to be 0.8 dB at 150 GHz. The ripples in the measurements indicate the matching-cap layer is not optimum and the reflection losses at the silicon/air interface are estimated to be 1.0 dB. The measurement does not include Gaussian coupling efficiency loss (0.4 dB) because the receiver is coupled directly to a hot/cold load and not through a plastic lens quasi-optical system. The total calculated losses are then 13.7 dB SSB including the ohmic losses in the DFS antenna, estimated to be 1.0 dB (due to the small dimensions of the folded slots), but not including the losses of the stubs before and after the diodes. This compares well with the measured 15$\pm$0.5 dB SSB conversion loss. These results are summarized in Table 3.1.

The difference between calculation and measurements may be attributed to ohmic losses in the DFS antenna. The folded-slots have been designed with very small center conductor width (8 μm center conductor and 16 μm spacing) resulting in relatively high ohmic losses at 150 GHz, estimated to be 1.0^{+} dB. In future designs, the double folded-slot antenna should have larger dimensions, around 30/15/30 μm.

3.4 Conclusion

A planar integrated subharmonic receiver has been developped at 140-170 GHz. The receiver shows a wideband DSB conversion loss of 11.5-13.5 dB at 140-170 GHz due to the wideband low input impedance of the antenna (20$\pm$j20 Ω), which presents a good match to the subharmonic diode input impedance (22-j30 Ω). The receiver

is coupled with a silicon lens, which contributes up to 2.6 dB of losses to the overall performance (1.1 dB of absorption, 0.5 dB of backside radiation and 1.0 dB of reflection losses). The receiver layout allows for RF amplification before downconversion with the use of appropriate HEMT amplifiers. The local oscillator can be integrated on-chip at 77 GHz, resulting in a low-cost uniplanar monolithic receiver for future automotive applications.

CHAPTER IV

MICROSTRIP ANTENNAS ON SYNTHESIZED LOW DIELECTRIC CONSTANT SUBSTRATES

As was mentionned in Chapter 1, microstrip antennas on high dielectric constant substrates (GaAs, Silicon) suffer from very narrow bandwidths (less than 2%), low efficiency and poor radiation patterns due to surface waves. Several methods were recently used to overcome this problem, including drilling a well designed cavity underneath the antenna [42], complete or partial etching of the substrate underneath the antenna [34, 43, 44] and etching few holes underneath the antenna to disturb the formation of substrate modes [45, 46].

In this chapter a rather new approach is described. The idea is to etch a series of very closely spaced holes ($\leq \lambda_d/10$) underneath and around the microstrip antenna, and to control the synthesized dielectric constant with the choice of the diameter and spacing of the holes. The period of the holes must be small compared to a wavelength so that quasi-static techniques result in a good estimate of the synthesized dielectric constant. The hole diameter is around 0.1-0.2λ_d, or 300-600 μm at 30 GHz and 100-200 μm at 90 GHz which is compatible with state-of-the-art via-hole formation available in MMIC processing. The via-hole approach and the associated localized reduction of the dielectric constant is also applicable to a variety of planar antennas

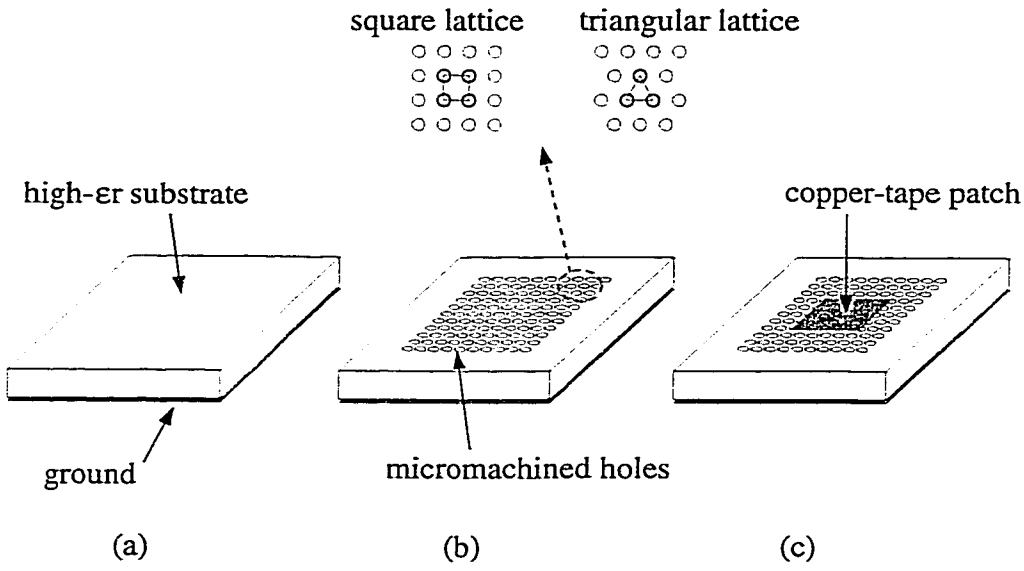

Figure 4.1: Procedure to realize low-ϵ_r regions: the high-ϵ_r substrate (a) is drilled in a local area on a rectangular or triangle lattice (b). The patch is made out of copper tape (c).

and antenna arrays such as microstrip dipoles, slot antennas and low gain Vivaldi antennas. In the first part of the chapter, the principle is demonstrated on 4 GHz microstrip antennas on thick dielectric substrates with high-ϵ_r, and two methods to measure the synthesized dielectric constant are compared: the quasi-static capacitance measurement, and the measurement of the frequency of resonance of a patch. In the second part of the chapter, the technique is used on 13 GHz microstrip antennas on high ϵ_r Duroid substrates with the measurements of the bandwidth, radiation efficiency and radiation patterns.

4.1 The Micromachining Approach

A simple way to synthesize low-dielectric constant regions in a high- dielectric constant substrate is to remove dielectric using adapted micromachining. On silicon (or GaAs), wet etching micromachining processes (TMAH, KOH) are convenient to create small holes or cavities which do not require high precision. Typically,

50-100 μm features can be easily obtained on 100-500 μm-thick substrates, with a precision of ± 5 μm. These processes are particularly interesting for cavities below a patch antenna or a transmission line, because they result in flat and smooth surfaces with a well controlled depth, accurate to ± 10 μm. These cavities can be metallized afterwards. On Duroid substrates, however, the use of a computer controlled milling machine is more adapted because of the dielectric soft texture. Very good precision is achieved in drilling small holes with today's numerically controlled machines.

For this study, the idea is to etch closely spaced holes, small compared to the wavelength, in a limited region underneath and around a patch antenna on a high-ϵ_r substrate. Figure 4.1 shows the steps to the realization of synthesized low-ϵ_r substrates. The hole dimension and density determine the synthesized dielectric constant. Also the hole lattice can be chosen to be square, triangular or hexagonal (Fig. 4.1). As will be seen later, this is not important since the dominant mechanism is the volumetric removal of the underlying substrate and the reduction of the effective dielectric constant. The patch antenna is then made out of copper tape and mounted on top of the synthesized region.

4.2 Quasi-Static Measurements of the Effective Dielectric Constant

In order to prove the quasi-static approach on closely spaced holes, a number of microstrip antennas on a dielectric substrate with different hole densities have been fabricated. The substrate is a Duroid $\epsilon_r = 10.5$, h=1.27 mm (50 mils). The resonant frequency, f_r, of the microstrip antennas of length and width L and W, respectively, was measured with a network analyzer. The effective relative dielectric constant ϵ_{reff}

L (cm)	2.18	1.47	1.54	1.50	1.07
W (cm)	2.66	2.13	2.13	2.14	1.47
f_r (GHz)	4.3	5.5	5.2	4.2	4.3
ϵ_{reff} Resonance method	2.3	3.0	3.2	5.4	10.5
ϵ_{reff} Capacitance method	2.5	3.3	3.5	6.3	10.5

Table 4.1: Comparison between the two methods to measure dielectric constants for different machined hole densities. The last column indicates measurements with no drilled holes.

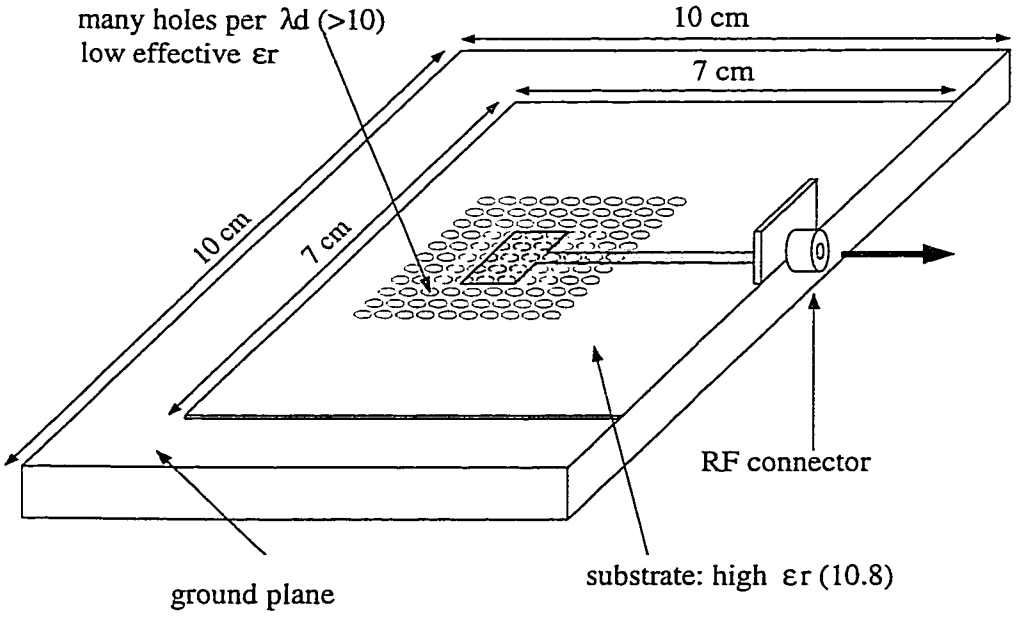

Figure 4.2: Microwave test fixture used at 12-13 GHz.

was derived using [22]:

$$W = \frac{c}{2f_r}\left(\frac{\epsilon_{reff}+1}{2}\right)^{-1/2} \tag{4.1}$$

$$L = \frac{c}{2f_r\sqrt{\epsilon_e}} - \Delta l \tag{4.2}$$

$$\epsilon_e = \frac{\epsilon_{reff}+1}{2} + \frac{\epsilon_{reff}-1}{2}\left[1+\frac{12h}{W}\right]^{1/2} \tag{4.3}$$

$$\Delta l = 0.412h\frac{(\epsilon_e+0.3)(W/h+0.264)}{(\epsilon_e-0.258)(W/h+0.8)} \tag{4.4}$$

The deduced dielectric constant ϵ_{reff} was compared with the value of ϵ_{reff} obtained using a 100 MHz capacitance measurement between the two metal layers (the microstrip antenna and the ground plane):

$$C = \frac{\epsilon_0\epsilon_{reff}LW}{h} \tag{4.5}$$

where C is the measured capacitance. In all cases, the feed line was a 50 Ω microstrip line on the same $\epsilon_r = 10.5$ substrate. Both methods resulted in very similar effective dielectric constant ϵ_{reff} which is proportional to the volume of substrate removed underneath the microstrip antenna. These results are summarized in Table 4.1. The resonance method is accurate for low frequencies and depends on a good reference-plane calibration, which can become a limiting factor at high frequencies.

4.3 Radiation Efficiency Measurements

4.3.1 Description of Method

The radiometric technique is an accurate method to measure radiation efficiencies of planar antennas [47]. The antenna is connected to a calibrated low-noise RF

system of measured gain G_S and measured noise temperature T_S. The system parameters are determined using a standard coaxial hot/cold load measurement method. The gain G'_S and temperature T'_S of the RF system with the microstrip antenna are measured using a hot/cold load (hemispherical black body absorber Ecosorb) placed in front of the antenna to cover all its radiation pattern. The gain, G'_S, and temperature, T'_S, are calculated using:

$$G'_S = \frac{P_H - P_C}{KB(T_H - T_C)} \tag{4.6}$$

$$T'_S = \frac{T_H - YT_C}{1 - Y} \tag{4.7}$$

$$Y = \frac{P_H}{P_C} \tag{4.8}$$

where $T_H = 295$ K and $T_C = 85$ K. P_H and P_C are the measured RF powers with the hot ant cold load, respectively. B is the final resolution bandwidth of the RF system and K the Boltzman constant. The antenna loss is then:

$$G_{A,dB} = G'_{S,dB} - G_{S,dB} \tag{4.9}$$

which is a negative number. Since the antenna is viewed as a room temperature attenuator, the antenna loss can also be deduced from the rise of the system noise temperature and is:

$$P_{H,C} = G_S G_A kB(T_{H,C} + T_A) + G_S kBT_S \tag{4.10}$$

where G_A, T_A are the gain and noise temperature of the antenna. The hot/cold load measurement is referenced to the RF antenna connector (Fig. 4.2). This includes the loss of the coaxial connector, the feed line ohmic and radiation losses (including the

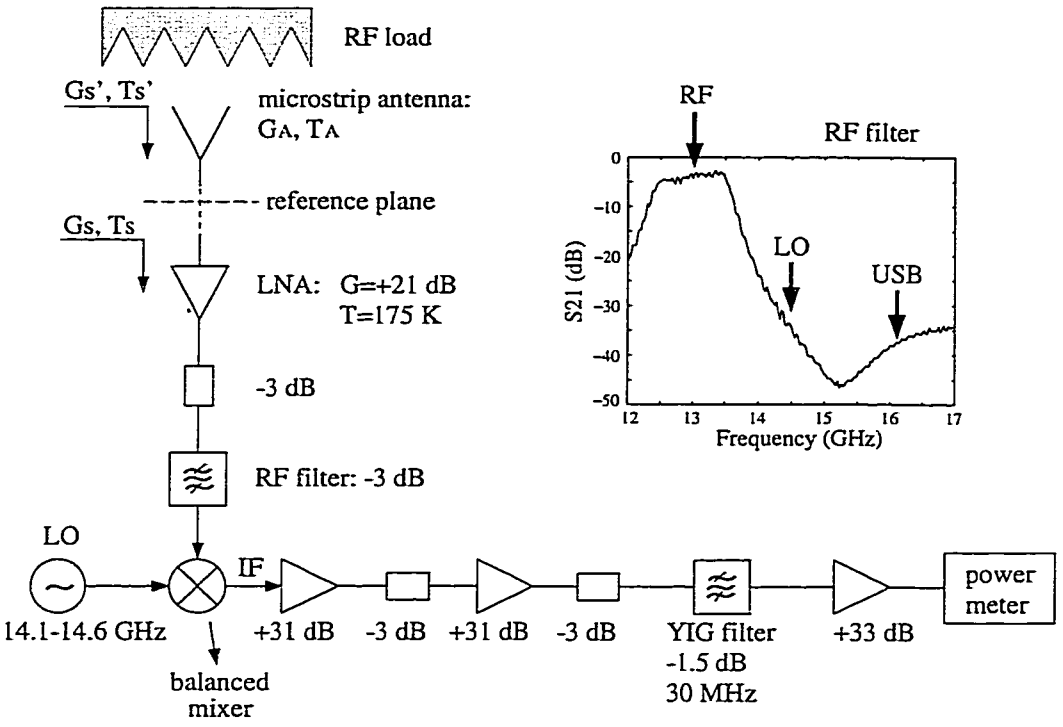

Figure 4.3: The RF chain at 12.5-13.5 GHz.

matching network), the impedance mismatch loss to 50 Ω, the microstrip antenna cavity losses (dielectric and ohmic) and the loss due to substrate modes excited by the feed line and the microstrip antenna.

4.3.2 RF Chain Design and Calibration

A detailed view of the RF chain is shown in Figure 4.3. The low-noise amplifier gain is 21 dB and is well matched to 50 Ω between 12 and 13.5 GHz. The RF bandpass filter has a 3 dB 12.5-13.5 GHz passband insertion loss. The intermediate frequency (IF) is fixed at 1.5 GHz. Since the LO is at 14.1-14.6 GHz, the lower sideband (12.6-13.1 GHz) is attenuated by 3 dB and the upper sideband is rejected by more than 40 dB (Fig. 4.3). This results in a true single side band (SSB) measurement. The conversion loss of the mixer is around 6 dB over the 12.6-13.1 bandwidth. The intermediate frequency is chosen to be 1.5 GHz, and is fixed by the YIG filter. The

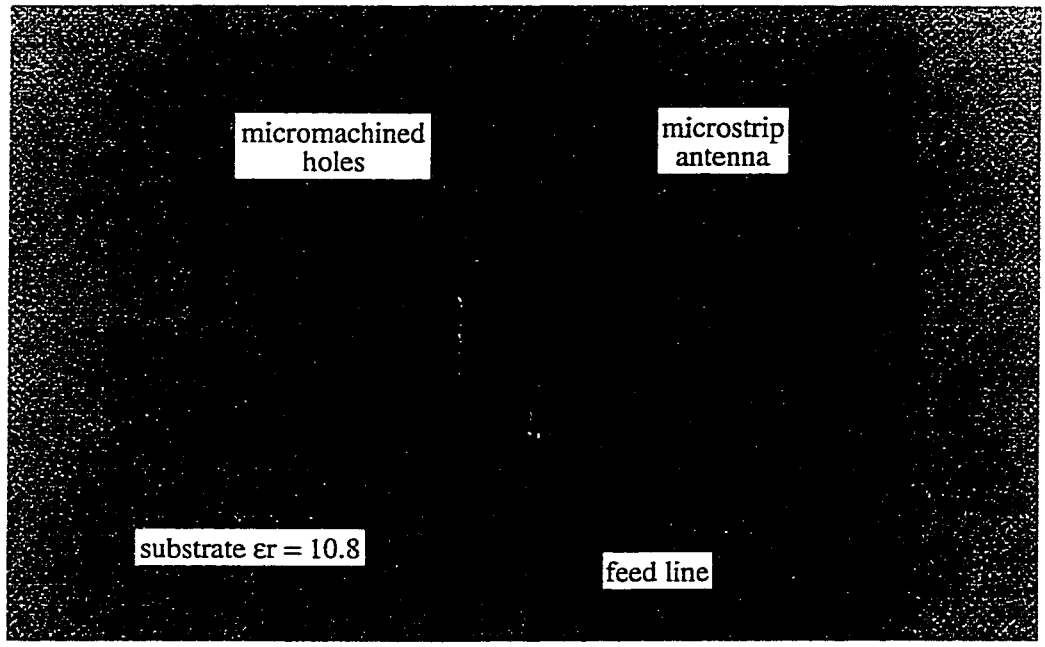

Figure 4.4: Fabricated microstrip antenna (0.70×0.92 cm) on a Duroid substrate, ϵ_r = 10.8, h=0.635 mm. The antenna is on localized low-ϵ_r dielectric ($\epsilon_r = 2.3$).

final resolution bandwidth of the IF chain is 30 MHz. A typical calibrated RF system has a gain G_S of 92±0.1 dB and a noise temperature T_S of 250±3 K. The power is averaged over this bandwidth and so is the efficiency and the impedance mismatch. However, 30 MHz is well within the bandwidth of the microstrip antenna and the averaging error is minimal.

4.3.3 Measurement Procedure

A 12.5-13.5 GHz microstrip antenna has been fabricated on ϵ_r = 10.8, h=0.635 mm (25 mils) Duroid substrate. The hole design was hexagonal for compact packing, with a hole diameter of 0.6 mm and a hole center to center spacing of 0.7 mm on a triangular lattice. A large volume (around 80%) of the material was removed and the resulting ϵ_{eff} using the quasi-static capacitance measurement described above was

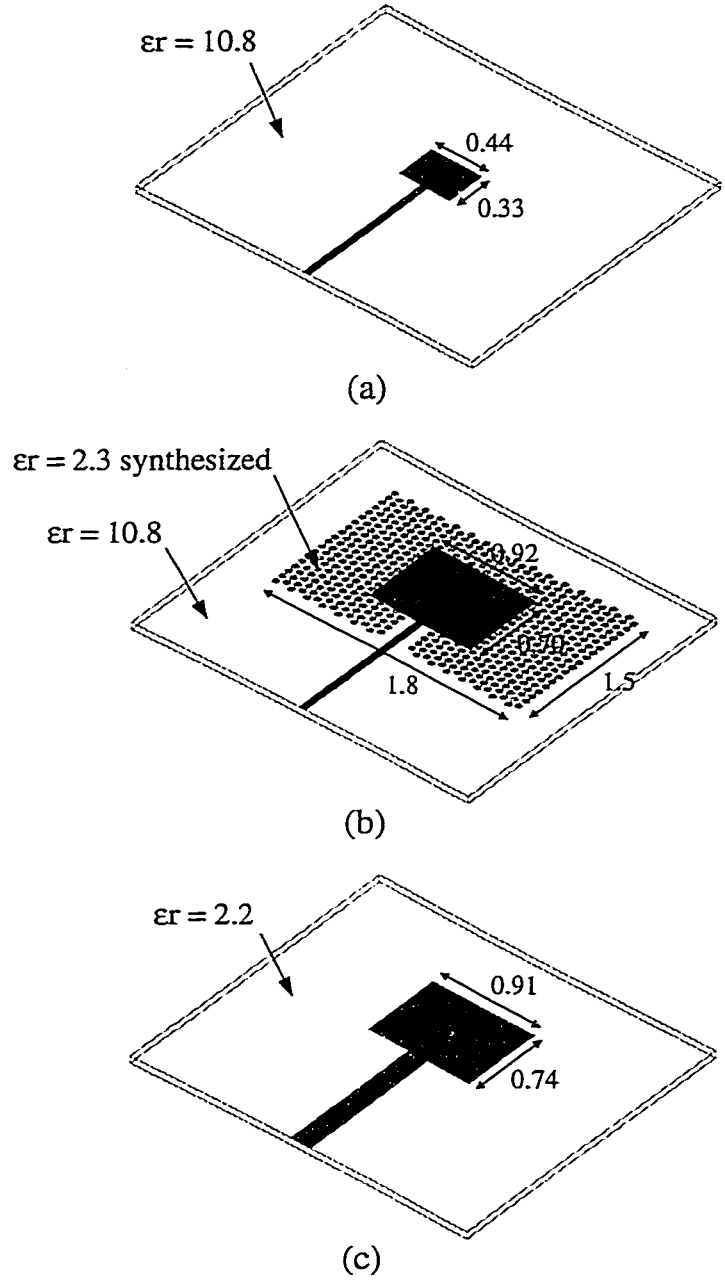

Figure 4.5: Comparision of the three antennas studied: $\epsilon_r = 10.8$ antenna (a), $\epsilon_r = 2.3$ synthesized antenna (b) and $\epsilon_r = 2.2$ antenna (c). The dimensions are in centimeters on the same scale.

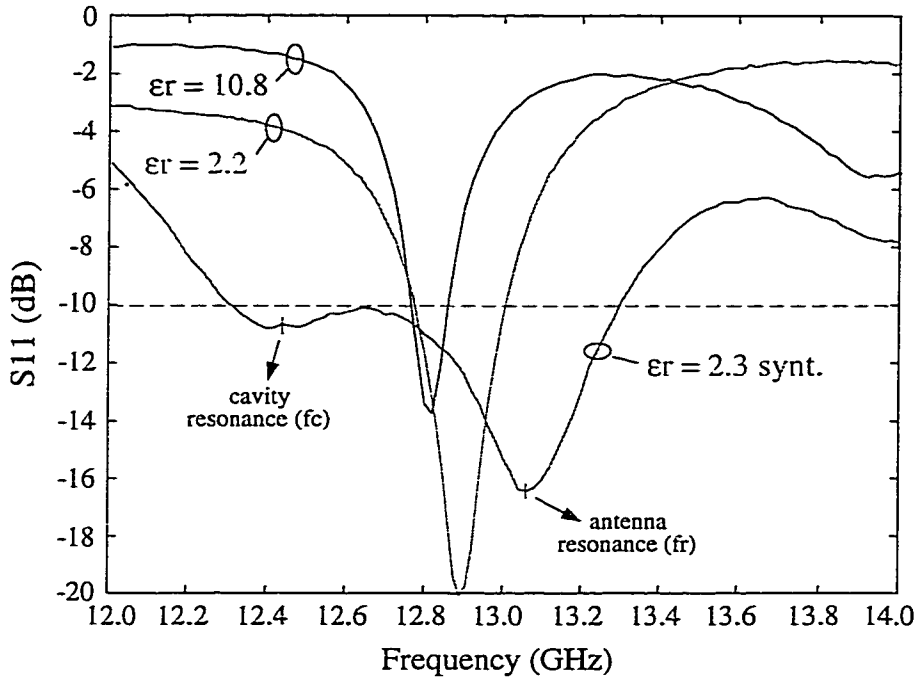

Figure 4.6: Measured input impedances of microstrip antennas on $\epsilon_r = 2.2$, synthesized $\epsilon_r = 2.3$ and $\epsilon_r = 10.8$.

$\epsilon_{reff} = 2.3$. Therefore, an antenna dimension of 0.70×0.92 cm is chosen for 12.8 GHz resonance. The holes were machined with a numerically controlled milling machine (Fig. 4.4).

In order to compare the performance of this antenna, we have fabricated other microstrip antennas on $\epsilon_r = 2.2$, h=0.635 mm ($\lambda_d/25$) with dimensions of 0.74×0.91 cm and on $\epsilon_r = 10.8$, h=0.635 mm ($\lambda_d/11$) with dimensions of 0.33×0.44 cm. All antennas were designed to resonate around 12.8-13.0 GHz and were matched to approximately 50 Ω using an in-line $\lambda/4$ transformer. All antennas were etched on a 7×7 cm dielectric substrate ($3.0\lambda_0$-square) and placed on top of a 10×10 cm ground plane ($4.3\lambda_0$-square), as in Figure 4.2. It is seen that while the synthesized dielectric microstrip antenna lies on a low-ϵ_{reff} substrate, the feed line still lies on a high-ϵ_r substrate. This is shown in Figure 4.5: the 50 Ω feed line has the same width for

the antennas on $\epsilon_r = 10.8$ and synthesized $\epsilon_r = 2.3$ and is wider for the $\epsilon_r = 2.2$ antenna. On the other hand, the microstrip patch has the same size on $\epsilon_r = 2.2$ and on synthesized $\epsilon_r = 2.3$, but is smaller on $\epsilon_r = 10.8$. The efficiency of a pyramidal horn antenna was first measured in the Ku band to validate the experimental set-up. The expected radiation efficiency for such a horn is very high (around 98%), since it has minimal ohmic losses and it is well matched to 50 Ω. The efficiency measured for the pyramidal horn antenna is 98$\pm$3% and agrees very well with the expected efficiency.

The calculated resonant impedances for the antenna on $\epsilon_r = 2.2$ and $\epsilon_r = 10.8$ are Z_r=185 Ω and Z_r=390 Ω, respectively [48]. All antennas are simply matched to 50 Ω using in-line $\lambda/4$ transformers. The measured input impedance of all three antennas is shown in Figure 4.6. It is seen that the antenna on the synthesized dielectric of $\epsilon_r = 2.3$ has a very wide -10 dB bandwidth of 7.9% due to the matching network. The antenna on $\epsilon_r = 2.2$ shows a -10 dB bandwidth of 1.8% which is, as expected, wider than the 0.8% -10 dB bandwidth of the $\epsilon_r = 10.8$ antenna. Microstrip feed lines are responsible for these small bandwidths and wider bandwidths can be achieved for all three designs by using feeding networks relying on slot-coupling [49]. This is demonstrated in Chapter 5 and 10% -10 dB bandwidths are measured at 94 GHz. One interesting fact is that the wide -10 dB bandwidth of 7.9% obtained for the synthesized dielectric $\epsilon_r = 2.3$ antenna results from a double resonance effect created by the presence of a low-ϵ_r micromachined cavity inside the high-ϵ_r substrate. The frequency of resonance of the cavity f_c=12.5 GHz is determined by the cavity length L_c (Fig. 4.5(b)), while the antenna resonance occurs at f_r=13.0 GHz (Fig. 4.6). Therefore, the microstrip antenna bandwidth can be tuned by changing the dimensions of the synthesized low-ϵ_r region around the antenna.

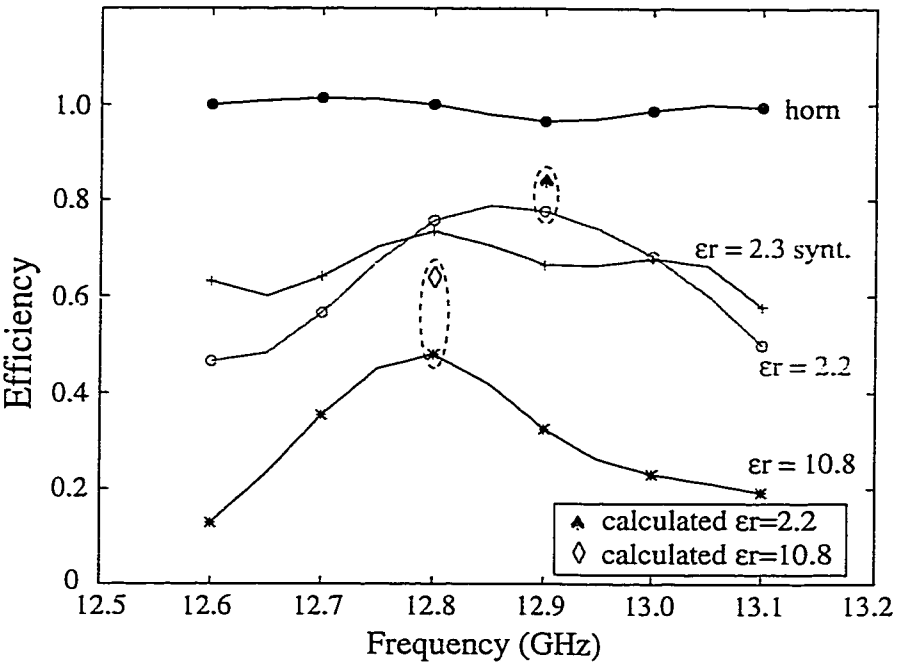

Figure 4.7: Measured radiation efficiencies of microstrip antennas on $\epsilon_r = 2.2$ (o), synthesized $\epsilon_r = 2.3$ (+), $\epsilon_r = 10.8$ (*), and horn antenna (•). Calculated values are ♠ for $\epsilon_r = 2.2$ and ◇ for $\epsilon_r = 10.8$.

Substrate ϵ_r	2.2	2.3 (synth.)	10.8
Resonance frequency	12.9	12.8	12.8
Measured efficiency	0.78±3%	0.70±3%	0.48±3%
Mismatch losses (dB)	0.05 (99%)	0.09 (98%)	0.18 (96%)
Connector loss (dB)	0.15 (97%)	0.15 (97%)	0.15 (97%)
Feed line loss (dB)	0.10 (97%)	0.70 (85%)	0.70 (85%)
Total loss (dB)	0.30 (93%)	0.94 (80%)	1.03 (79%)
Deduced efficiency	0.83	0.87	0.61
Calculated efficiency	0.86	0.86	0.67

Table 4.2: Measured and calculated radiation efficiencies at resonance for different substrates.

The efficiency of all three antennas was measured using the radiometric method described above. First, the efficiency of a pyramidal horn antenna was measured in the Ku band to validate the experimental set-up. The expected radiation efficiency for such a horn is very high (around 98%), since it has minimal ohmic losses and it is well matched to 50 Ω. The efficiency measured for the pyramidal horn antenna is 98±3% and agrees very well with the expected efficiency. It is seen in Figure 4.7 that the microstrip antenna radiation efficiency improved from 48±3% for $\epsilon_r = 10.8$ to 73±3% for $\epsilon_r = 2.3$ synthesized, and that the synthesized dielectric antenna yields similar values as the $\epsilon_r = 2.2$ antenna. In Figure 4.7, the results include feed line losses (ohmic, dielectric and radiation), substrate mode losses and mismatch loss to 50 Ω. The bell-shaped curves with a peak at 12.8-13.0 GHz are mainly due to mismatch loss and show the bandwidth of the microstrip antennas to a 50 Ω load.

Figure 4.7 also shows the calculated radiation efficiency at resonance for the $\epsilon_r = 2.2$ antenna at 12.9 GHz and the $\epsilon_r = 10.8$ antenna at 12.8 GHz. The values were determined using Prof. David Pozar's microstrip program (The Univ. of Massachussets, Amherst) and do not include connector loss, mismatch loss or feed line loss. However, they do include the microstrip antenna ohmic and dielectric cavity losses and the substrate mode losses. As can be seen, a very good agreement is achieved with the $\epsilon_r = 2.2$ measurement and the small difference (8%) is explained by connector and feed line losses (50 Ω microstrip line on $\epsilon_r = 2.2$, 0.635 mm thick substrate). For the case of the $\epsilon_r = 10.8$ antenna, there is a 19% difference between the calculated and measured values. It could be explained by the matching network loss, acting as a high-Q cavity, and the radiation loss of the feed line (50 Ω microstrip line on $\epsilon_r = 10.8$, h=0.635 mm thick, or $\lambda_d/11$, substrate). By modeling this feed line with HP Momentum [31], the loss was estimated at 0.20±0.05 dB/cm at 12.8-

13.0 GHz. The line is 3.3 cm long and results in an feed line loss of around 0.7 dB. Taking this loss and the connector loss (0.1-0.2 dB) into account, the measured value becomes 61% which agrees well with the calculated radiation efficiency (67%). The difference can be partially attributed to the high-Q matching network.

It is important to note that the synthesized $\epsilon_r = 2.3$ antenna feed line is on a $\epsilon_r = 10.8$ substrate (the holes are localized around the antenna only). If the feed line loss is deimbedded from the measured value of 73±3%, a very good agreement with the calculated value is obtained: a radiation efficiency of 87%, the same as the $\epsilon_r = 2.2$ antenna (Table 4.2).

4.3.4 Radiation Efficiency Prediction: the Quality Factor Approach

The radiation efficiency of an antenna is defined as the ratio of the power radiated to the total power at the antenna ports. For microstrip antennas, the radiation efficiency suffers from conductor losses, dielectric losses and losses due to surface waves. The quality factor approach is interesting and simple to understand, and can evaluate the loss mechanism of microstrip antennas. The idea is to consider the microstrip antenna as a microstrip resonator, and then to determine the quality factor of all loss contributions: Q_c for conductor losses, Q_d for dielectric losses, Q_s for surface wave losses. Q_r is the radiation quality factor and determines the power radiated by the antenna. The quality factor is defined as:

$$Q = 2\pi f_0 \frac{W_T}{P}$$

where f_0 is the frequency of resonance, W_T the total energy stored in the resonator and P the power lost. The quality factor can also be written as:

$$Q = \frac{\pi}{\alpha\lambda}$$

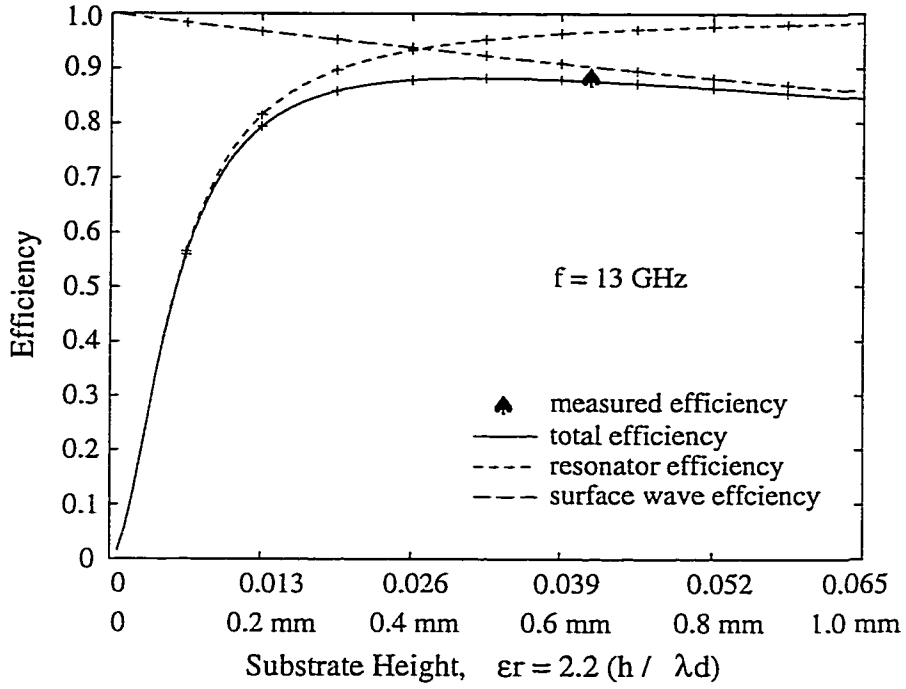

(a)

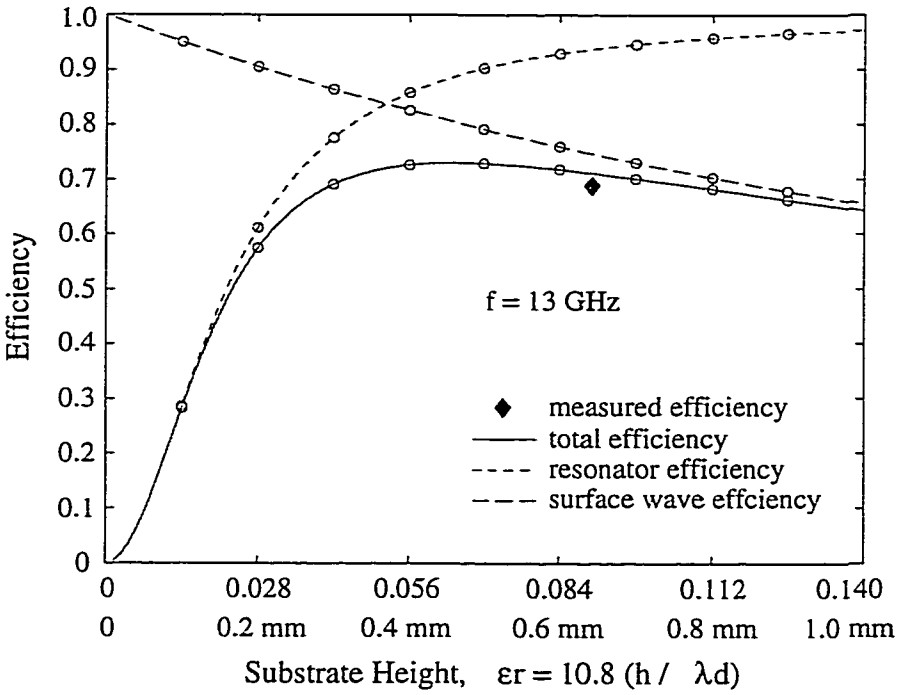

(b)

Figure 4.8: Predicted radiation efficiency of microstrip antennas on $\epsilon_r = 2.2$ (a) and $\epsilon_r = 10.8$ (b) substrates versus substrate thickness.

where α is the attenuation and λ the wavelength.

Once the antenna dimensions are calculated at resonance using the equations from Section 4.2, the dielectric and conductor quality factor are deduced from [50]:

$$Q_d = \frac{\pi}{\alpha_d \lambda_d}$$

$$Q_c = \frac{\pi}{\alpha_c \lambda_g}$$

where α_d and α_c are the dielectric and conductor attenuations, respectively, with:

$$\alpha_d = \frac{k_0 tan\delta}{2\sqrt{\epsilon_r}} q$$

$$\alpha_c = \frac{R_s}{Z_0 W}$$

q is the filling factor corresponding to the percentage of electric field inside the substrate, $k_0 = 2\pi/la_0$, Z_0 is the characteristic impedance, W the antenna width, $tan\delta$ the dielectric loss tangent, and R_s the surface resistance for a metal of conductivity σ:

$$q = \frac{\epsilon_r(\epsilon_e - 1)}{\epsilon_e(\epsilon_r - 1)}$$

$$R_s = \sqrt{\frac{\pi f \mu_0}{\sigma}}$$

It is useful to define a circuit quality factor Q_0 as:

$$\frac{1}{Q_0} = \frac{1}{Q_c} + \frac{1}{Q_d}$$

The radiated power P_r and power lost to surface waves P_s for a dipole antenna on a grounded dielectric substrate of height h are calculated using simple approximate formulas derived by Jackson *et al.* [51]:

$$P_r = (k_0 h)^2 \frac{80\pi^2(1 - 1/\epsilon_r + 2/5\epsilon_r^2)}{\lambda_0^2}$$

$$P_s = (k_0 h)^3 \frac{60\pi^3(1-1/\epsilon_r)^3}{\lambda_0^2}$$

The radiation quality factor is given by Lewin's formula [52], resulting in the quality factors [50]:

$$Q_r = \frac{Z_0}{480\pi(h/\lambda_0)^2 F(\epsilon_e)}$$

$$Q_s = Q_r \frac{P_r}{P_s}$$

with

$$F(\epsilon_e) = \frac{\epsilon_e + 1}{\epsilon_e} - \frac{(\epsilon_e - 1)^2}{2\epsilon_e\sqrt{\epsilon_e}} ln \frac{\sqrt{\epsilon_e}+1}{\sqrt{\epsilon_e}-1}$$

The total power lost inside the microstrip resonator is then:

$$P_T = P_c + P_d + P_r + P_s = 2\pi f_0 W_T (\frac{1}{Q_0} + \frac{1}{Q_r} + \frac{1}{Q_s})$$

resulting in the radiation efficiency:

$$\eta = \frac{P_r}{P_T} = \frac{\frac{1}{Q_r}}{\frac{1}{Q_0} + \frac{1}{Q_r} + \frac{1}{Q_s}}$$

$$\eta = \frac{Q_0 Q_s}{Q_r Q_s + Q_0 Q_r + Q_0 Q_s}$$

The method described above is applied to microstrip antennas on $\epsilon_r = 2.2$ and $\epsilon_r = 10.8$ substrates at 13 GHz. Figure 4.8(a) and 4.8(b) shows the calculated radiation efficiency versus substrate thickness for both antennas. It can be clearly seen that for $\epsilon_r = 2.2$ and $\epsilon_r = 10.8$ antennas, the maximum radiation efficiency is a broad function of the substrate thickness and is quite high between $\lambda_d/20$- to $\lambda_d/10$-, and $\lambda_d/40$- to $\lambda_d/20$- thick substrates, respectively. The corresponding radiation efficiency is 86% for the antenna on $\epsilon_r = 2.2$ substrates and 71% for the antenna on $\epsilon_r = 10.8$ substrates at 13 GHz.

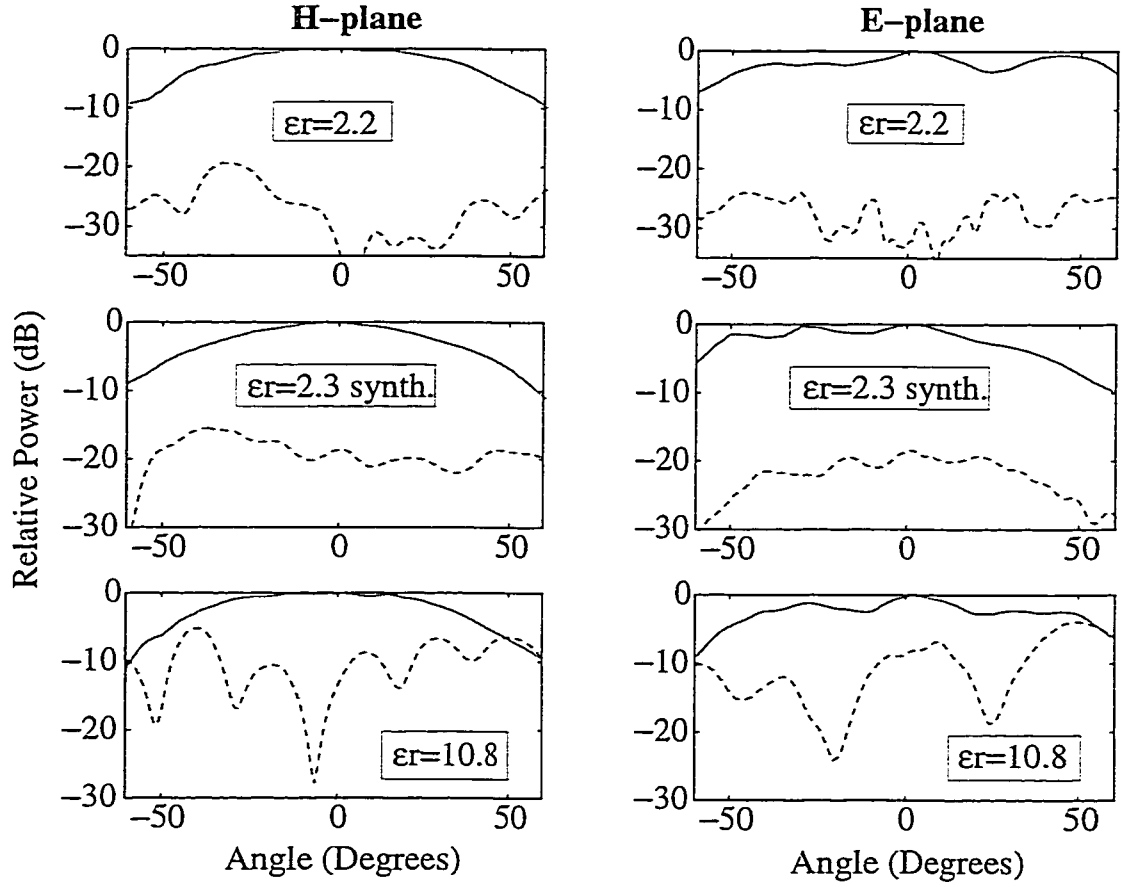

Figure 4.9: Radiation patterns of microstrip antennas on $\epsilon_r = 2.2$ at 12.9 GHz, synthesized $\epsilon_r = 2.3$ at 12.8 GHz, and $\epsilon_r = 10.8$ at 12.8 GHz. E-plane, H-plane (-) and cross-polarization patterns (- -) are shown.

4.4 Radiation Patterns

The measured patterns of all three antennas at their respective resonant frequencies are shown in Figure 4.9. Note that the antennas are all on a 10-cm square holder and suffer from finite ground plane edge effects (Fig. 4.2). It is seen that the $\epsilon_r = 10.8$ antenna on a 0.635 mm thick substrate ($\lambda_d/11$) suffers from a large ripple and high cross-polarization levels on broadside due to substrate modes and edge radiation in the E-plane. The synthesized dielectric antenna ($\epsilon_r = 2.3$) shows a small ripple mainly due to radiation from the feed lines but the cross-polarization levels are quite low. As expected, the $\epsilon_r = 2.2$ antenna exhibits good radiation patterns and low cross-polarization levels.

4.5 Conclusion

A clear improvement of the radiation efficiency (from 61% to 87%) and radiation patterns of microstrip antennas on high dielectric constant substrates has been demonstrated, resulting from a local reduction of the substrate dielectric constant underneath and around the antenna. The drilled region creates a low-ϵ_r cavity in a high-ϵ_r substrate. The -10 dB bandwidth has also been increased (from 0.8% to 7.9%) from a double resonance effect. The cavity dimensions can be tuned so that the cavity resonance overlaps the antenna resonance, therefore significantly improving the system bandwidth. A thorough theoretical and experimental analysis is needed in order to characterize qualitatively and quantitatively the effect of this double resonance. High-efficiency micromachined antennas can be designed at 10-30 GHz on high resistivity Silicon and GaAs substrates with this method.

CHAPTER V

A 94 GHz APERTURE-COUPLED MICROMACHINED MICROSTRIP ANTENNA

In Chapter 4, the losses suffered from surface waves by microstrip antennas on high-ϵ_r substrates were suppressed by synthesizing a local low-ϵ_r region around the antenna by drilling closely spaced holes [53]. The antenna was simply fed by a microstrip line. In array applications, the aperture-coupled microstrip antenna [54, 55] is preferable since it allows for the electromagnetic separation of the radiating element (the microstrip patch) and the feed network with the use of the ground plane.

The synthesis of low-ϵ_r substrates and local regions can also be achieved artificially using micromachining processes developped for MEMS, and particularly wet etching of silicon with KOH or TMAH. An simple approach is to etch a cavity directly beneath the microstrip antenna [56]. This chapter investigates a millimeter-wave aperture-coupled micromachined microstrip antenna, operating at 94 GHz. The design consists of two stacked silicon substrates: 1) the bottom substrate, which carries the microstrip antenna, is micromachined to improve the radiation performance of the antenna, and 2) the top substrate, which carries the microstrip feed line and the coupling slot. Also, a low-loss transition from microstrip to coplanar waveguide

(cpw) transmission-line must be designed so as to integrate the microstrip antenna in a configuration where the feed network is cpw-based.

5.1 Antenna Design

Figure 5.1 shows the perspective view and the cross-section of the aperture-coupled micromachined microstrip antenna. The design of the antenna is described below, referring to Figure 5.2:

5.1.1 Antenna

A cavity is etched in the substrate below the microstrip antenna. The synthesized effective dielectric constant (ϵ_{eff}) is characterized to determine the antenna dimensions (W, L) for a resonance at 94 GHz. The effective dielectric constant is the quasi-static value seen underneath the microstrip patch antenna and is in the range of 2.8-3.9, depending on the etching depth. The effective dielectric constant is deduced from the quasi-static calculation of the microstrip patch capacitance on a cavity-etched silicon substrate. The calculations are made with Quickfield [57] and are based on a Finite Element resolution of Poisson's equation inside the structure. Figure 5.3 shows the calculated effective dielectric constant versus the silicon-to-air fraction. The cavity walls are not taken into account. The effective dielectric constant is calculated from:

$$\epsilon_{eff} = C_{cav}/C_{air}$$

where C_{cav} and C_{air} are the capacitance with the silicon and with air only, respectively. In practice for silicon substrates, a dielectric constant of 3.0-3.5 is achieved when the cavity depth reaches 75% of the substrate thickness. The antenna is then analyzed using the effective dielectric constant obtained. There are no models de-

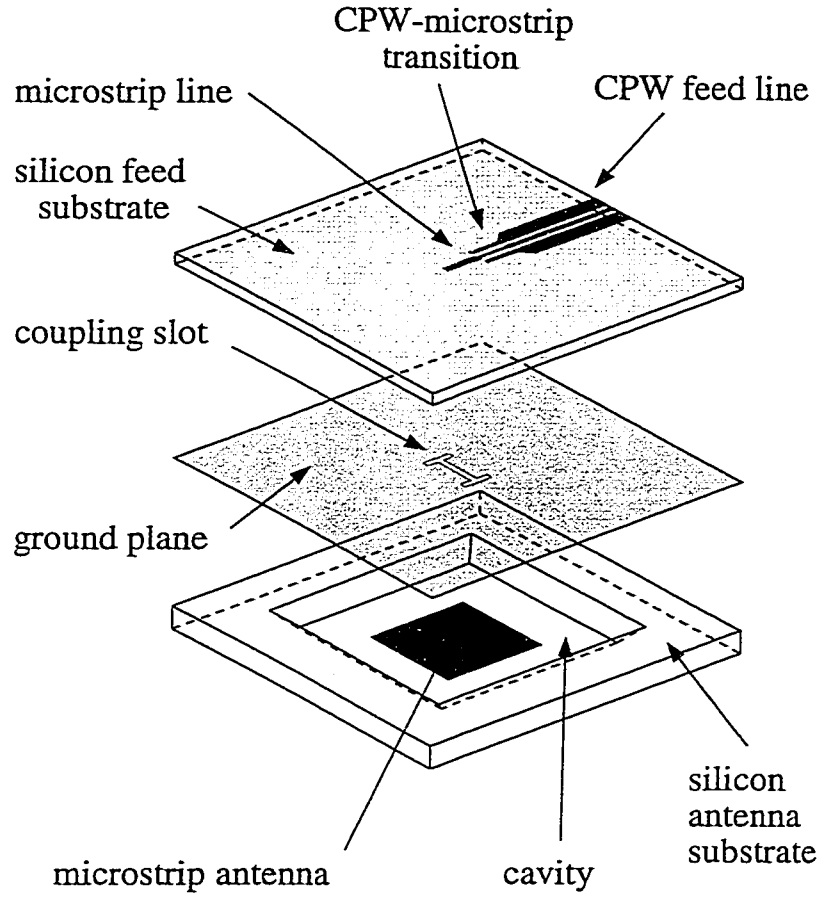

(a)

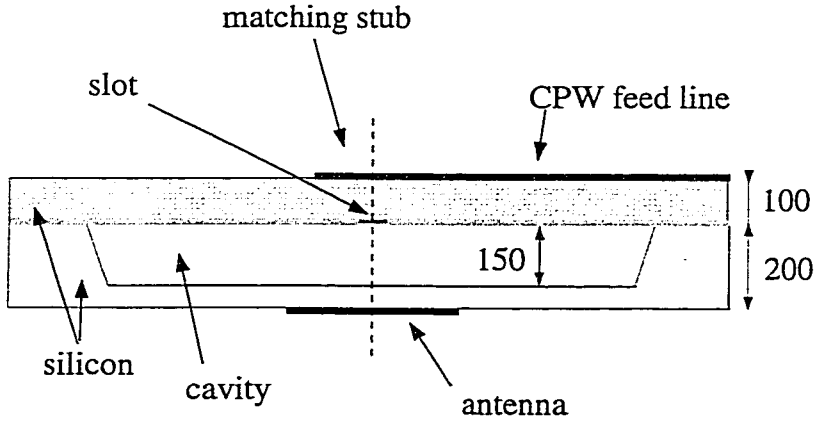

(b)

Figure 5.1: Perspective view (a) and cross-section (b) of the aperture-coupled micromachined microstrip antenna. All dimensions are in microns.

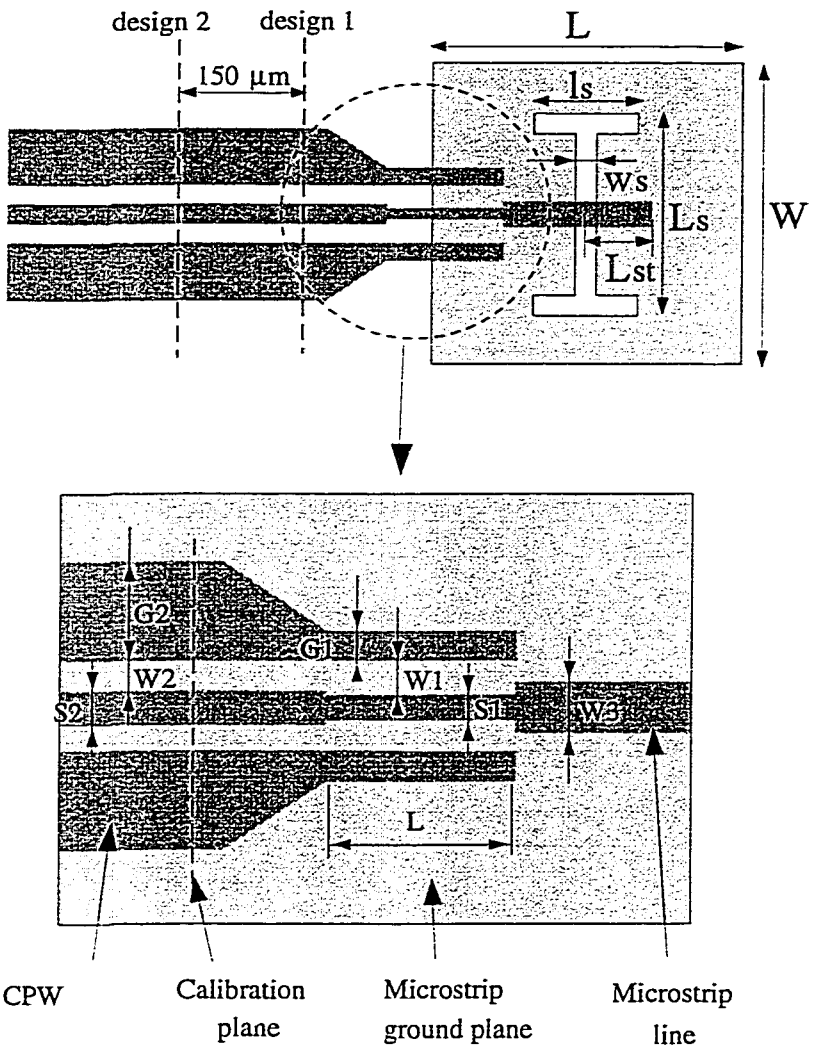

Figure 5.2: Top view of the microstrip antenna design and of the cpw-to-microstrip transition.

scribing the effect of the cavity width and this will be the subject of a further study. It is believed that the cavity around the antenna can be designed to resonate close to the microstrip antenna resonance, and therefore resulting in an increase in bandwidth, as described in Chapter 4 [53].

The influence of the shape of the slot has been studied previously by Pozar and Rathi [49, 58]. A H-shaped slot (Fig. 5.2) is used which improves the coupling compared to a rectangular slot. The H-slot design results in a short slot and pushes

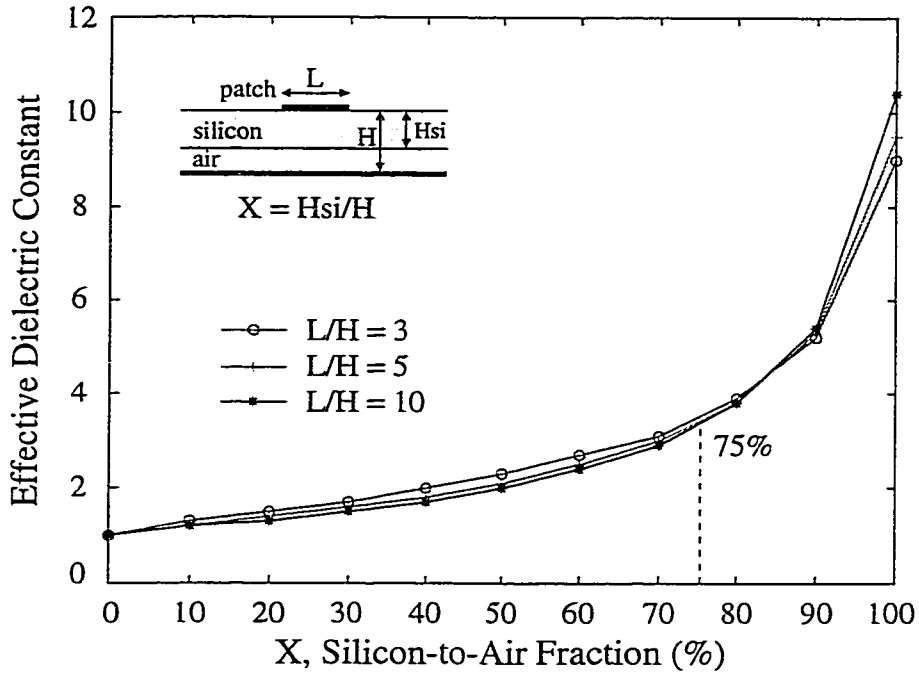

Figure 5.3: Effective dielectric constant as a function of the silicon removed under a square patch on silicon, for various L/H ratios, where L is the patch width and H the substrate thickness.

the resonant frequency of the slot above that of the microstrip antenna, thereby improving the front-to-back ratio. The real part of the aperture-coupled microstrip antenna input impedance is fixed by the length of the slot, L_s, and is designed to be 50 Ω. The imaginary part of the aperture-fed microstrip antenna input impedance is then compensated by the microstrip line extension, L_{st}, which acts like a matching stub (Fig. 5.2). The simulation is done using a commercial analysis program IE3D (Zeeland Software [59]).

5.1.2 CPW to Microstrip Line Transition

In order to integrate the microstrip antenna in an array where the feed network is based on cpw lines, a simple, low-loss and compact cpw to microstrip transition is designed, extending the work of Houdard *et al.* [60] at W-band frequencies. It can be analyzed as a three-line microstrip coupler, and more details can be found in Chap-

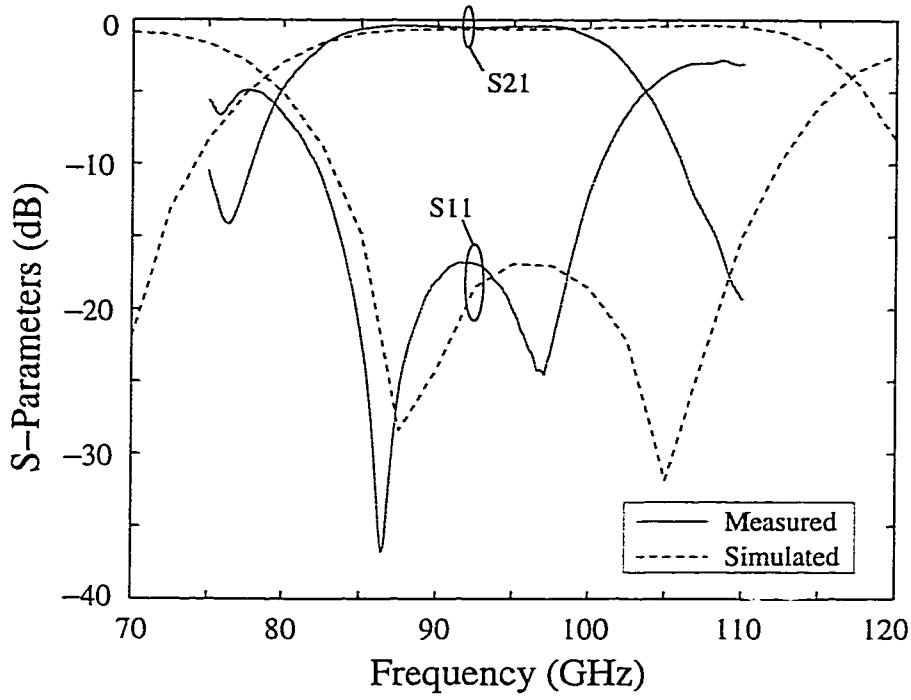

Figure 5.4: Comparison between measured and simulated (IE3D) S-parameters of the cpw-to-microstrip transition.

ter 6 and in [61]. Figure 5.2 shows the layout and, Figure 5.4 shows the measured and simulated performance of the transition used at W-band frequencies. The fgc feed line dimensions are S_2=40 μm, W_2=24 μm and G_2=106 μm corresponding to a chatacteristic impedance of 50 Ω. The microstrip line is W_3=74 μm wide resulting in a 50 Ω characteristic impedance. The dimensions of the cpw-to-microstrip transition are S_1=30 μm, W_1=29 μm and G_1=45 μm. The coupling region is chosen to be L=280 μm long ($\lambda_g/4$ at 94 GHz). A back-to-back transition separated by a 860 μm long microstrip line results in 0.2 dB insertion loss per transition with a bandwidth of 20%. The return loss is better than -17 dB from 85 to 100 GHz. The shift in frequency observed for this transition between measurements and simulations is due to the existence of unwanted microstrip modes below all three strips forming the fgc line, and particularly below the two outer ground strips, as described in Section 5.2.

Measurements and simulations disagree above 100 GHz, where the microstrip substrate becomes $\geq \lambda_d/10$ and the surface-wave modes in the microstrip line become the dominant loss factor.

5.2 Input Impedance

Two aperture-coupled microstrip antennas are designed for 94 GHz operation. One is built on a full 100 μm thick silicon wafer and the other on a 200 μm thick silicon wafer in which a 150 μm deep cavity has been etched using TMAH or KOH wet etching techniques [62]. Referring to Figure 5.1 and 5.2, the antenna and slot dimensions are, respectively, $W \times L$=380 μm $\times$ 380 μm and $L_s \times l_s \times w_s$ =270 μm $\times$ 120 μm $\times$ 50 μm for the antenna integrated on a full silicon wafer of 100 μm thick, and $W \times L$=800 μm $\times$ 800 μm and $L_s \times l_s \times w_s$ =500 μm $\times$ 250 μm $\times$ 50 μm for the micromachined microstrip antenna. The bottom silicon substrate is identical for both designs and is 100 μm thick (feedline substrate). The microstrip feed line is W_3=74 μm wide resulting in a 50 Ω characteristic impedance, and the matching stub is L_{st}=250 μm long for the non-micromachined antenna and L_{st}=160 μm long for the micromachined one. The cpw feed line and the cpw-to-microstrip transition used for coplanar-probe on-wafer measurements are the same for the micromachined and the non-micromachined antennas. The dimensions of these are given in section 5.2. All metal layers are 8000 Åof evaporated gold, corresponding to around 3 skin depths at 94 GHz. Figure 5.5 shows the pictures of the antenna, cavity, slot and feed line for the aperture-coupled micromachined microstrip antenna.

The input impedance of the two antennas is measured using W-band picoprobes on a HP8510 network analyzer and TRL calibration is used to move the reference plane from the probe-tip to the plane shown in Figure 5.2. The simulated (IE3D)

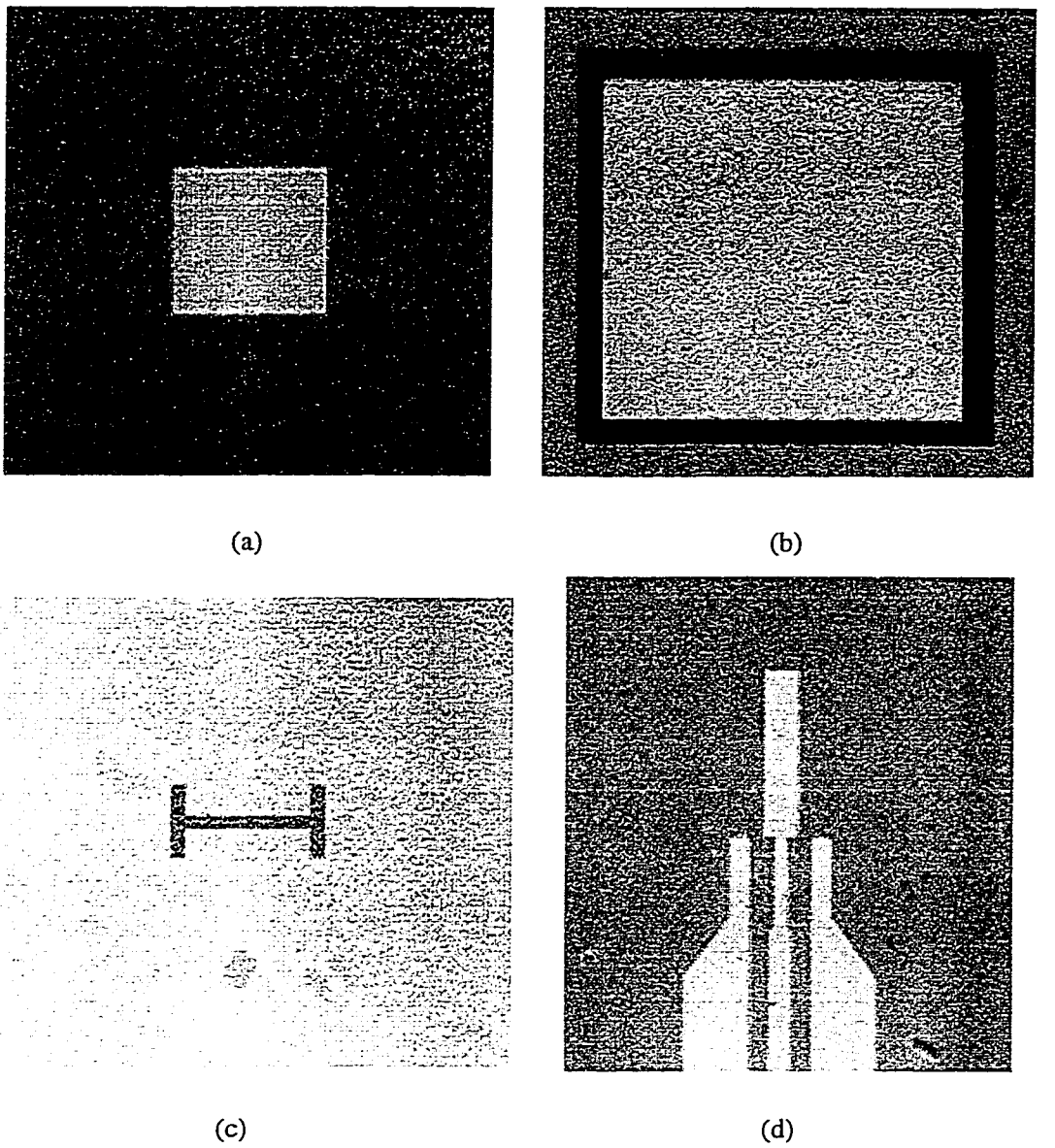

Figure 5.5: Pictures of the microstrip antenna (a), micromachined cavity (b), coupling-slot (c) and feed line (d). The four pictures are not at the same scale.

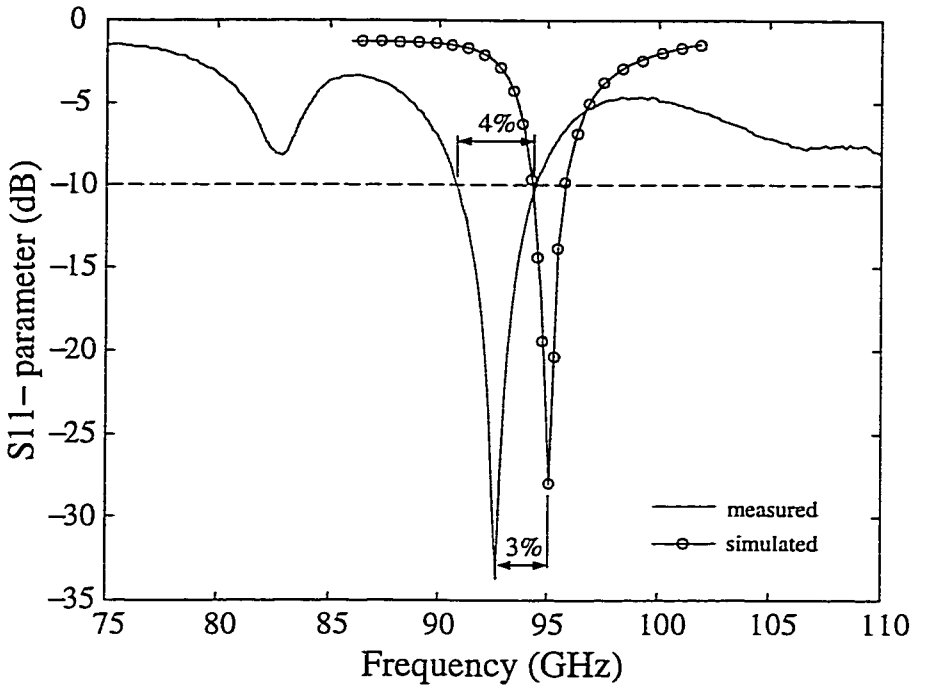

(a)

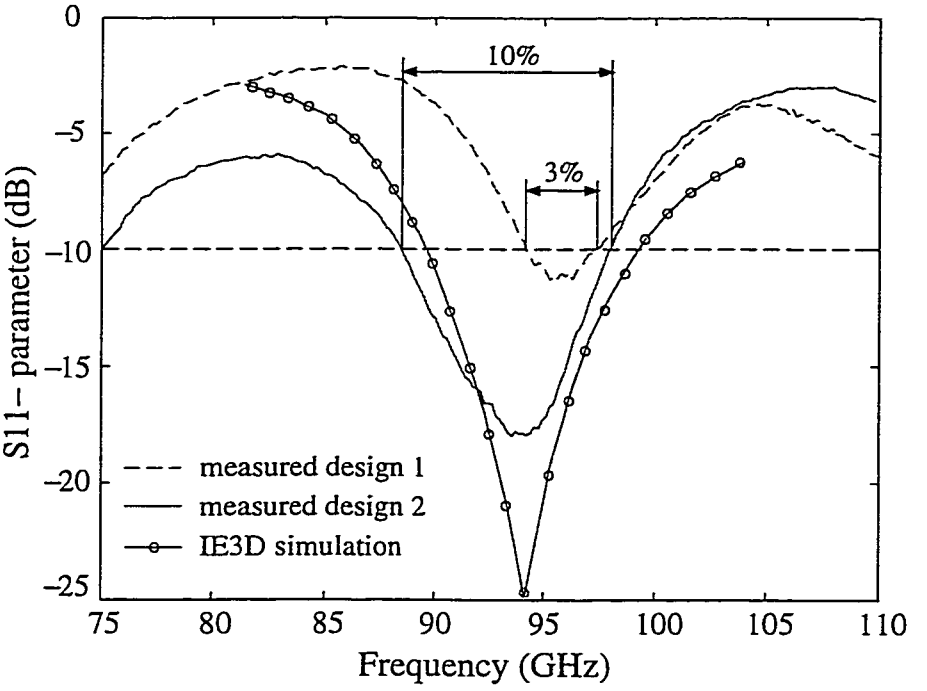

(b)

Figure 5.6: Measured and simulated (IE3D) input impedance of the microstrip antenna built on a full silicon substrate of 100 μm thick (a) and on a 200 μm thick silicon wafer in which a 150 μm deep cavity has been etched (b).

and measured input impedances of both microstrip antennas are shown in Figure 5.6. It is seen that there is a 3% frequency shift between the measured and simulated response for the standard microstrip antenna, which could be attributed to small variations in the silicon wafer thickness, and to the general inaccuracies of numerical packages in high-Q structures ($\epsilon_r = 11.7$) at millimeter-wave frequencies (probably due to the simulation at the exact current distribution in the slot-feed). A return loss of -35 dB at 92.5 GHz with a -10 dB bandwidth of 4% has been measured for the antenna built on a full silicon wafer of 100 μm thick. Also, a return loss of -12 dB at 95 GHz with a -10 dB bandwidth of 3%, and of -18 dB at 94 GHz with a -10 dB bandwidth of 10% has been obtained for the micromachined microstrip antenna, respectively, for Designs #1 and #2. Notice that in this case, the simulation agrees very well with the measurement due to the low-Q ($\epsilon_r = 2.9 - 3.0$) nature of the micromachined antenna.

The only difference between Designs #1 and #2 in Figure 5.6(b) is the length of the input cpw feed line which is around 150 μm. The important variation of the antenna return loss for the two different designs can be explained by the dependence of the cpw-to-microstrip transition versus the length of the cpw feed line. This dependence is attributed to a parasitic microstrip mode which is triggered by the transition discontinuity and propagates along the coplanar ground planes of the conductor-backed cpw feed line. These microstrip modes are easily triggered at the discontinuities (the open stubs) due to the high dielectric constant of silicon and the thickness of the wafer (100 μm or $\lambda_d/10$). The W-band probes only measure the cpw component of the signal, and the microstrip modes are therefore reflected at the probe pads and at the open stubs, resulting in a microstrip standing wave. A better measurement is therefore achieved by changing the length of the input cpw feed line

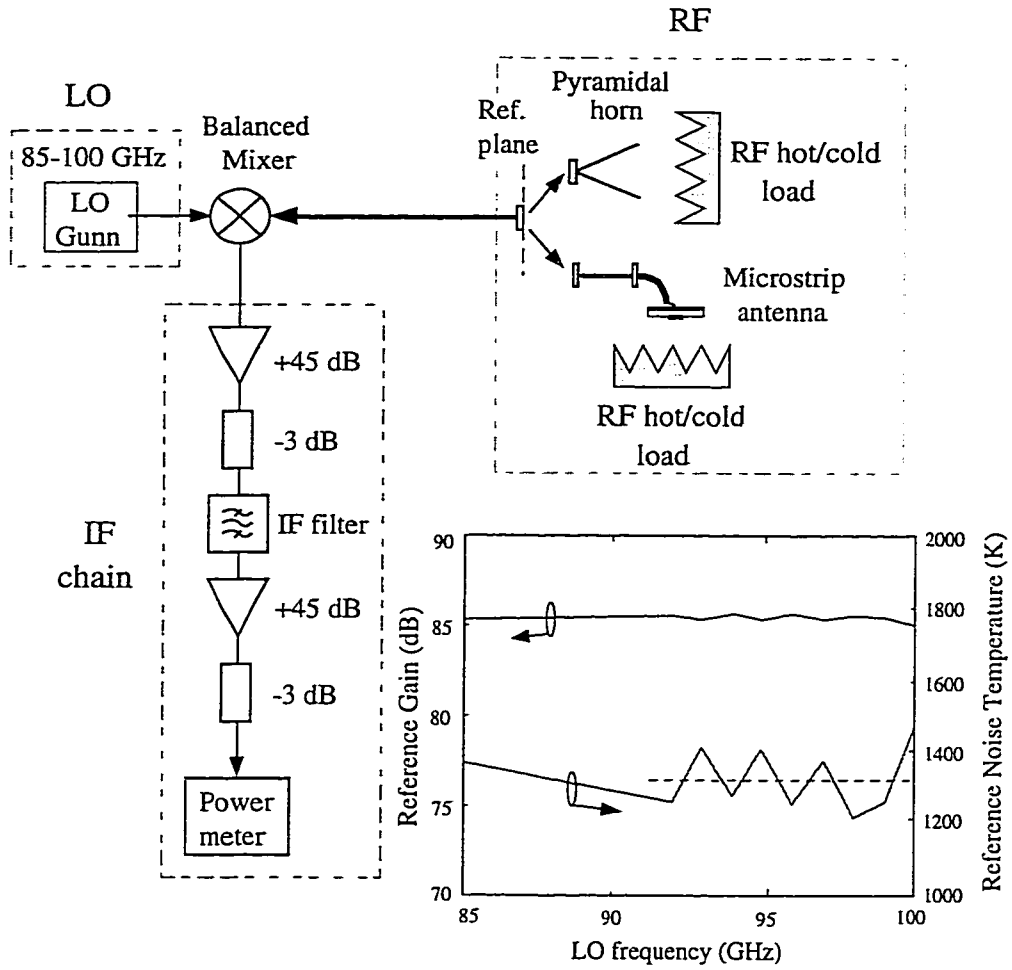

Figure 5.7: Radiometric measurement set-up at 85-100 GHz.

and setting the TRL calibration plane at a minimum of the standing wave, as is done in Design #2.

The conversion mode at discontinuities in conductor-backed cpw has been shown by Jackson in [63]. Various back-to-back cpw-to-microstrip transitions have been designed and measured to fully characterize the parasitic microstrip mode along the conductor-backed feed cpw line and to cancel it. The reader is referred to [64] for more detail.

5.3 Radiation Efficiency

The radiation efficiency is measured using the radiometric technique described in Chapter 4. The microstrip antenna is connected to a calibrated (low-noise) system of gain G_s and noise temperature T_s. The RF chain is calibrated using a standard WR-10 pyramidal horn which has a known radiation efficiency of 97-98%. The horn is then replaced by the microstrip antenna connected to the chain via a W-band picoprobe. This method is a DSB measurement since no RF filter is used to separate the upper sideband from the lower sideband before mixing down to the IF. The measurement is therefore more accurate if a small IF is chosen. For example, the DSB measured radiation efficiency at 94 GHz with a 200 MHz IF is the average of the radiation efficiencies at 93.8 GHz and 94.2 GHz, while it is the average of the radiation efficiencies at 92.6 GHz and 95.4 GHz if an 1.4 GHz IF is chosen.

A detailed view of the RF chain is shown in Figure 5.7. The conversion loss of the W-band balanced mixer is 8 dB over the 80-100 GHz bandwidth. The intermediate frequency (IF) is fixed at 200 MHz. The calibrated IF chain has a gain of 86 dB and a noise temperature of 111 K. The total system DSB noise temperature and gain are 1350±150 K and 86±0.5 dB, respectively (Fig. 5.7).

Figure 5.8 represents the measured radiation efficiency of different microstrip antennas using the radiometric method. The measured radiation efficiency improved from 28±5% for the 100 μm thick silicon substrate ($\epsilon_r = 11.7$) to 58±5% (Design #2) for the micromachined antenna with ϵ_{eff}=3.0. Notice that Design #1 resulted in 50% radiation efficiency due to some power loss in the cpw-to-microstrip transition (and mode conversion). The dashed curves in Figure 5.8 represent the measurement results including the microprobe losses (1.0 dB), the feedline losses (0.2 dB), and the mismatch loss to 50 Ω load. The straight lines represent the de-embedded radiation efficiency of microstrip antenna designs around their resonance frequency.

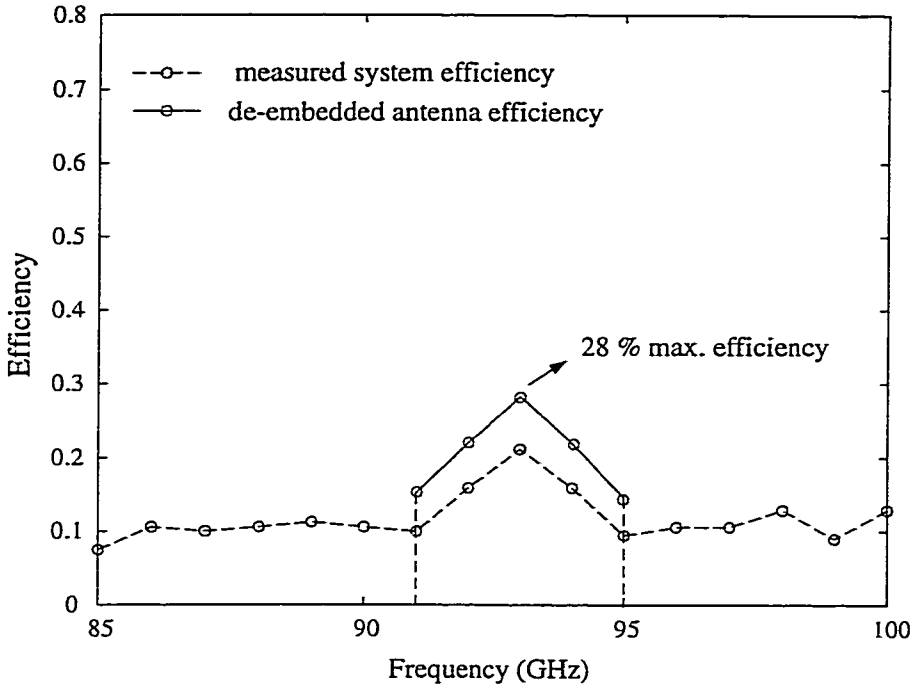

(a)

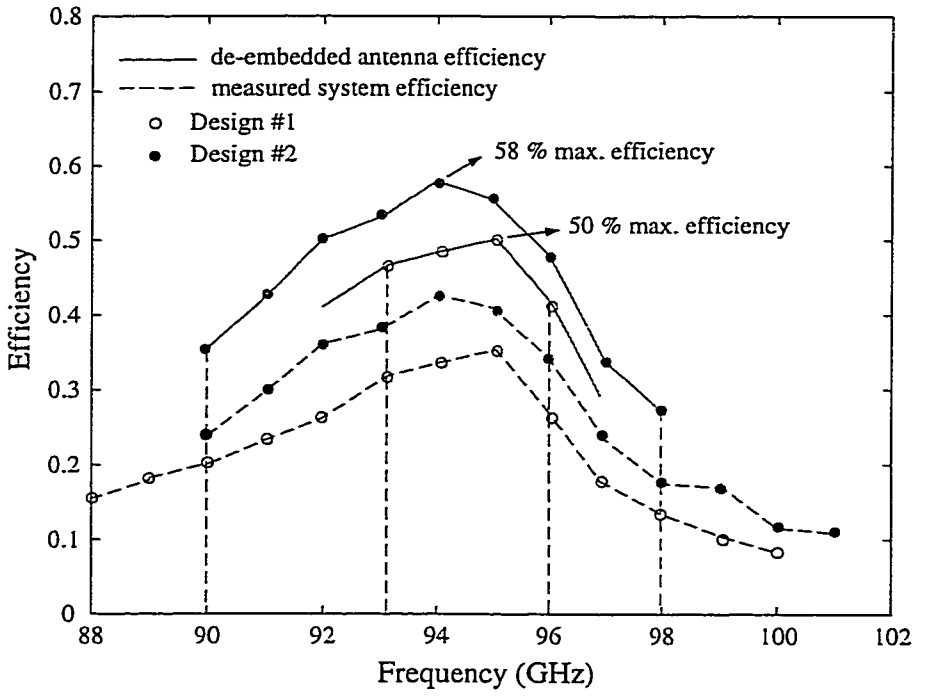

(b)

Figure 5.8: Measured radiation efficiency of a microstrip patch antenna built on a full 100 μm silicon wafer (a), and of a micromachined microstrip antenna (b).

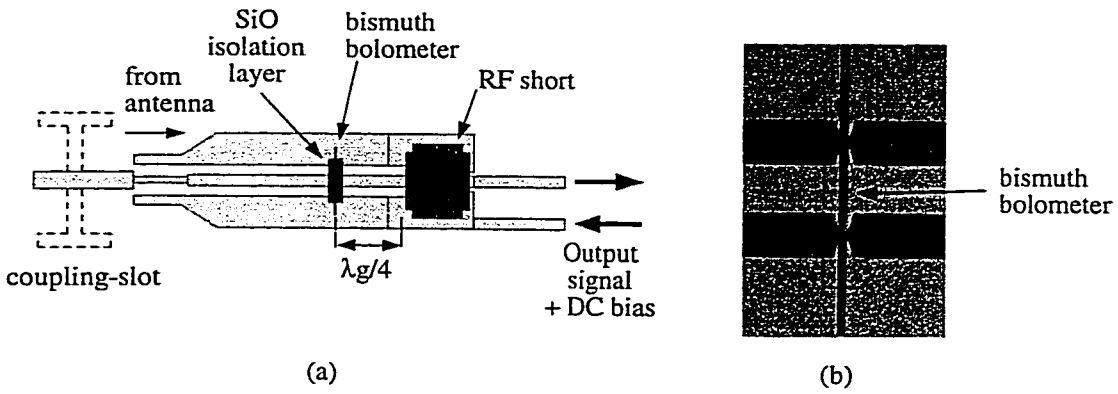

Figure 5.9: Integration of the bismuth bolometer to measure radiation patterns (a) and picture of the bismuth bolometer (b).

5.4 Radiation Patterns

To measure the radiation patterns of the micromachined microstrip antenna, a bismuth microbolometer is integrated into the circuit. The RF short in the cpw line is provided by a thin-film capacitor,300 μm $\times$ 200 μm $\times$ 1500 Åof evaporated SiO. Two 100 Ω bismuth bolometers (4 μm $\times$ 4 μm and 1000 Åthick) are placed in parallel $\lambda_g/4$ away from the RF short (where λ_g is the guided wavelength in the cpw line) and result in a 50 Ω bolometer resistance (Fig. 5.9).

The measured radiation patterns are shown in Figure 5.10 and are typical for microstrip antennas. It is seen that the cross-polarization level is below -20 dB and the front-to-back ratio is below -10 dB for both E- and H-plane directions. The ripples in the E-plane are due to the finite ground of the microstrip antenna ($3 \times 3\lambda_0$).

The back side radiation comes mainly from the feed H-slot radiation. In the design, the H-slot is lying on a silicon substrate (100 μm thick) on the backside and with the cavity on the front side (Fig. 5.1). This means that the H-slot will radiate mostly in the back side direction. The front and back side radiations for the Design #1 have been compared in the E-plane, from 90 to 102 GHz (Fig. 5.11). The

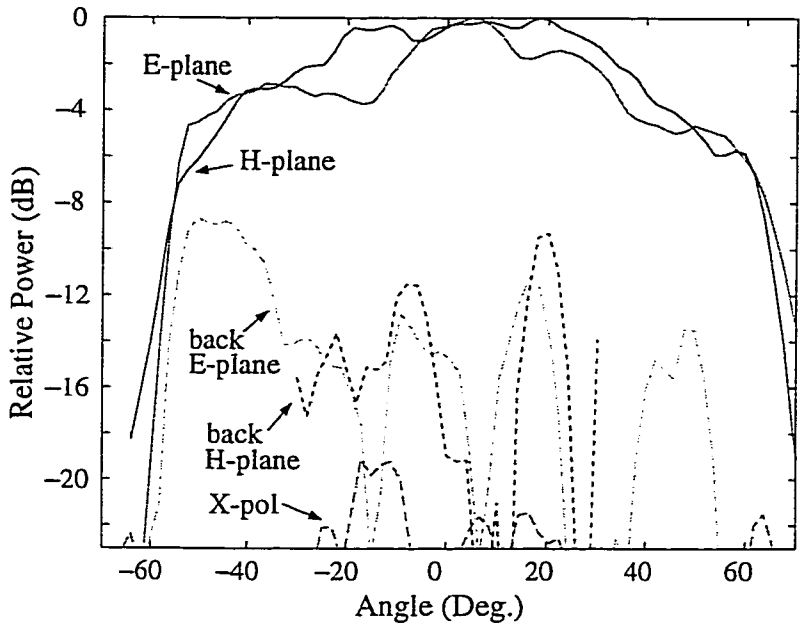

Figure 5.10: Measured radiation patterns of the micromachined microstrip antenna at 94 GHz.

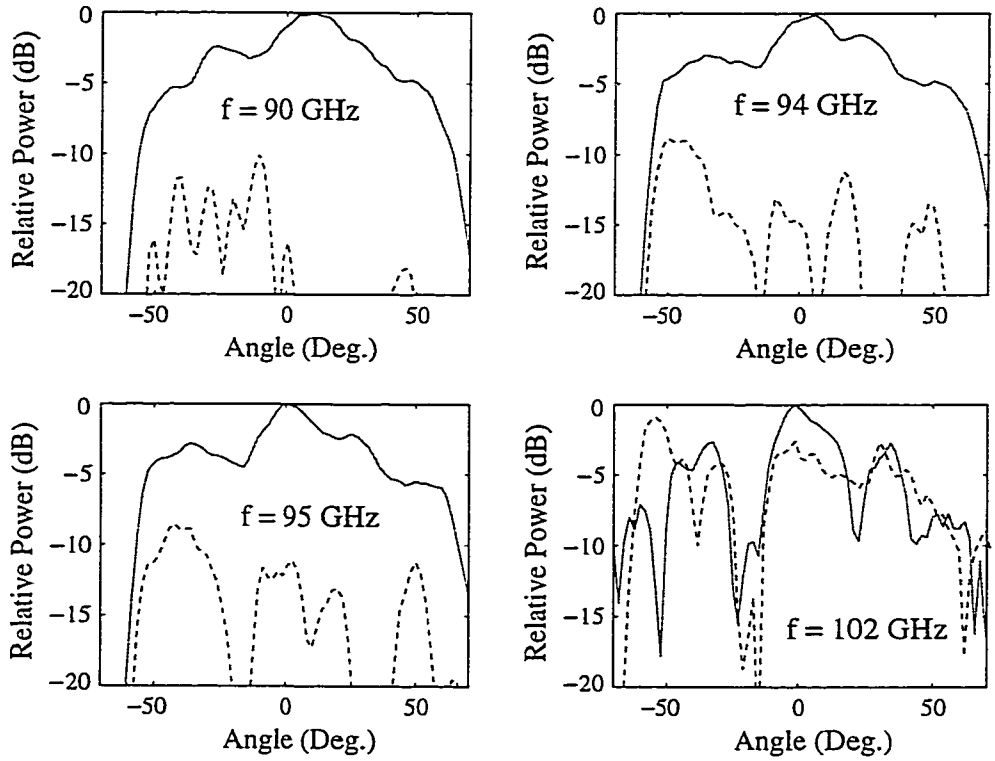

Figure 5.11: Front (—) versus back (– –) radiation measured in the E-plane from 90 to 102 GHz.

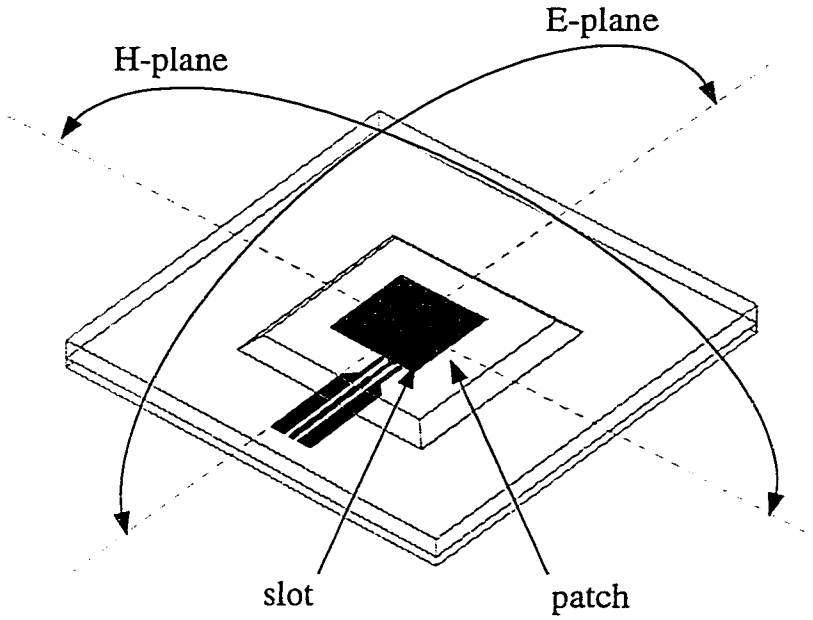

Figure 5.12: Definition of the E- and H-planes of the aperture-coupled microstrip antenna.

measured front-to-back ratio is -12 dB and increases with frequency as expected. At 102 GHz, the radiation pattern is greatly disturbed by the slot radiation since the slot is then close to resonance (Fig. 5.11(d)).

5.5 Mutual Coupling

It is important to reduce the mutual coupling between patches in the E- and H-plane directions for array applications (Fig. 5.12). The microstrip antenna can be simply viewed as 2 magnetic currents on grounded dielectric slab, roughly $\lambda_g/2$ apart. Surface waves and particularly the dominant TM_0 mode are triggered in the E-plane direction. In an array configuration, a high mutual coupling is then expected in the E-plane direction, and low in the H-plane and 45°-plane directions. One approach is to modify the shape of the cavities etched underneath the patches. Instead of etching only one wide cavity underneath the four microstrip antennas (Fig. 5.13(a)),

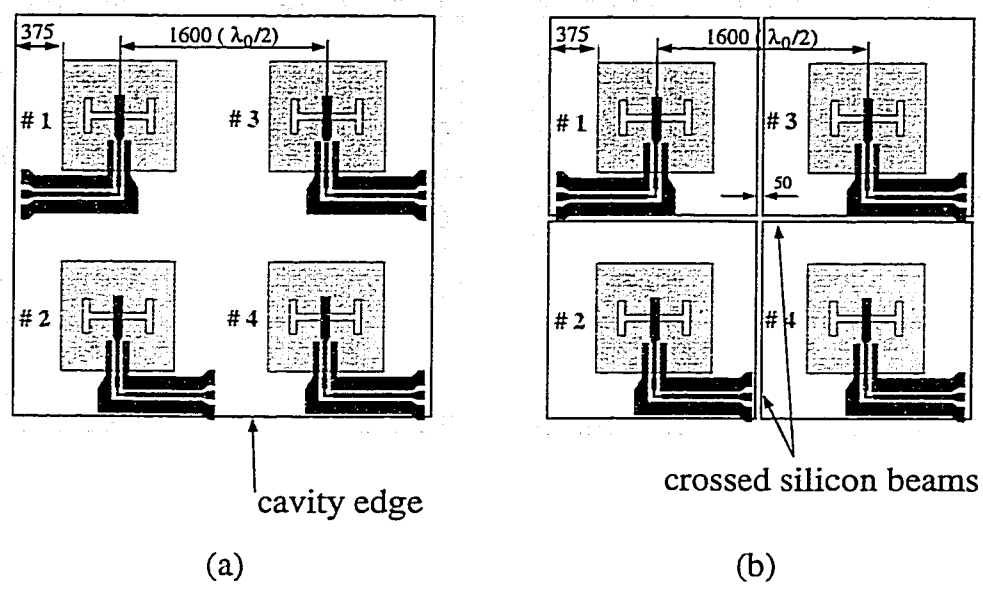

Figure 5.13: Layout of the 2 × 2 antenna array to measure the mutual coupling with one single cavity (a) and individuals cavities (b). All dimensions are in microns.

an individual cavity is used for each patch separated by a 50 μm wide silicon beam (Fig. 5.13(b)).

Quasi-static simulations of the microstrip patch on a micromachined substrate, with a 150 μm deep cavity in a 200 μm thick silicon substrate, and relying on finite element calculations of the geometry capacitances [57], show that the electromagnetic field is mostly confined inside the cavity below the patch antenna and not in the silicon substrate. It is also seen that the electric field extends inside the cavity widely away from the source, therefore increasing the crosstalk between elements (Fig. 5.14(a)). On the other hand, the electric fields are clearly confined underneath each patch antenna with the use of a 50 μm wide silicon beam separating the antennas (Fig. 5.14(b)).

Two different 2×2 micromachined antenna arrays with a spacing of $\lambda_0/2$ have been built to measure the mutual coupling: the first array with a single cavity and

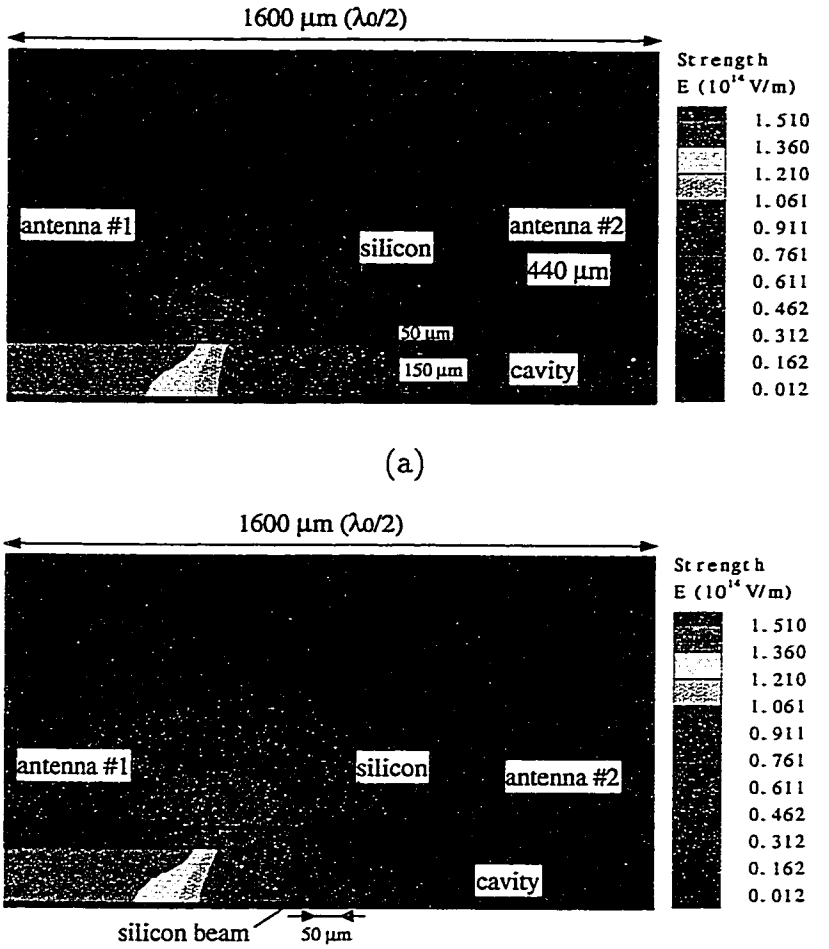

Figure 5.14: Quasi-static simulations of the electric fields around the patch antenna on a micromachined silicon substrate. The fields are confined inside the cavity in the E-plane direction (a), and silicon beams are used to isolate two adjacent elements (b).

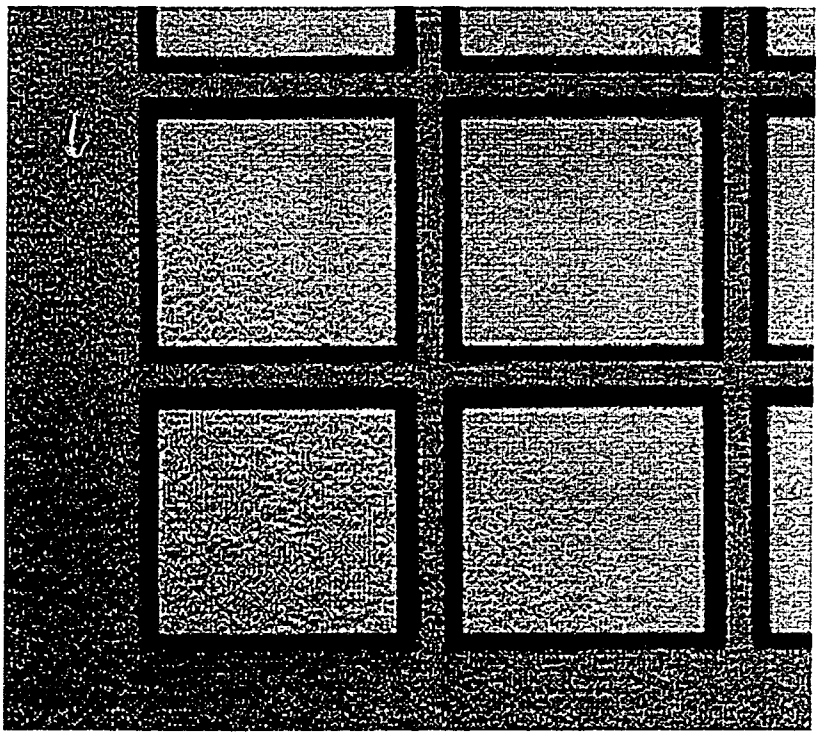

Figure 5.15: Picture of the four individual cavities with crossed silicon beams.

the second array with individual cavities and a crossed beam geometry (Fig. 5.15). The crosstalk in E- and H-plane directions is measured using W-band picoprobes on a HP8510 network analyzer. Figure 5.16 shows the S-parameters measured for both arrays in the E-, H- and 45°-directions. It shows that crossed silicon beams reduce the parasitic mutual coupling in the two main plane directions to less than -20 dB (Fig. 5.17). This coupling level is sufficiency low to design efficient phased arrays for W-band applications.

5.6 Conclusion

A high-efficiency aperture-coupled microstrip antenna has been developed at 94 GHz. The silicon substrate supporting the patch antenna is micromachined and a cavity is etched below the patch. This technique allows to reduce the dielectric constant of the substrate from $\epsilon_r = 11.7$ to close to $\epsilon_r = 4$. Therefore, a thicker sub-

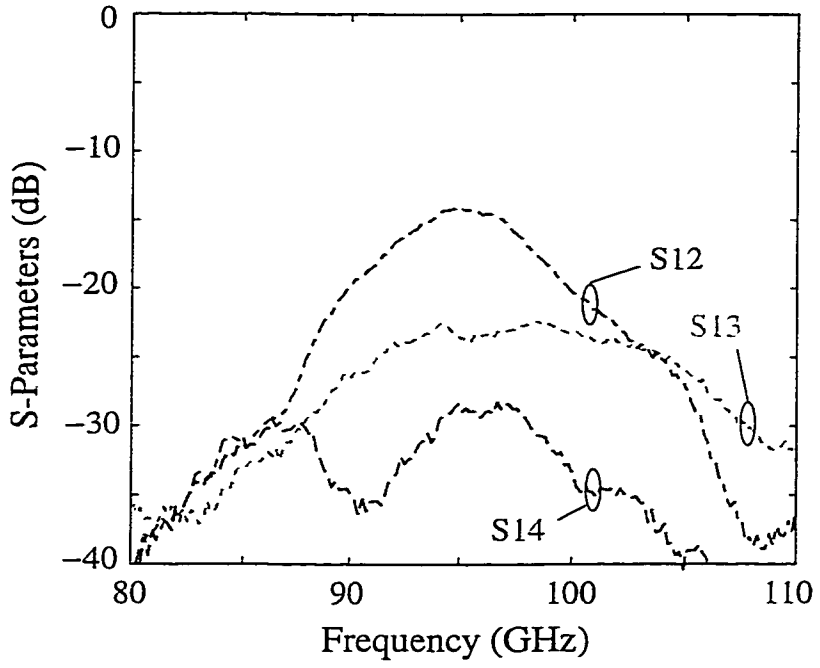

(a)

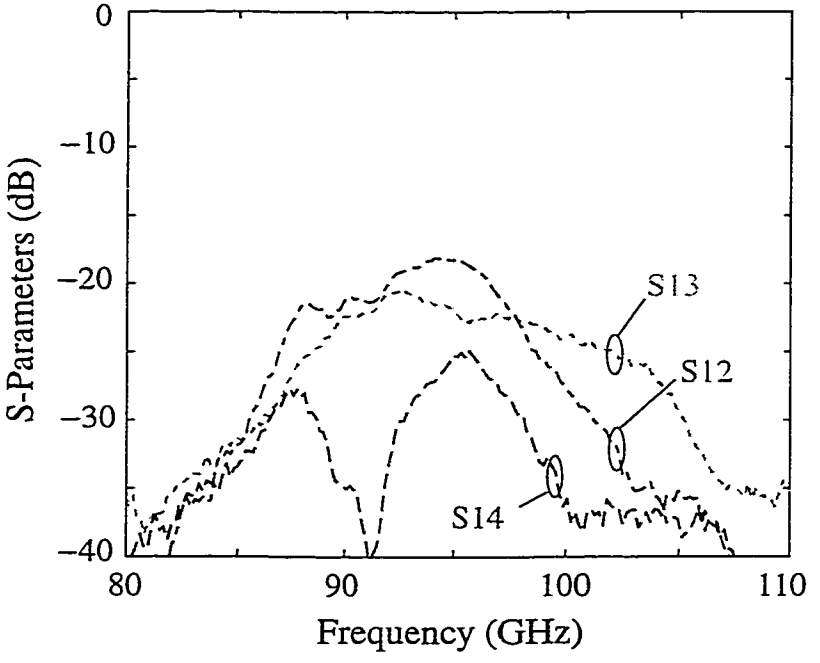

(b)

Figure 5.16: Measured mutual coupling comparison for the single cavity design (a) and individual cavities design (b). S12, S13, S14 correspond to the E-, H-, and 45°-plane directions, respectively.

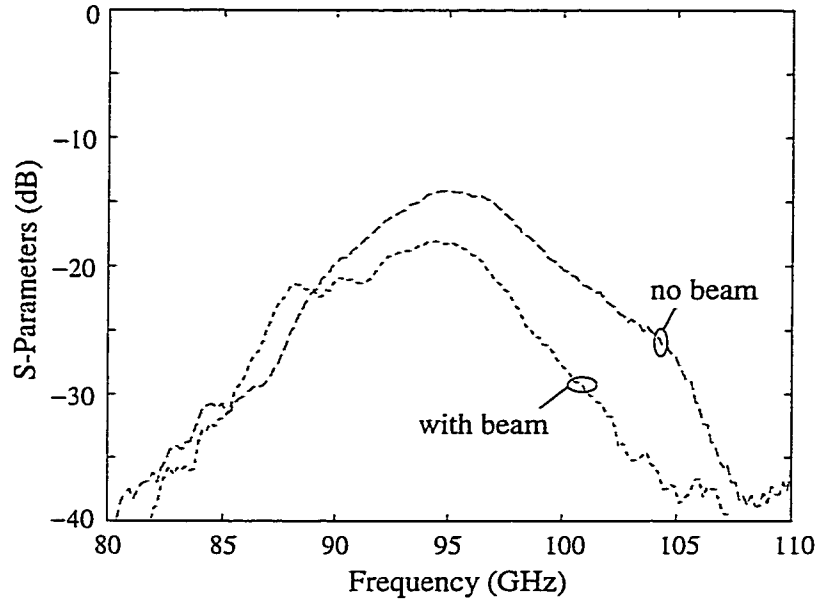

(a)

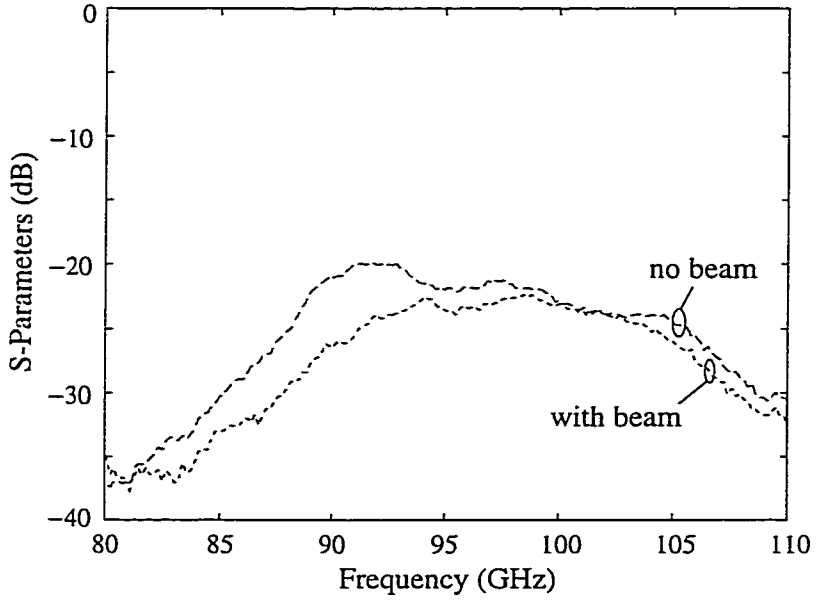

(b)

Figure 5.17: Measured mutual coupling comparison in the E- (a) and H-plane (b) directions.

strate is used (200 μm instead of 100 μm for a non-micromachined silicon substrate), resulting in an improved radiation efficiency from 28$\pm$5% to 58$\pm$5%. The design also includes a low-loss cpw-to-microstrip transition in order to integrate the antenna in a cpw-based RF circuit. The transition is based on electromagnetic coupling and has to be carefully designed in order to avoid the triggering of unwanted microstrip modes in the cpw lines, and this is the subject of Chapter 6. This aperture-coupled microstrip antenna has an excellent -10 dB bandwidth (10%), and good radiation patterns with a measured front-to-back ratio of 12 dB. The mutual coupling between adjacent elements in an array configuration is better than -20 dB when individual cavities are etched below each patch antenna. The microstrip antenna design is therefore low-cost, compact, compatible with silicon or GaAs MMIC technology, with excellent radiation performance, and can be used in millimeter-wave phased arrays for sensor and communication applications.

CHAPTER VI

W-BAND SINGLE LAYER VERTICAL TRANSITIONS

In the previous chapters, many approaches to reduce losses from surface waves were investigated. Several cpw and microstrip technologies were used, depending on the geometry. The choice of having a ground plane usually determines the type of transmission lines. However in more and more applications, combining cpw and microstrip lines can improve greatly the design, providing solutions for low-cost 3-dimensional fully integrated receivers. In Chapter 5, as an example, a 94 GHz aperture-coupled microstrip antenna, fed by a microstrip line, was coupled to a cpw output with the use of a cpw-to-microstrip transition.

Therefore, there is a need for low-loss, simple and wideband interconnections operating at W-band. Transitions based on electromagnetic coupling are more attractive than via-holes or wirebonds since they simplify the fabrication processes, particularly for millimeter-wave circuits. Also the simulation of the latter is complex and very time consuming. This chapter investigates three type of W-band transitions. First, two designs of a uniplanar transition from finite ground coplanar waveguide (fgc) to microstrip line are presented. One relies on straight stubs (Fig. 6.1(a)) and the other on radial stubs (Fig. 6.1(b)) to increase the bandwidth. Second, two

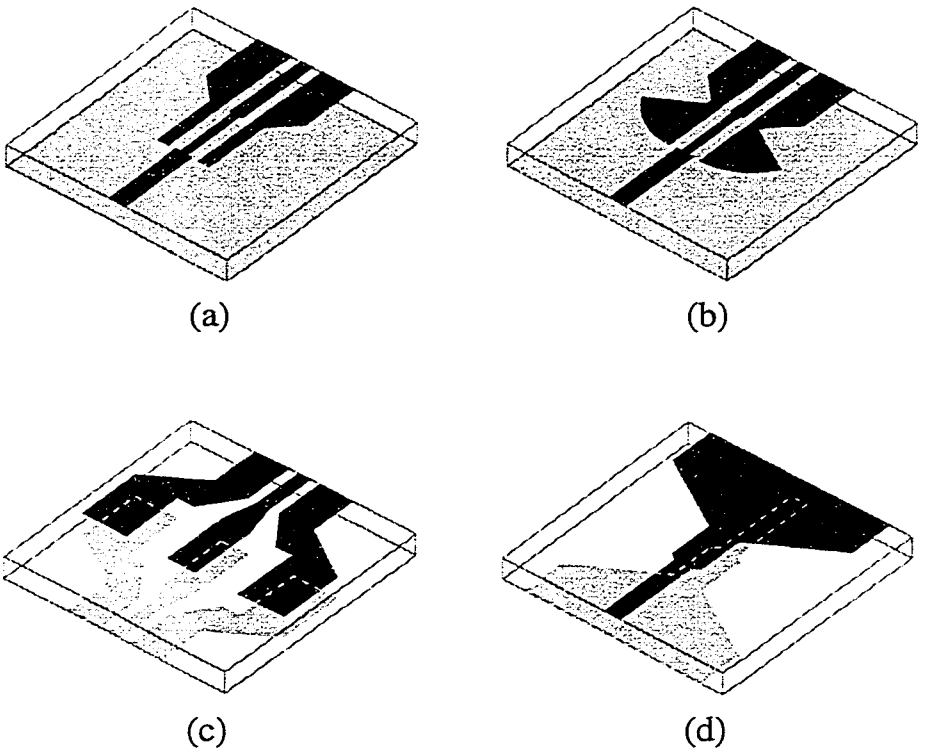

Figure 6.1: View of the w-band transitions: straight-stub cpw-to-microstrip (a), radial-stub cpw-to-microstrip (b), vertical cpw overlay (c) and vertical microstrip overlay (d).

vertical single-layer transitions are explored: one using cpw-mode coupling, first developped by Jackson in 1987 [65] (Fig. 6.1(c)), and one using microstrip-mode overlay (Fig. 6.1(d)). Vertical transitions provide a coupling between a mode propagating on the top surface of a substrate to a mode propagating on the bottom surface of the same substrate (surface-to-surface coupling).

6.1 W-Band Finite Ground Coplanar Waveguide (fgc) to Microstrip Line Transition

The cpw-to-microstrip transition based on electromagnetic coupling was first described in 1976 on alumina substrates ($\epsilon_r = 9.6$) and demonstrated from 5-11 GHz and from 11-18 GHz [60]. In this section the design is extended to W-band (centered

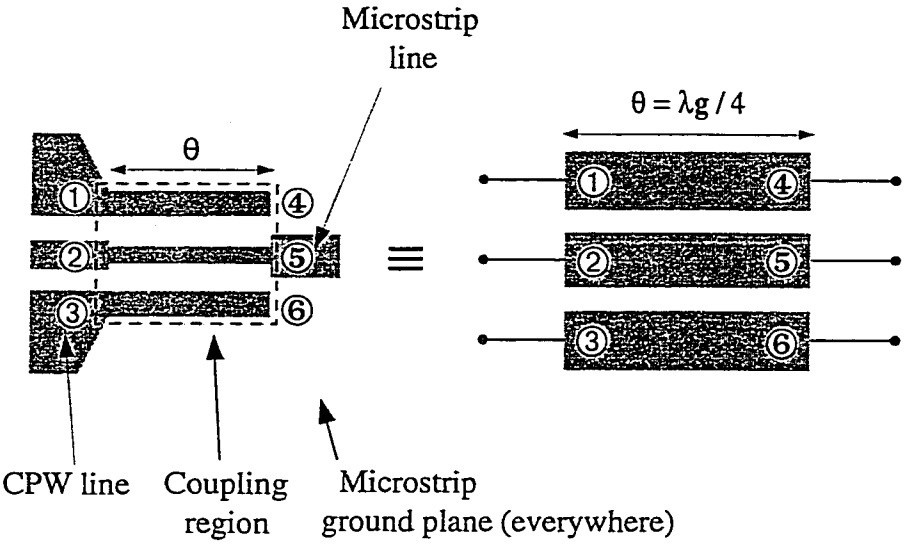

Figure 6.2: CPW-to-microstrip transition and the equivalent three-line microstrip coupler used to analyze and design the transition.

at 94 GHz), and a new wideband version of the transition is presented.

6.1.1 Transition Design

The transition has been designed following the procedure described by Pavlidis *et al.* [66], which considers the coupling region as a six-port network with a ground plane, or as three coupled-microstrip lines (Fig. 6.2). In this configuration, as seen in Figure 6.2, ports 2 and 5 are the input/output ports, respectively. The transition is $\lambda_g/4$ long at the center frequency of operation (f_0 = 94 GHz), where λ_g is the guided wavelength of the three-conductor line. Ports 4 and 6 are terminated by an open circuit, which results in ports 1 and 3 being short-circuited at f_0. The system is characterized by three mode impedances, which depend only on the geometry of the multi-wire network: width and spacing of the microstrip lines, height and dielectric constant of the substrate [66]. Figure 6.3 shows the different modes propagating along three coupled strip lines, the microstrip mode (A), the even cpw mode (B) and

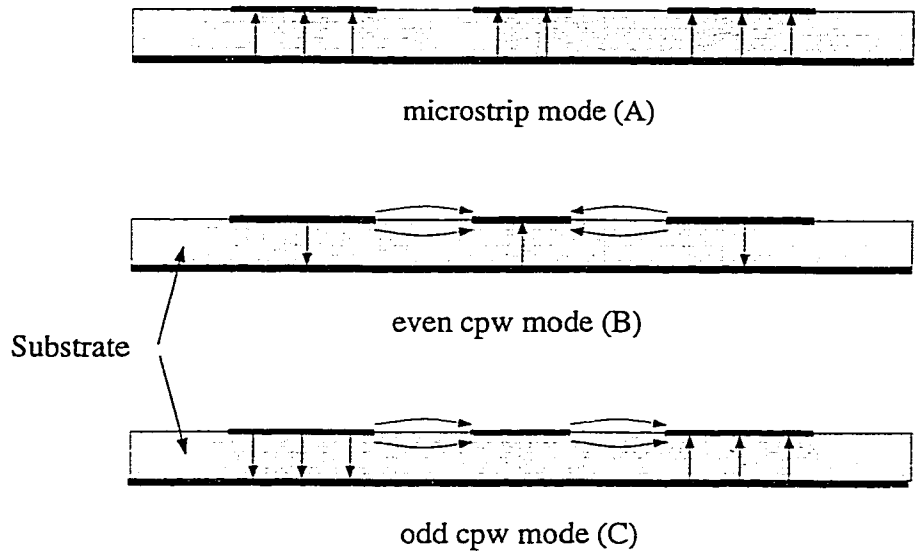

Figure 6.3: Field configuration of the microstrip mode (A), even cpw mode (B) and odd cpw mode (C) in a three-line coupler.

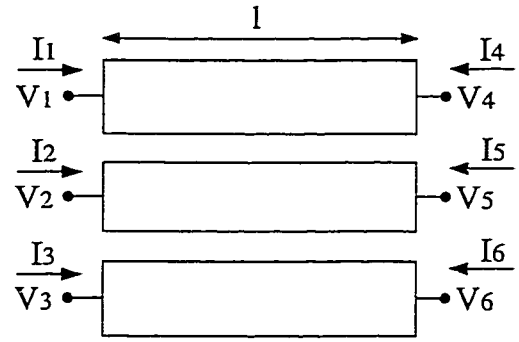

Figure 6.4: Voltage and current definitions in the three-line coupler.

the odd cpw mode (C) [67]. The mode impedances, Z_A, Z_B and Z_C, are deduced from the 2-D quasi-static capacitances [57]. For each mode, the quasi-static capacitances between the lines with the silicon substrate present, C_s, and with air only, C_a, are calculated. The characteristic impedance and effective dielectric constant of each mode, Z_A, Z_B, Z_C are then:

$$Z_n = \sqrt{\frac{\epsilon_0 \mu_0}{C_s C_a}} \quad n = A, B, C$$

$$\epsilon_{en} = C_s / C_a$$

The voltages and currents at each port are defined in Figure 6.4:

$$V_1 = V_1(0) \quad V_4 = V_1(l)$$
$$V_2 = V_2(0) \quad V_5 = V_2(l)$$
$$V_3 = V_3(0) \quad V_6 = V_3(l)$$
$$I_1 = I_1(0) \quad I_4 = -I_1(l)$$
$$I_2 = I_2(0) \quad I_5 = -I_2(l)$$
$$I_3 = I_3(0) \quad I_6 = -I_3(l)$$

In practical circuits, the odd cpw mode is suppressed with the use of air-bridges that equalize the two outer strips, and is not taken into account in the analysis. By symmetry, the structure can then be seen as a two port network with:

$$V_1 = V_3 \quad V_4 = V_6$$
$$I_1 = I_3 \quad I_4 = I_6$$

The total voltage V and current I at a position z along the line is the sum of the contributions of all modes, A, B and C, propagating in the $+z$ and $-z$ directions:

$$V(z) = V_{+A} e^{-j\beta_A z} + V_{-A} e^{j\beta_A z} + V_{+B} e^{-j\beta_B z} + V_{-B} e^{j\beta_B z} + V_{+C} e^{-j\beta_C z} + V_{-C} e^{j\beta_C z}$$

$$I(z) = Y_A(V_{+A} e^{-j\beta_A z} - V_{-A} e^{j\beta_A z}) + Y_B(V_{+B} e^{-j\beta_B z} - V_{-B} e^{j\beta_B z}) + Y_C(V_{+C} e^{-j\beta_C z} - V_{-C} e^{j\beta_C z})$$

where β and Y are the mode propagation constant and characteristic admittance, respectively. The impedance matrix of the whole system is then:

$$\begin{bmatrix} V_1 \\ V_2 \\ V_4 \\ V_5 \end{bmatrix} = \begin{bmatrix} Z_{11} & Z_{12} & Z_{14} & Z_{15} \\ Z_{21} & Z_{22} & Z_{24} & Z_{25} \\ Z_{41} & Z_{42} & Z_{44} & Z_{45} \\ Z_{51} & Z_{52} & Z_{54} & Z_{45} \end{bmatrix} \begin{bmatrix} I_1 \\ I_2 \\ I_4 \\ I_5 \end{bmatrix}$$

Solving for V and I, and using symmetry conditions, each element of the Z-matrix can be written as a function of the mode impedances Z_A, Z_B, resulting in [68]:

$$Z_{11} = Z_{22} = Z_{44} = Z_{55} = -j(Z_A + Z_B)cot\theta/2$$

$$Z_{12} = Z_{21} = Z_{45} = Z_{54} = -j(Z_A - Z_B)cot\theta/2$$

$$Z_{14} = Z_{41} = Z_{25} = Z_{52} = -j(Z_A - Z_B)csc\theta/2$$

$$Z_{15} = Z_{51} = Z_{24} = Z_{42} = -j(Z_A + Z_B)csc\theta/2$$

where θ is the average electrical length of the line:

$$\theta = (\beta_A + \beta_B)/2$$

The dimensions of each coupled line are then calculated to optimize the insertion and return losses of the transition, referenced to 50 Ω. The input line is a 50 Ω finite ground coplanar waveguide (fgc), The output line is a 50 Ω microstrip line. In this design, the lower ground plane extends everywhere. However, since the ground plane of the fgc line is finite, no unwanted parallel-plate modes are triggered in the substrate between the coplanar lines and the ground plane.

In the second design, the straight coupling stubs are replaced by wideband radial stubs to increase the bandwidth of the transition. As will be shown later, this results in 25% more bandwidth than the straight stubs.

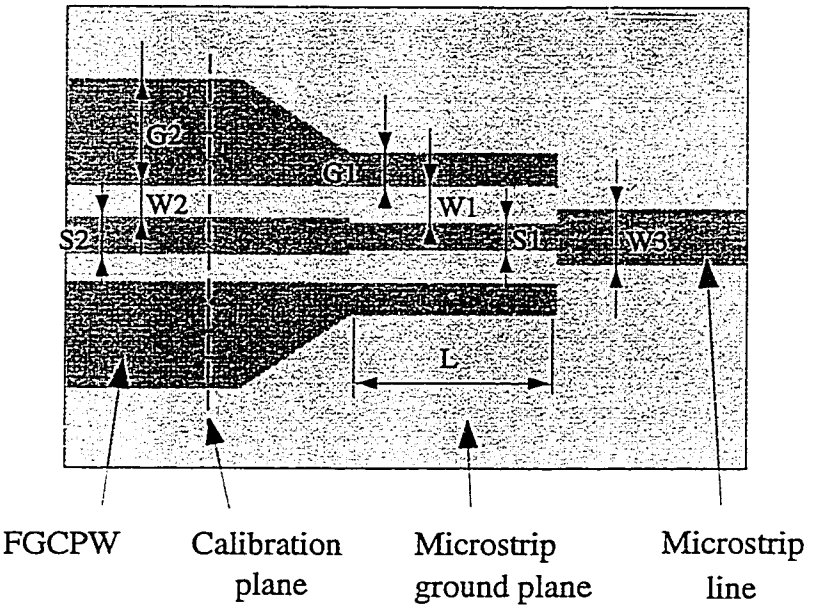

(a)

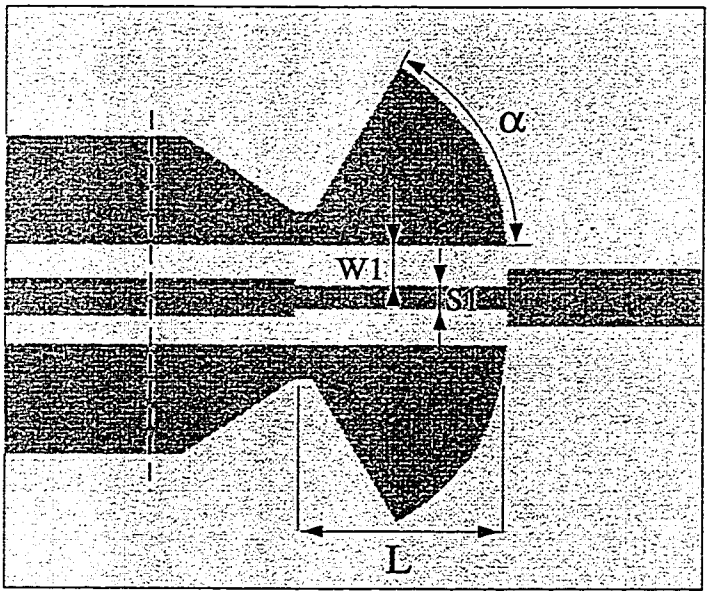

(b)

Figure 6.5: CPW-to-microstrip transition with straight coupling stubs (a) and with radial coupling stubs (b).

6.1.2 W-band Measurements

A/ DESIGN

Two fgc-to-microstrip transitions have been designed, fabricated and tested in the W-band region (75-110 GHz): a straight stub design (transition A) and a radial stub design (transition B). The transitions are built on a 120 μm thick high-resistivity Silicon substrate ($\epsilon_r = 11.7$). The circuit is mounted on a metallized Silicon wafer to provide the ground plane. The evaporated gold is 9000 $\AA$ (more than 3 skin-depths at 94 GHz). The fgc input line dimensions are $S2 = 50$ μm, $W2 = 45$ μm and $G2 = 145$ μm (Fig. 6.5(a)) corresponding to a characteristic impedance of $Z_c = 47$ Ω [3]. The microstrip line is 70 μm wide, corresponding to a characteristic impedance of $Z_m = 50$ Ω.

The coupling region is chosen to be $L = 280$ μm long ($\lambda_g/4$ at 94 GHz). For transition A, the dimensions are $S1 = 30$ μm, $W1 = 55$ μm, and the straight stubs are $G1 = 45$ μm wide (see Fig. 6.5(a)), corresponding to fundamental mode impedances of $Z_{oo} = 13$ Ω, $Z_{oe} = 130$ Ω and $Z_{ee} = 50$ Ω. For transition B, the dimensions are also $S1 = 30$ μm, $W1 = 55$ μm, and the angle of the radial stubs is 60^o (Fig. 6.5(b)).

B/ MEASUREMENTS

The S-parameters of two back-to-back transitions, separated by an 860 μm-long microstrip line, as shown in Figure 6.6, are measured with W-band picoprobes on a HP8510 network analyzer. The VNA is calibrated before the transition region using TRL calibration techniques and the calibration plane is shown in Figure 6.5. The measured performances of the transitions are compared with IE3D Method-of-Moment [59] simulations and are shown in Figure 6.7(a) (straight stubs) and Figure 6.7(b) (radial stubs).

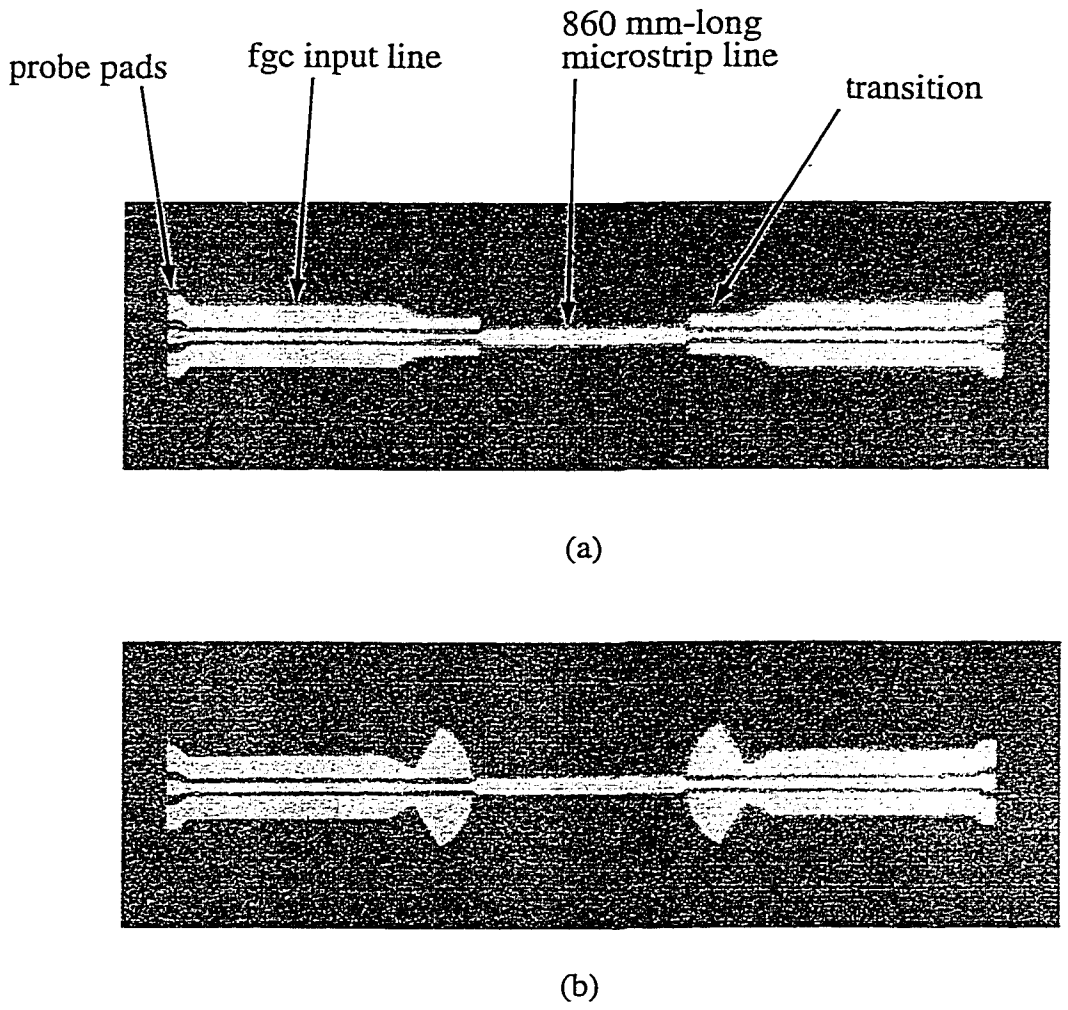

Figure 6.6: Pictures of the two fabricated back-to-back fgc-to-microstrip transitions showing the straight-stub design (a) and the radial-stub design (b).

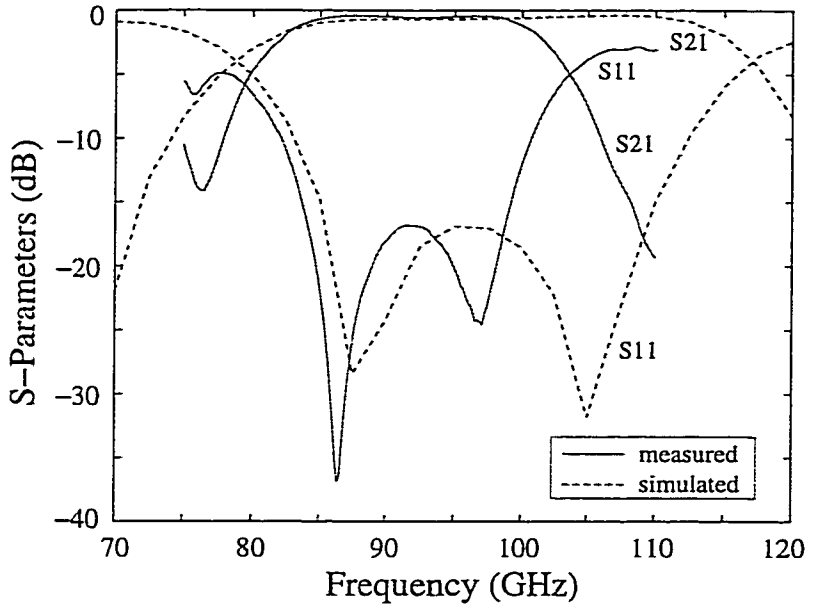

(a)

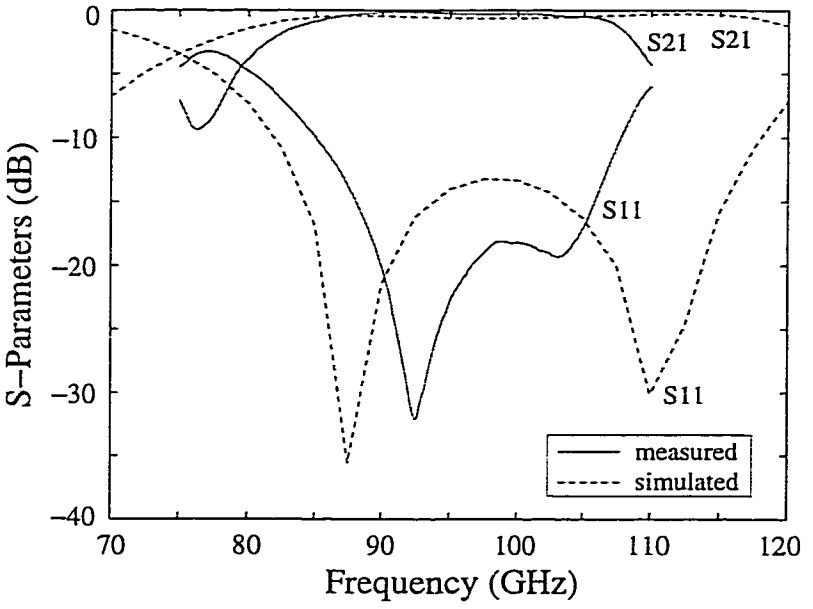

(b)

Figure 6.7: CPW-to-microstrip straight-stub (a) and radial-stub (b) transitions S-parameters (-) vs. Method-of-Moment simulation (- -).

The measured total insertion loss is 0.4 dB from 85 GHz to 95 GHz for the straight-stub transition and includes two transitions and the microstrip line, and the 3-dB bandwidth is 20%. The loss of the microstrip line (w=70 μm, h=120 μm) is calculated to be 0.04 dB. The deduced insertion loss for a single transition is 0.18 dB. The measured return loss is better than -17 dB from 83 GHz to 100 GHz providing a bandwidth of 20%. However, the IE3D simulations give a wider bandwidth as shown in Figure 6.7(a) and Figure 6.7(b). The differences in frequencies between the measurements and the IE3D simulations are due to the presence of a strong parasitic microstrip mode propagating below the two cpw ground strips. As described in Chapter 5, the probe measurement only picks up the cpw component of the signal, resulting in a microstrip mode standing wave in the circuit, between the probe pads and the open stubs, while the IE3D simulations describe the behaviour of all the modes, due to the definition of the ports of the fgc lines.

The radial-stub transition shows very similar performances but is more wideband: 0.18 dB insertion loss, 3-dB bandwidth of 25%, and a return loss better than -17 dB from 85 GHz to 110 GHz. This bandwidth covers nearly the entire W-band region and the radial-stub transition can be used in cpw-to-microstrip circuits VNA on-wafer measurements. However, the straight-stub transition is more compact and might be prefered when space is the main issue on the wafer.

6.2 W-band cpw-to-cpw Transition

6.2.1 Transition Design

The cpw-to-cpw transition described by Jackson [65] consists of an overlay of two fgc lines that can support even- and odd-modes. The dimensions of the overlay region are designed so that the even- and odd-mode impedances result in a perfect

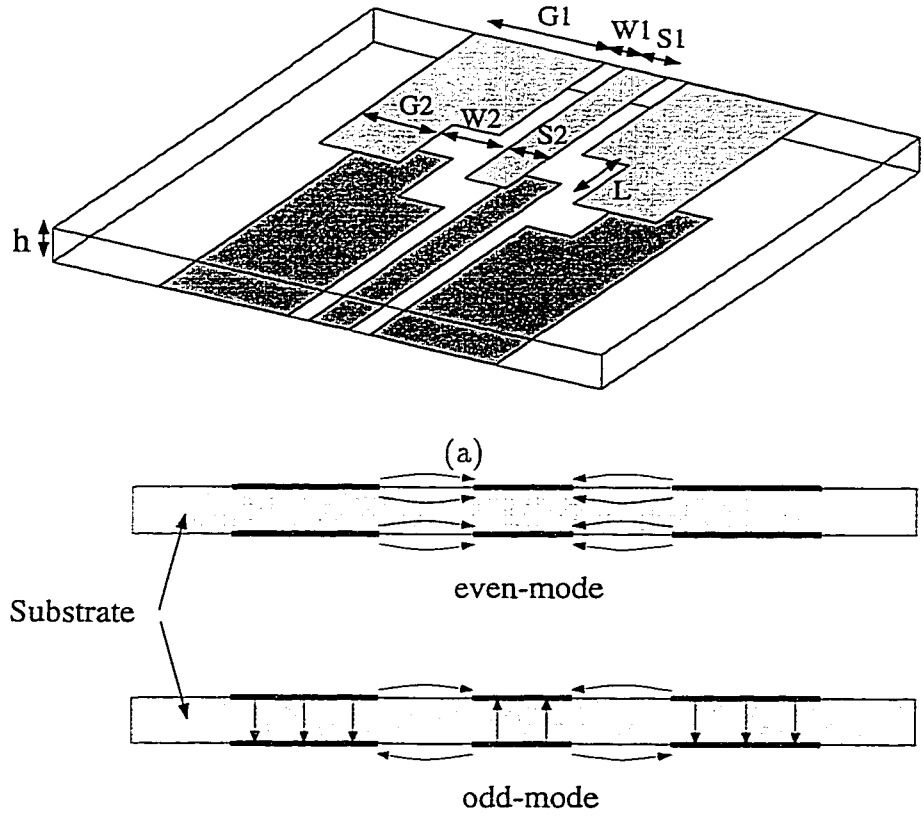

Figure 6.8: Perspective view of the cpw-to-cpw single-layer transition (a), and electric field configuration for the even and the odd cpw-mode (b).

match at the frequency of interest. The length of the transition is chosen to be $\lambda_g/4$. Figure 6.8(a) shows the perspective view and Figure 6.8(b) the cross-section of the transition as well as field distribution for the even and odd modes. The cpw-to-cpw transition has been designed, fabricated and tested for silicon substrates ($\epsilon_r = 11.7$) in the 75-110 GHz region (Fig. 6.9). The substrate is 100 μm thick (corresponding to $\lambda_d/9$ at 94 GHz, where λ_d is the dielectric wavelength). The fgc input line dimensions are designed to result in a characteristic impedance of 50 Ω. The dimensions of the coupling region are *S2*=120 μm, *W2*=195 μm and *G2*=195 μm. The resulting impedances are Z_A=130 Ω and Z_A=35 Ω, with $\epsilon_A = 7.5$ and $\epsilon_B = 3.5$. At 94 GHz, the guided wavelengths of the two modes are therefore λ_A=1.17 mm and λ_B=1.71 mm. The coupling region dimensions and the shape of the taper have been numerically optimized with IE3D [59]. To measure the influence of the overlay (coupling) region length on the transition, overlay regions of *L*=210, 280 ($\lambda_g/4$ at 94 GHz) and 350 μm long are fabricated. The evaporated metal is 8000 $\AA$ of gold, corresponding to around 3 skin depths at 94 GHz. A photograph of the top and bottom lines of the transition is shown in Figure 6.10.

6.2.2 W-band Measurements

VNA measurements of two back-to-back transitions separated by a 0.9 mm-long 50 Ω fgc line are made using TRL calibration techniques. Figure 6.11(a) compares the measurement and simulation (IE3D) results of the cpw-to-cpw vertical transition with an overlay length of 280 μm and Figure 6.11(b) presents the measured S-parameters for transitions with three different coupling region lengths. A good agreement is obtained between measurements and simulations (IE3D) from 75 to 110 GHz (Fig. 6.11(a)). Figure 6.11(b) clearly shows the bandwidth shift of the

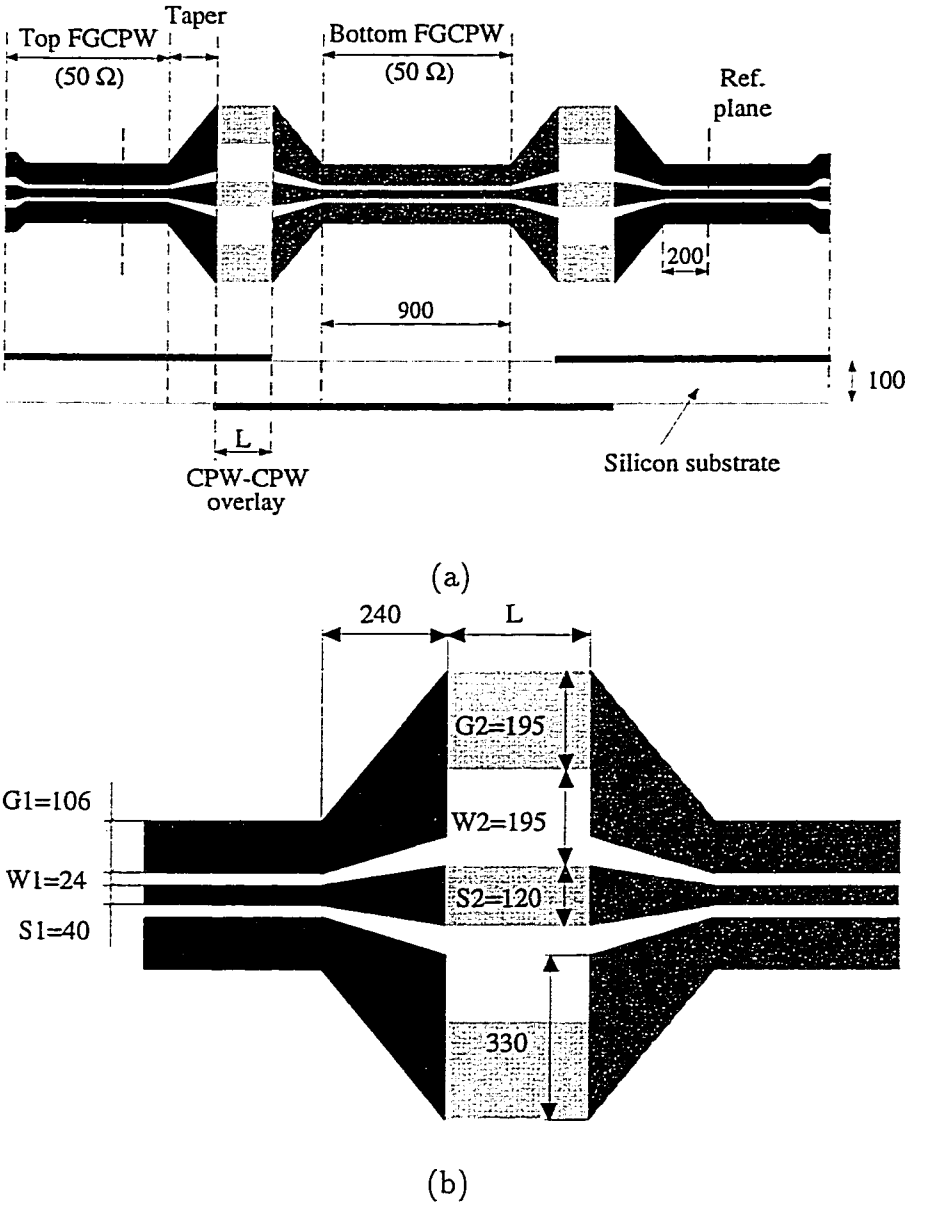

Figure 6.9: Layout of the two back-to-back cpw-to-cpw transitions (a) and close view of one single transition (b). All dimensions are in microns.

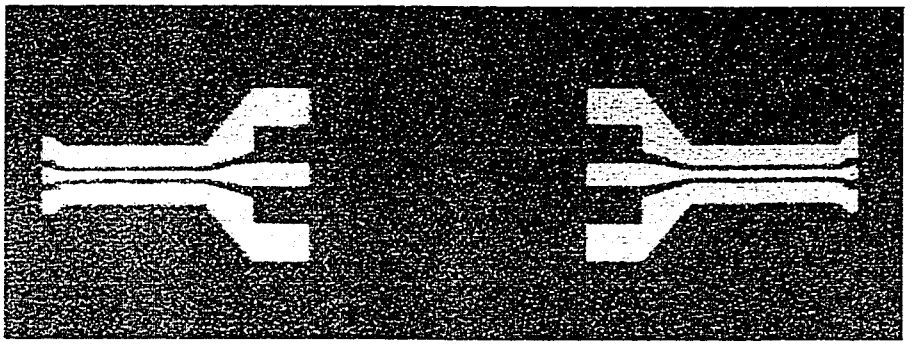

(a)

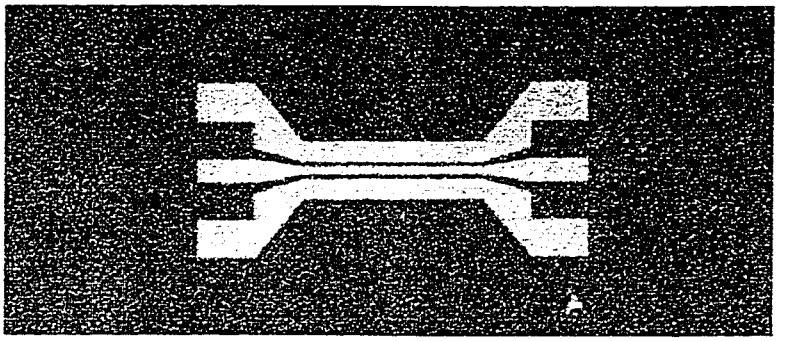

(b)

Figure 6.10: Picture of the fabricated back-to-back cpw-to-cpw transition, top (a) and bottom (b). Dimensions are found on Figure 6.9.

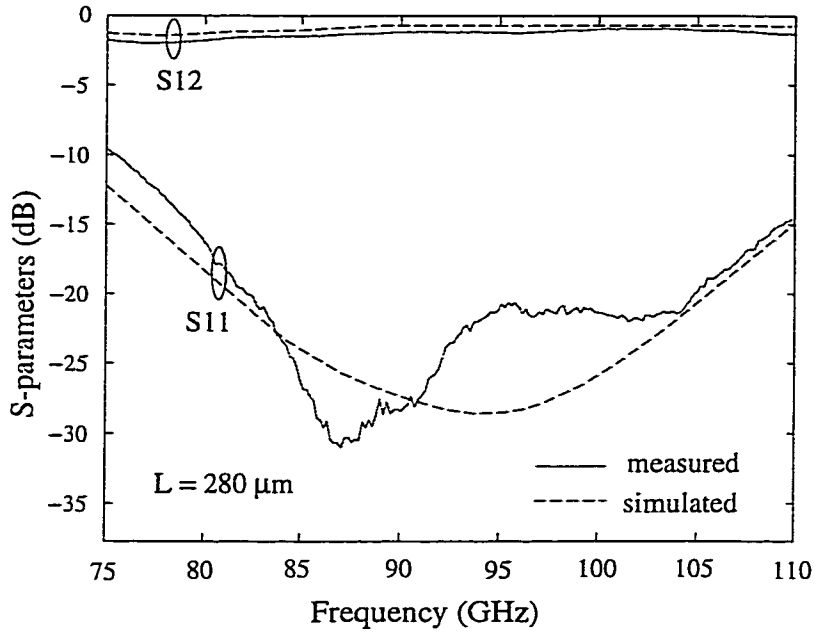

(a)

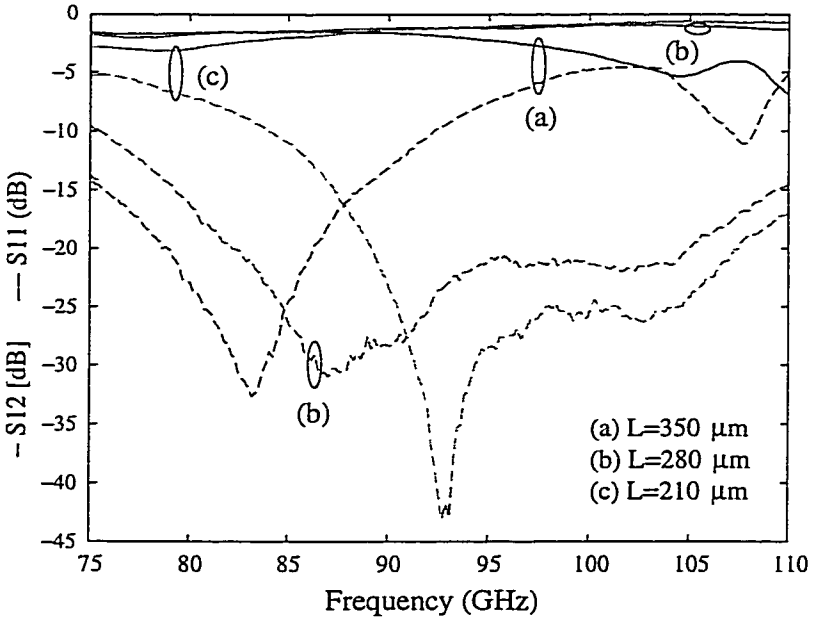

(b)

Figure 6.11: Measured and simulated (IE3D) W-band S-parameters of two back-to-back cpw-to-cpw transitions shown in Figure 6.9.

transition versus the overlay region length, L. The best transition for the 75-110 GHz frequency band is obtained with L=280 μm, which is approximately equal to $\lambda_d/4$ at 96-100 GHz. The total measured loss is -0.9 dB at 100 GHz for L=280 μm, with a return loss below -22 dB. The measured loss for a fgc line is 0.35 dB/mm at 94 GHz, so the deduced insertion loss per transition is 0.25 dB from 85-110 GHz and 0.6 dB over the whole measurement frequency band (75-110 GHz).

6.3 W-band Microstrip-to-Microstrip Transition

6.3.1 Transition Design

The third transition presented in this chapter uses microstrip-mode coupling. First, a cpw-to-microstrip transition is needed so as to allow input and output W-band coplanar-probe measurements (Fig. 6.12). The transition is designed following the experimental results presented by Strauss [69]. This type of cpw-to-microstrip transition uses two 90°-open stubs (280 μm long) to provide an effective short at the cpw-microstrip interface, and strong field coupling between the fgc ground planes and the metal backside of the microstrip line. The length of these two stubs is chosen to be $\lambda_g/4$ at the frequency of interest. All dimensions of this transition have been numerically optimized using IE3D [59] for the 75-110 GHz frequency band. The 50 Ω fgc input line dimensions are the same as in part II. The microstrip line is 74 μm wide resulting in a characteristic impedance of 50 Ω. The substrate is 100 μm thick. The metal evaporated is 8000 $\mathring{A}$ of gold.

Two circuits having the same total length are fabricated in order to deembed the insertion loss of the vertical microstrip-to-microstrip transition. The first circuit is composed of only a simple microstrip line section between the two cpw-to-microstrip transitions (Reference Circuit, Fig. 6.12(a)), and the second circuit includes two back-

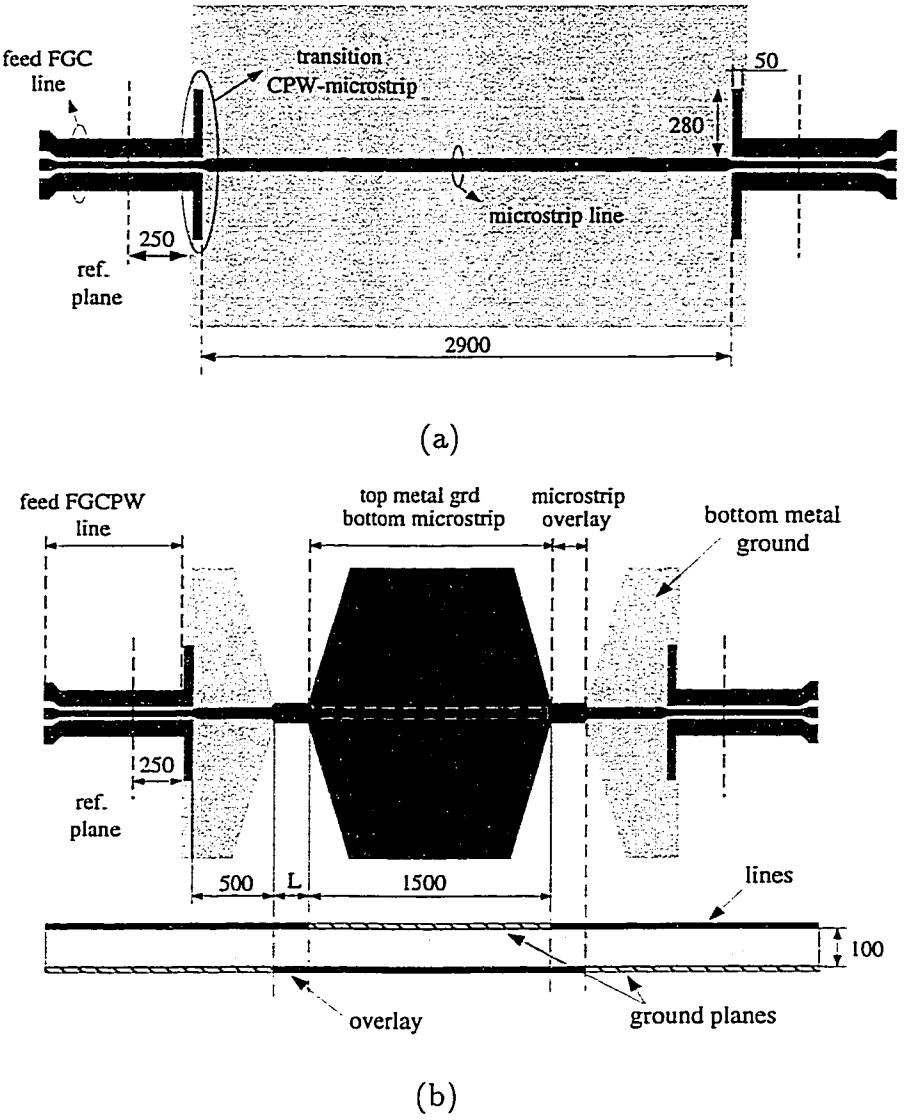

Figure 6.12: Layout of two back-to-back cpw-to-microstrip transitions including: a microstrip line of 2900 μm long (Reference Circuit) (a), and two back-to-back vertical microstrip-to-microstrip transitions (VMMT) (b).

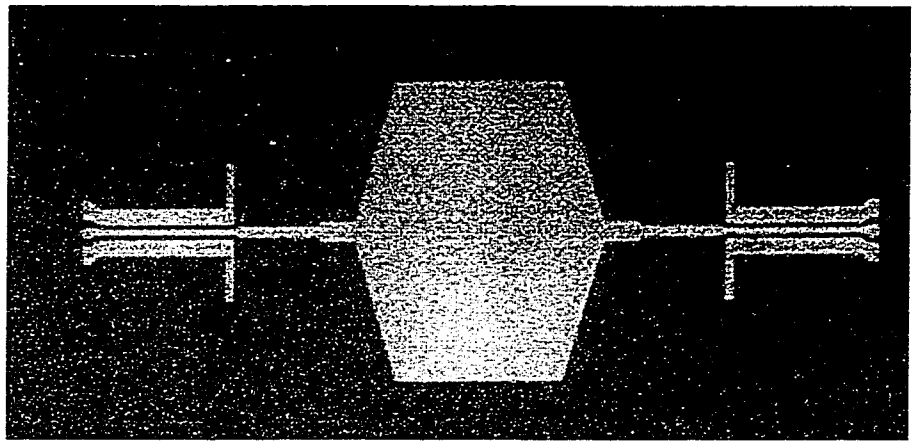

(a)

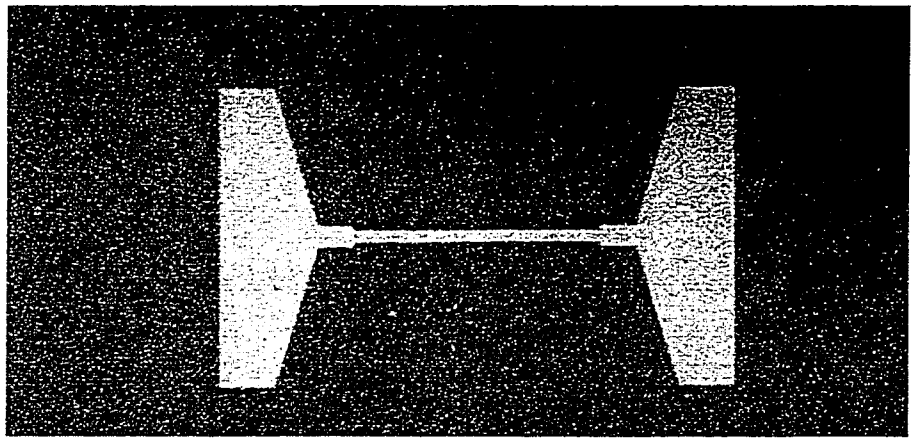

(b)

Figure 6.13: Picture of the fabricated back-to-back microstrip-to-microstrip transition, top (a) and bottom (b). Dimensions are found on Figure 6.12.

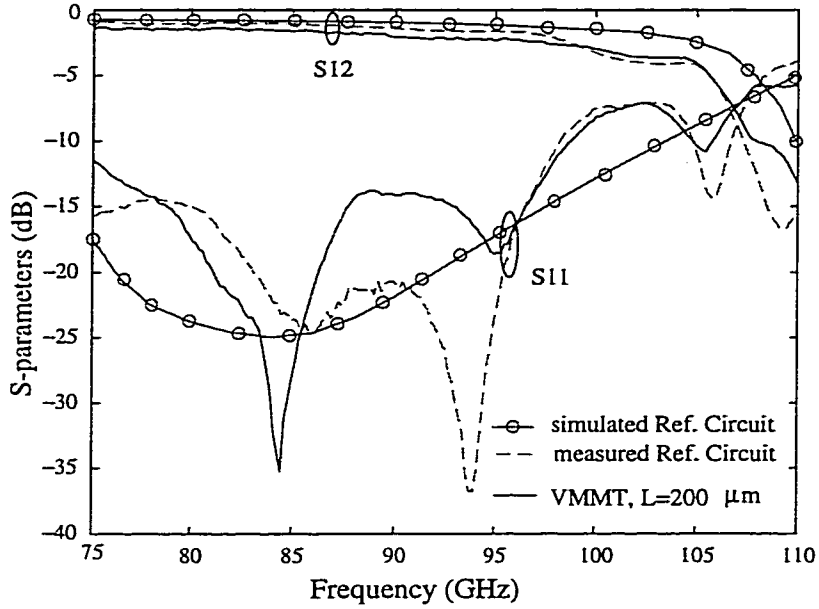

Figure 6.14: Measured and simulated (IE3D) S-parameters of two back-to-back cpw-to-microstrip transitions including a long microstrip line section (Reference Circuit). Also included is the measured of two back-to-back vertical microstrip-to-microstrip transitions as shown in Figure 6.12(b).

to-back vertical microstrip-to-microstrip transitions (VMMT Circuit, Fig. 6.12(b)). With these circuits, the effect of vertical microstrip-to-microstrip transition can be characterized by a direct comparison. The electromagnetic coupling between the top and the bottom microstrip surfaces occurs in the coplanar strip overlay. The coupling region is composed of a vertical 130 μm wide coplanar strip line resulting in a 50 Ω characteristic impedance. To measure the influence of the coupling region length on the microstrip-to-microstrip transition, overlay lengths of 100, 200 and 500 μm have been designed. Preliminary designs were done at 1-2 GHz using a microwave model and then scaled to 94 GHz. A picture of the top and bottom lines of this transition is shown in Figure 6.13.

6.3.2 W-band Measurements

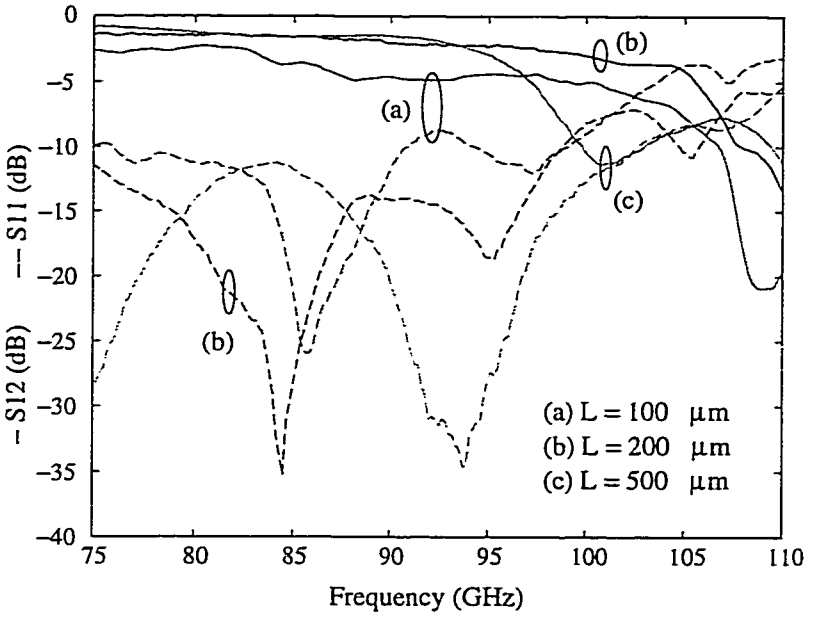

Figure 6.15: Measured S-parameters of two back-to-back vertical microstrip-to-microstrip transitions versus the coupling region length, L.

The microstrip-based transition has been designed, fabricated and tested for silicon substrates ($\epsilon_r = 11.7$) in the W-band region (75-110 GHz). VNA measurements of two circuits back-to-back transitions are made using TRL calibration techniques (Fig. 6.14 and 6.15). A good agreement is obtained between the simulations (IE3D) and the measurements of the two back-to-back cpw-to-microstrip transitions including a long microstrip line section (Fig. 6.12(a)). The ripples in the measured S11 curve were not predicted by the numerical simulations (IE3D). The general inacurracies (at second order) of numerical packages in high-Q ($\epsilon_r = 11.7$) structures at millimeter-wave frequencies are due to the simulation of the exact current distribution in the strip lines. The overlay length of microstrip-to-microstrip transition is L=200 μm. The total measured loss per transition is extracted by a direct comparison of the two measured S-parameters curves and is equal to 0.2 dB.

Figure 6.15 presents the measured S-parameters of the back-to-back transition for

different overlay lengths. Compared to the overlay length (L) of 200 μm, an increase of around 1.2 dB for the insertion loss is observed for a reduction of overlay length to 100 μm. The increase of insertion and return losses is attributed to the parasitic proximity coupling between the top and the bottom microstrip metal ground plane. On the other hand, a decrease of the transition bandwidth is observed for a longer overlay length (L=500 μm). This is due to the lower cutoff frequency of the strip overlay region. Therefore, an optimum overlay length for this vertical microstrip-to-microstrip transition is around 200 μm for W-band applications.

6.4 Conclusion

Three low-loss wideband W-band transitions combining cpw and microstrip technologies have been demonstrated on silicon substrates ($\epsilon_r = 11.7$). These transitions rely on electromagnetic coupling and are easy to fabricate with simple front- and back-side photolithography, since they do not require via-holes nor wirebonds. First, uniplanar cpw-to-microstrip transitions on 100 μm silicon substrates have less than -0.2 dB insertion loss per transition over a 20% bandwidth (83-100 GHz). The coupling from microstrip mode to cpw mode is provided by a virtual short-circuit between the cpw grounds on the top surface and the microstrip ground plane on the bottom surface of the substrate, by the use of $\lambda_g/4$-long straight stubs. The transition bandwidth can be increased to 25% (83-100 GHz) if radial stubs are used without degradating the insertion loss. Second, two vertical transitions, where the input and output ports are on the other sides of the same substrate (100 μm-thick silicon), were developed. The first vertical transition is based only on cpw lines and uses overlaying fgc lines. The transition insertion loss is 0.25 dB over the whole W-band range (75-110 GHz). The second vertical transition uses only microstrip lines,

and the coupling occurs in a strip line overlay. This transition is not dependant on the length ot the strip line overlay. All three transitions, cpw-to-microstrip, cpw-to-cpw and microstrip-to-microstrip, are compact and the transition region is smaller than $\lambda_g/4$ (280 μm at 94 GHz). The transitions have many applications in low-loss, low-cost fully integrated 3-dimensional receivers, in cpw-probe to microstrip circuit measurements and in millimeter-wave packaging and vertical interconnects.

CHAPTER VII

CONCLUSIONS AND FUTURE WORK

The objective of this thesis is to find simple solutions to eliminate surface waves losses which greatly affect the radiation performance and bandwith of millimeter-wave front-end receivers and planar antennas built on standard high dielectric-constant MMIC substrates ($\epsilon_r = 11.7$ for silicon and $\epsilon_r = 12.9$ for GaAs).

7.1 Conclusions

Low-loss Schottky-diode receivers are demonstrated in Chapters 2 and 3. The designs are simple, and are fabricated using flip-chip Schottky diodes, cpw lines and matching networks. Both receivers are built on a silicon substrate and placed on a high-resistivity silicon lens which eliminates substrate modes. The first receiver consists of a double-slot antenna and a fundamental Schottky-diode mixer placed at the center of the antenna. The measured SSB conversion loss is 9.3±0.3 dB at 86-90 GHz. However it requires a quasi-optical LO injection, and a quasi-optical diplexer to combine the LO and RF signals, which is bulky for most commercial applications. The second receiver is designed for automotive applications, which require compact, light and low-cost modules. The 140-170 GHz receiver is based on a planar subharmonic Schottky-diode mixer in order to reduce the aperture linear

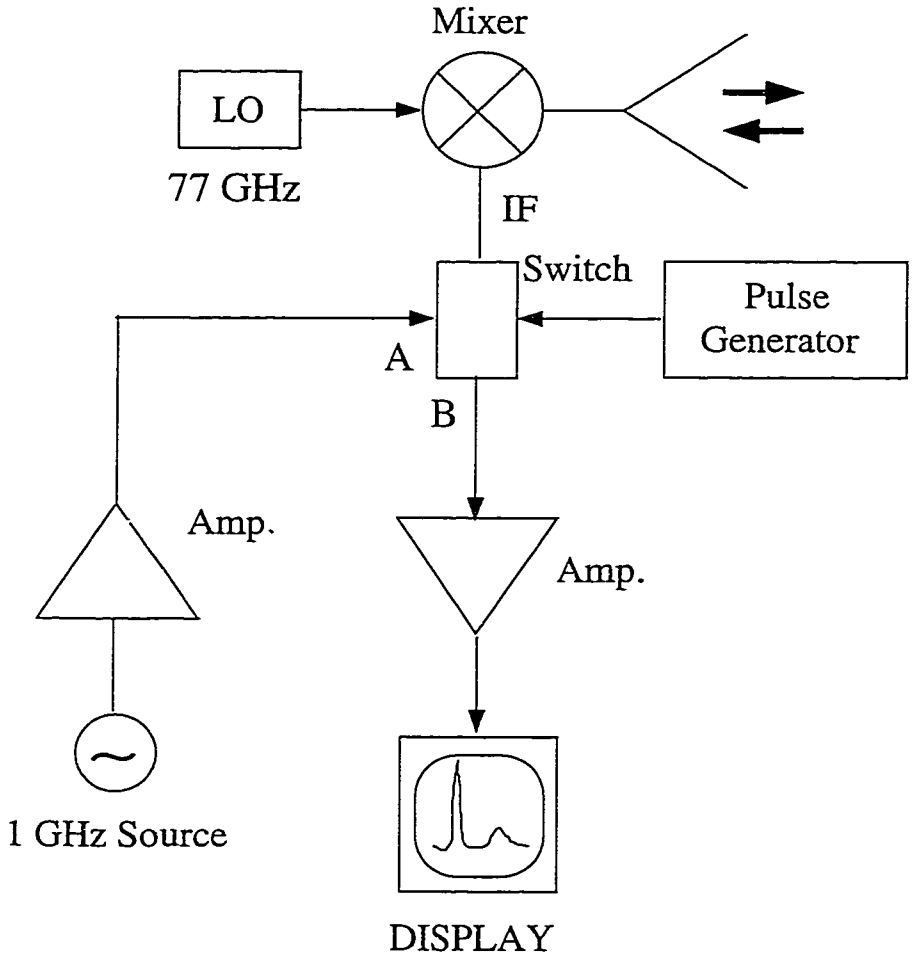

Figure 7.1: Radar configuration.

size by a factor of two. The double folded-slot antenna is used and proves to be particularly well adapted to this receiver due to its low input impedance (20 Ω) which is a good match to the subharmonic diode input impedance (22-j30 Ω). The DFS antenna also allows for RF amplification before downconversion, and for on-wafer LO injection at 70-85 GHz. The receiver shows a measured wideband DSB conversion loss of 11.5-13.5 dB at 140-170 GHz. In both double-slot and double folded-slot receivers, the silicon lens contributes 1.8-2.4 dB of losses in the overall system performance, and can be reduced by 1.0 dB if an optimum matching cap layer is used. These geometries provide low-cost solutions to uniplanar monolithic receivers for future automotive radar applications (Fig. 7.1).

Standard micromachining processes are used in Chapter 3 and 4 to eliminate surface waves triggered by microstrip antennas on thick high dielectric constant substrates. The intent is to synthesize low dielectric constant regions around and underneath the radiating patch antenna. The first approach consists of small closely spaced drilled holes around and below the antenna, and is successfully demonstrated on a 13 GHz microstrip-fed microstrip antenna. The dielectric constant is locally reduced from 10.8 to 2.3, and many improvements are achieved: better radiation patterns, lower cross-polarization levels, increased radiation efficiency, from 61% to 87%, and larger bandwidth, from 0.8% to 7.9%. The second approach is to etch a cavity below the patch antenna on silicon substrates using wet-chemical etching techniques. An aperture-coupled microstrip antenna is realized with a micromachined cavity, reducing the dielectric constant from 11.7 to close to 3.0-3.5. The antenna is integrated with a cpw output port using a low-loss cpw-to-microstrip transition. The radiation efficiency is improved from 28% for an antenna on a non-micromachined silicon substrate to 58% for the micromachined case. This aperture-coupled microstrip

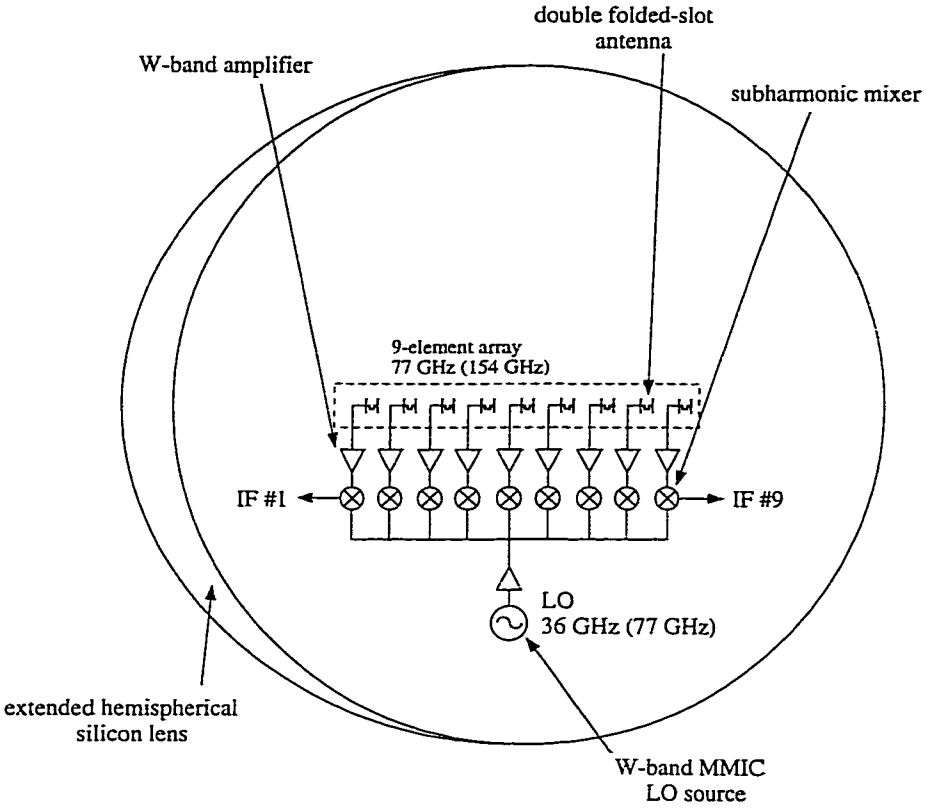

Figure 7.2: Integrated millimeter-wave imaging receiver based on double folded-slot antennas for automotive applications.

antenna has an excellent -10 dB bandwidth (10%), and good radiation patterns with a measured front-to-back ratio of 12 dB. The mutual coupling between adjacent elements in an array configuration is better than -20 dB when individual cavities are etched below each patch antenna.

The third part of this thesis deals with applications such as vertically integrated circuits which require the flexibility to use a combination of planar technologies (microstrip, coplanar strips and waveguides) and which are not dependant on air-bridges and via-holes. Low-loss, wideband and small transitions are therefore necessary to ensure the compatibility of cpw and microstrip technologies. First, a uniplanar cpw-to-microstrip transition centered at 94 GHz is shown. It results in 0.2 dB insertion

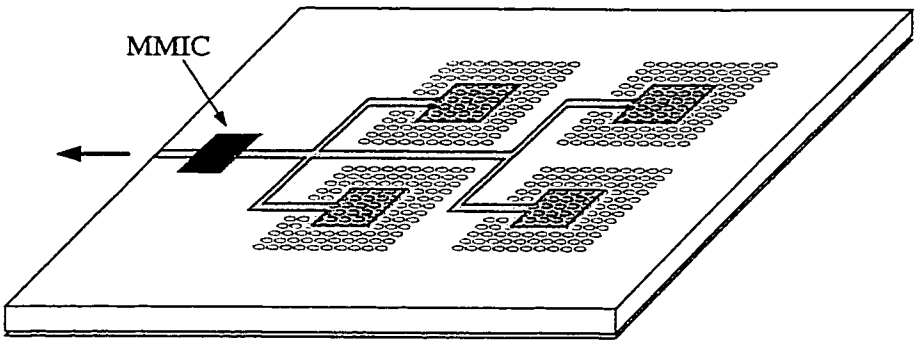

Figure 7.3: Two-by-two 10-40 GHz micromachined phased array.

loss with a bandwidth of 20%. The return loss is better than -17 dB from 85 GHz to 100 GHz. Then, vertical transitions based on surface-to-surface coupling are described. The first transition uses cpw-mode coupling and results in an insertion loss better than 0.6 dB over the whole band, with a loss of 0.25 dB from 85-110 GHz. The return loss is better than -10 dB from 75 to 110 GHz. The second transition uses microstrip-mode coupling and results in a 0.2 dB insertion loss over the whole W-band.

7.2 Future Work

Microwave and millimeter-wave advanced systems architecture is demanding technological improvements in multiple areas: devices, circuits, packaging, antennas, as well as communication systems, control and software. The technologies explored in this thesis provide low-loss and simple solutions to the RF passive aspects of millimeter-wave front-end transceivers and communication modules.

The double folded-slot receiver described in the first part of this thesis can be extended a monopulse radar. The configuration would require 4 double folded-slot antennas and subharmonic mixers, and two LO sources injected with 3-dB hybrid power dividers (Fig. 7.2). W-band MMIC LO sources can be directly directly on the

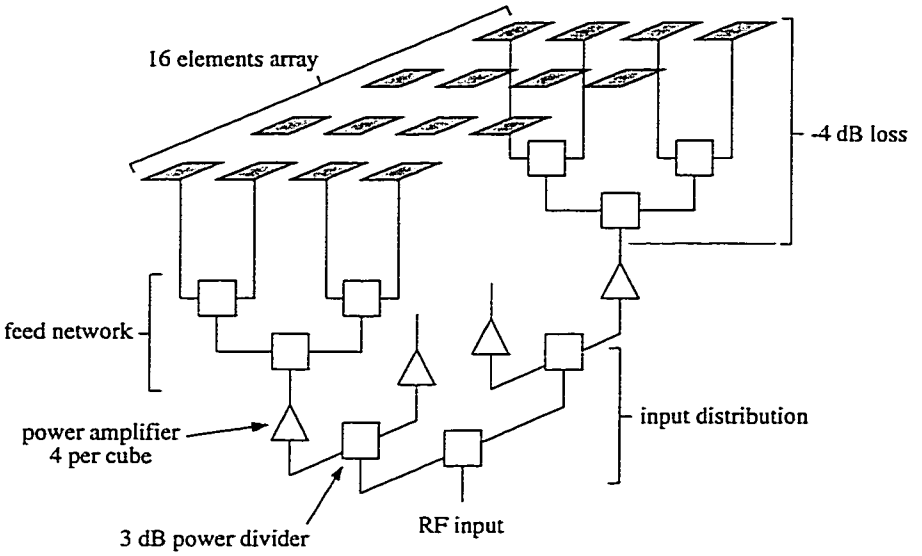

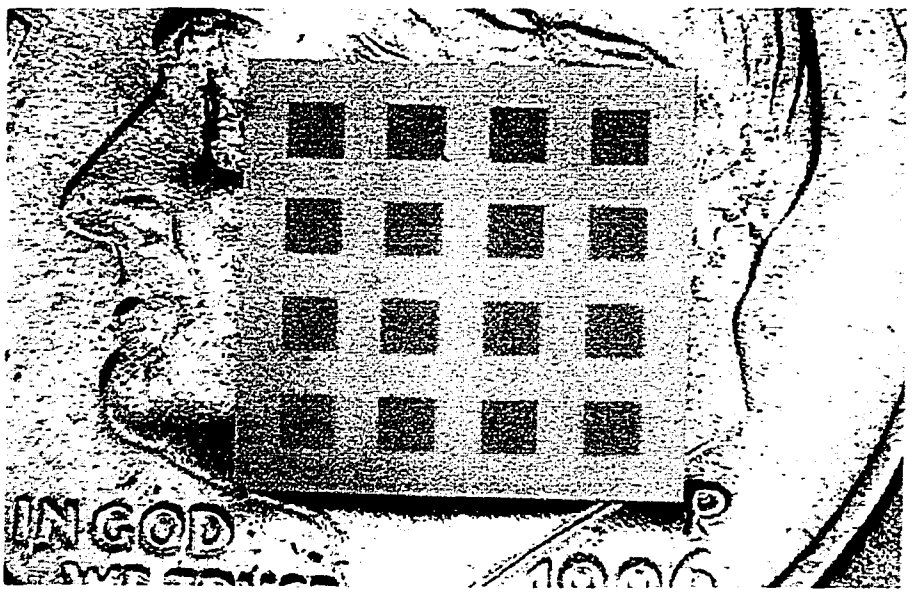

Figure 7.4: Conceptual diagram and picture of the 16 element phased array.

circuit, Monolithic PHEMT oscillators producing 0.3 mW of power at 74-75.5 GHz have been reported [70]. InP-based HBT MMIC oscillators can produce 0.5 mW of power at 77 GHz [71], and single-stage pseudomorphic GaAs HFET oscillators generate 8 mW of power at 75 GHz for a drain bias of V_{DS}=3 V [72]. The off-axis scanning properties of dielectric lens-integrated receivers are also very attractive for many active integrated antennas for wireless applications, which require beam control and beam steering, such as radar based wireless communications. Lens-based receivers are of particular interest for phase conjugate systems and retrodirective reflectors, where the detected wavefront at the antenna array is conjugate phase shifted at each mixer. The IF signal is then reradiated with an inverted phase, therefore preserving the wavefront, even if the antenna array is not planar, or is partly physically blocked.

The micromachined microstrip antennas presented in this thesis can be integrated in compact, high-efficiency, multi-function front-end transceivers. It is possible to build millimeter-wave 10-40 GHz phased and imaging arrays on silicon or GaAs substrates using the drilled-holes technique A 2×2 phased array in shown in Figure 7.3. The holes are drilled or chemically etched around and underneath each of the four patch antennas forming the array. The RF circuits, feed networks with power dividers, in-line matching sections, phase shifters and high-Q filters, are fabricated on the high-dielectric constant substrate. Wire-bond or flip-chip MMIC devices are then mounted at the output port of the array. Besides, such a geometry permits the monolithic integration of MMIC devices on the same substrate.

High-efficiency micromachined microstrip antennas can also be combined with the low-loss wideband transitions described in this thesis, to fabricate fully integrated three-dimensional millimeter-wave sensor modules. With the use of on-wafer pack-

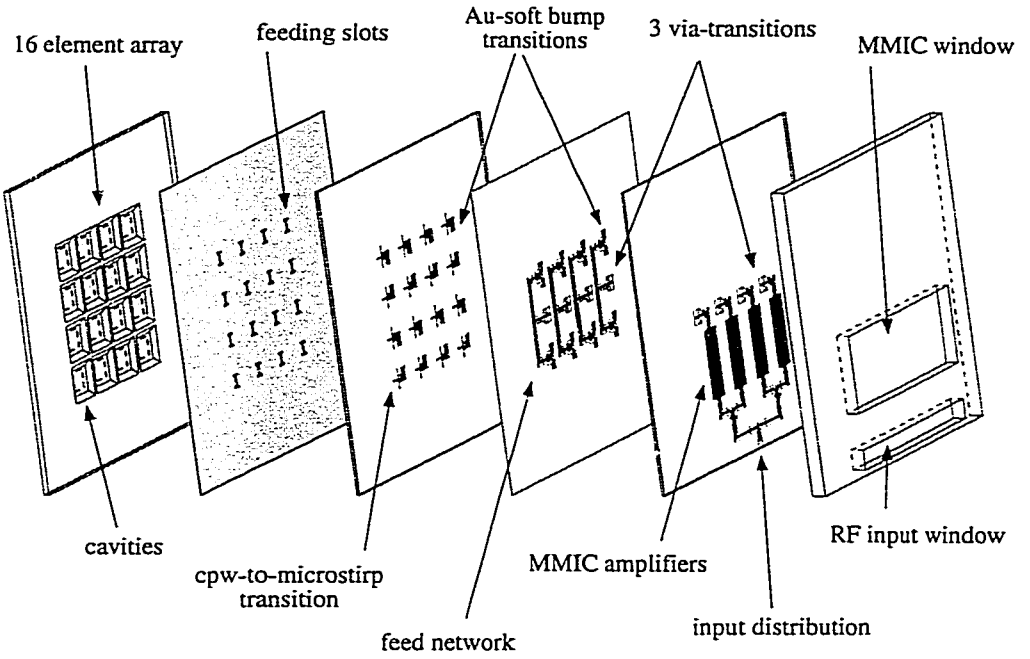

(a)

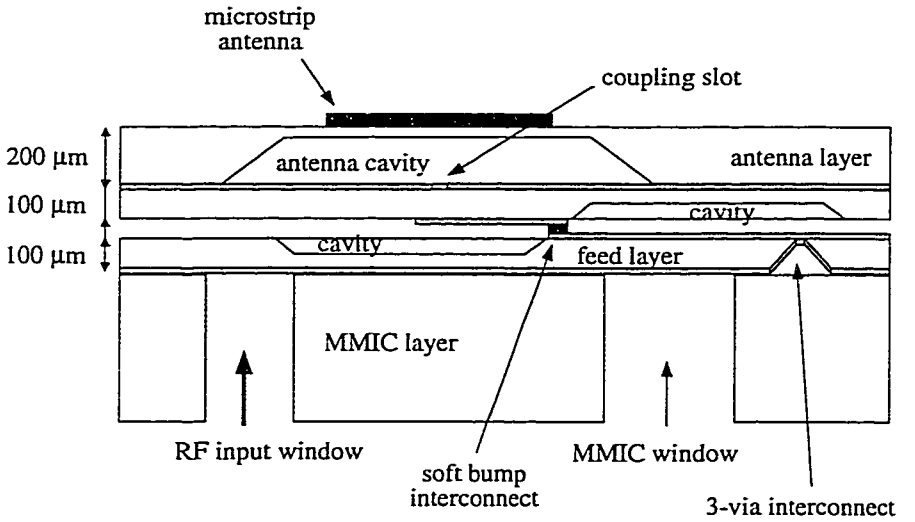

(b)

Figure 7.5: Perspective view (a) and cross-section (c) of the 94 GHz power cube.

aging, a high-density vertical integration can be achieved. Figure 7.4 shows a 4×4 hybrid monolithic phased array designed for radar guidance systems operating at 94 GHz. The goal is to implement a high efficiency array in a high-density building block, which can generate close to 2 Watts/in^2 in a 0.007 in^3 silicon micropackage. Also, low-cost fabrication and assembly processes are used. The W-band power cube consists of 4 layers. Aperture-coupled microstrip antennas form the antenna layer. The silicon substrate is 200 μm thick and is micromachined using the method described in Chapter 5 to result in high radiation efficiency (60%) and low cross-talk (-20 dB) between elements. The antenna feed networks lie on a 100 μm thick silicon substrate. The ground plane parasitic effects are taken into account in order to tune the power divider amplitude and phase balance. Four flipped InP MMIC power amplifiers with 10 dB of gain and 50 mW of output power are mounted in one cube. The placement of the MMIC amplifiers has to be very accurate and reliable. The input distribution network (Fig 7.5) is also integrated before RF amplification. Interlayer transitions rely on pressure contacts through gold soft bumps. The RF radiation and interconnect losses are reduced as low as possible with the use of shielded fgc lines. The silicon substrates supporting the fgc lines and feed networks are etched to provide line shielding as well as feature placement (such as the soft bump transitions). The total RF losses are expected to be less than 4 dB between the microstrip antennas and the power amplifiers, including antenna radiation efficiency. The power cube is currently undergoing fabrication and testing.

APPENDICES

APPENDIX A

77 GHz DUAL-POLARIZED MICROSTRIP ANTENNAS ON THIN DIELECTRIC MEMBRANES

Automotive collision avoidance systems are currently being fabricated and field-tested at 76-78 GHz [73, 74]. The systems are typically composed of a transmitter/low-noise receiver front-end placed at the focal plane of a 10 to 15 cm dielectric collimating lens. A waveguide horn antenna or a microstrip antenna is commonly used as the feed antenna at the focal plane. The microstrip antenna is typically etched on a 80-100 μm thick teflon substrate and is not compatible with MMIC front-end electronics.

Part of this thesis deals with the elimination of dielectric losses and surface waves suffered by microstrip antennas on high-ϵ_r substrates: the approach consists in synthesizing local low-ϵ_r regions around the patch, by ever drilling small closely spaced holes (Chapter 4) or etching a cavity nelow the antenna (Chapter 5). The bandwidth, radiation efficiency and patterns are significantly improved. The other approach considered and described in this appendix is to suspend the antenna on a thin dielectric membrane deposited directly on the silicon substrate. This technique has been developped by Rebeiz et al. for high-efficiency millimeter-wave antennas [34, 75], and recently applied to microstrip antennas at 77 GHz by Stotz et al. [43]. Single and

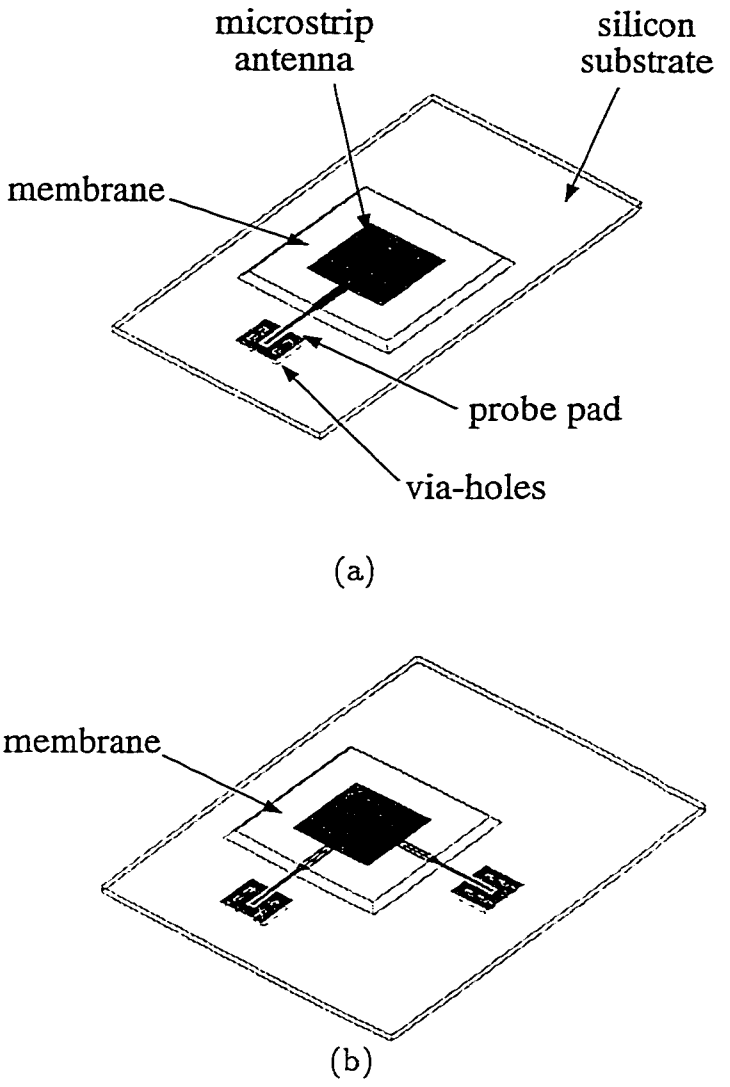

Figure A.1: Perspective view of the single- (a) and dual-polarized (b) microstrip antenna on membranes.

dual-polarized microstrip antennas suspended on thin-film membranes are designed, fabricated and tested at 77 GHz for automotive applications. The goal is to increase the bandwidth and the isolation between the orthogonal ports while using standard integration of GaAs or Silicon microchip-based MMICs.

A.1 Antennas on thin dielectric membranes

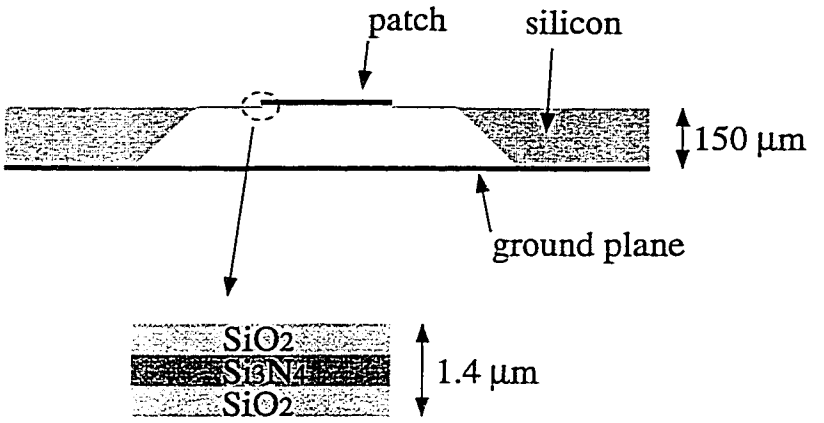

Figure A.2: Cross-section and detail of the thin-film membrane.

Integrated circuits on thin film membranes, therefore suspended in free-space, are low-loss since they are not disturbed by the presence of a dielectric substrate directly below the radiating element. The radiation characteristics of antennas integrated on thin dielectric membranes are therefore vastly improved. Figure A.1 shows a perspective view of single- and dual-polarized microstrip antennas on membranes. The membrane is a composite of three dielectric layers deposited by thermal oxydation and low-pressure chemical vapor deposition: $SiO_2/Si_3N_4/SiO_2$ (Fig. A.2), on both sides of a silicon substrate. The total thickness is 1.4 μm for an effective dielectric constant close to ϵ_m=5. The silicon substrate is removed from the backside with wet-chemical etching techniques described previously, such as TMAH or KOH. The three-layer structure gives the membrane strong mechanical properties with a residual tensile stress of 5-20 MPa, and can be used in MMIC applications.

A.2 Input Impedance Measurements

A.2.1 Antenna Design

The layout of the dual-polarized microstrip antenna is shown in Figure A.3. The substrate is 150 μm-thick silicon ($\epsilon_r = 11.7$). This corresponds to $0.13\lambda_d$ at 77 GHz,

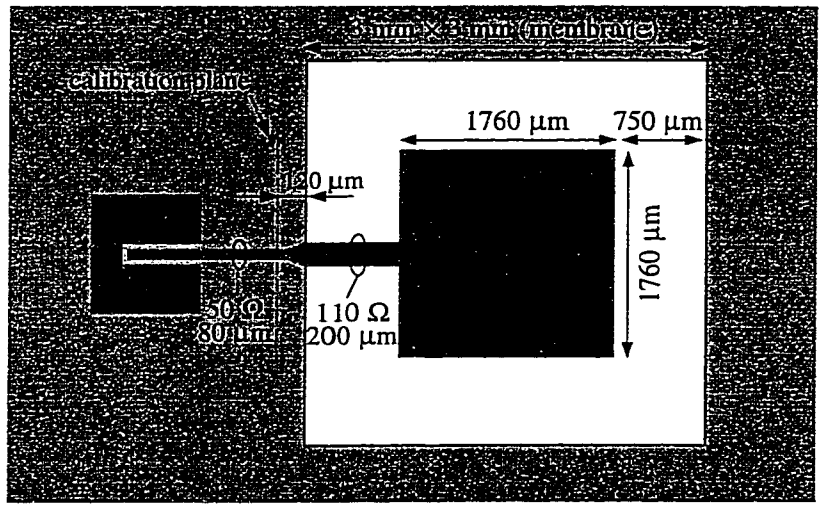

(a)

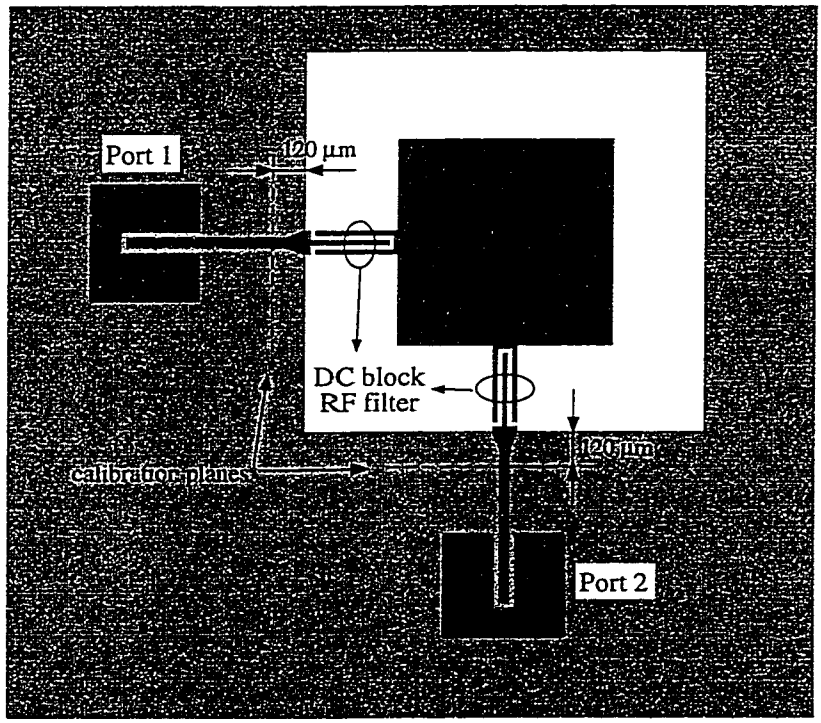

(b)

Figure A.3: Lay-out of the single- (a) and dual-polarized (b) microstrip antenna used for input impedance measurements.

but only $0.04\lambda_0$, where λ_0 and λ_d are the free-space and dielectric wavelengths, respectively. The single-polarized antenna is integrated on a 3×3 mm membrane and is fed by a microstrip line on the membrane (Fig. A.3(a)). The antenna dimensions are 1760 μm-square which is slightly larger than the resonant dimensions, and a 110 Ω-line, 0.19 λ_{guide} long is used to transfer the input impedance to 50 Ω at the membrane-silicon interface. The 110 Ω line on the membrane transforms into a 50 Ω-line on the high-resistivity silicon substrate. The dual-polarized antenna is also built on a 3×3 mm membrane and is fed by two orthogonal ports (Fig. A.3(b)). The input impedance and isolation is calculated with a method-of-moment solution [59]. The resonant impedance is 340 Ω for an antenna dimension of 1760 μm-square, and the corresponding isolation between the orthogonal ports is calculated to be better than 20 dB over a 20 GHz (26%) bandwidth. The solution takes into effect the width of the feeding lines but assumes that the antenna is integrated on a infinite dielectric membrane. The effective dielectric constant is taken to be 1.05 which is the quasi-static average between the 1.5 μm thick membrane layer ($\epsilon_r = 5$) and the 150 μm thick air ($\epsilon_r = 1$). Microwave modeling at 3.5 GHz has shown that the silicon-membrane interface wall has no effect on the radiation patterns and input impedance if placed as close as 4h to the edge of the microstrip antenna, where h is the thickness of the silicon substrate.

A.2.2 W-band Measurements

The antenna was fabricated on a 150 μm thick high-resistivity silicon substrate, and 9000 Å gold was used for metalization. Figure A.4 shows a picture of the fabricated dual-polarized microstrip antenna. The edge of the membrane is not very well defined due to some misalignment with the $< 100 >$ crystal planes. The input

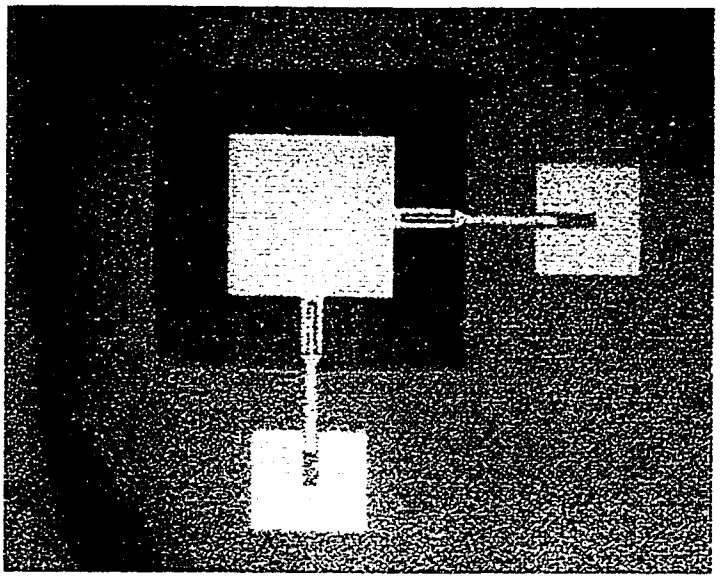

Figure A.4: Picture of the 77 GHz dual-polarized microstrip antenna.

impedance of the single- and dual-polarized antennas is measured with a network analyzer HP8510 using W-band probes, and is compared to the method-of-moment simulations (Fig. A.5). The VNA is calibrated with the TRL technique, and the calibration plane is 120 μm before the membrane edge (Fig. A.3). The measured input impedance is 26 Ω at 76 GHz (-10 dB return loss), compared to the simulated 45 Ω at 76 GHz (-20 dB return loss). The measured port-to-port isolation is -20 dB over a 8 GHz bandwidth. The difference is mainly due to the use of cpw-probe pads where the cpw grounds are connected to the microstrip gound plane with silver epoxy-filled viaholes. This transition has not been optimized and is introducing calibration errors. A more reliable cpw-to-microstrip transition based on electromagnetic coupling should be used in future designs (Chapter 6).

A.3 Radiation Performances

A.3.1 Design for Radiation Patterns Measurements

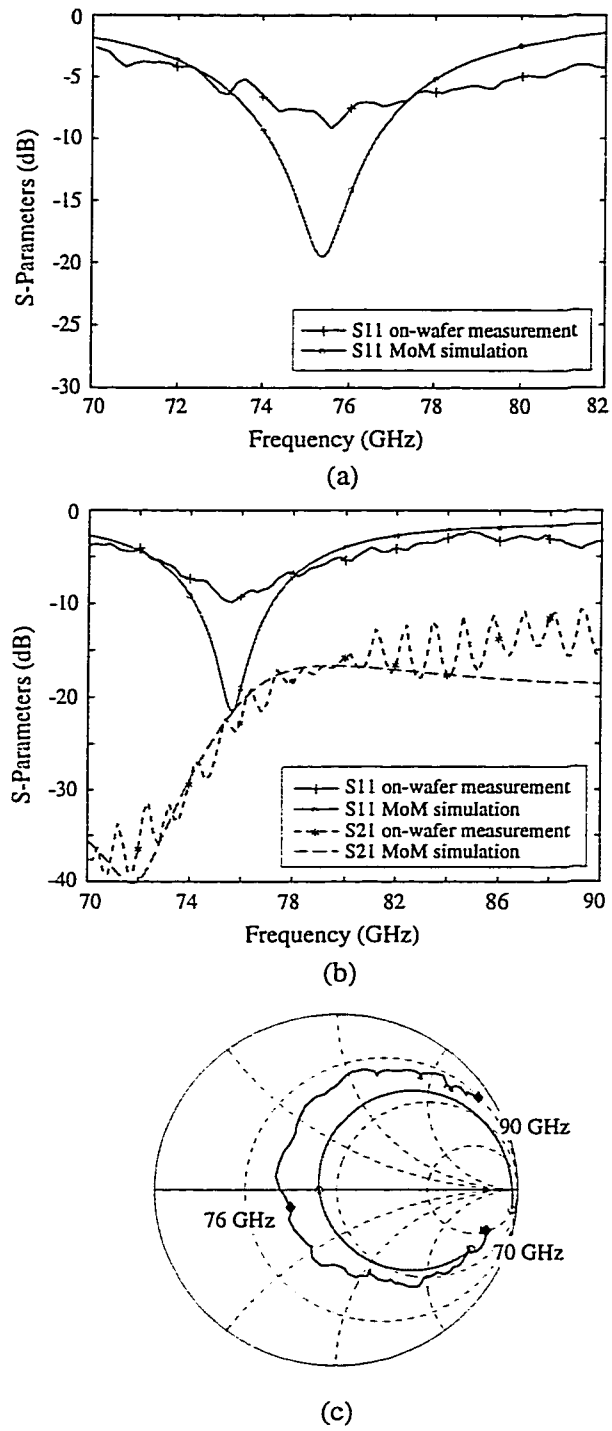

Figure A.5: Measured and calculated input impedance of the single- (a) and isolation of the dual-polarized (b,c) microstrip antenna at 70-90 GHz.

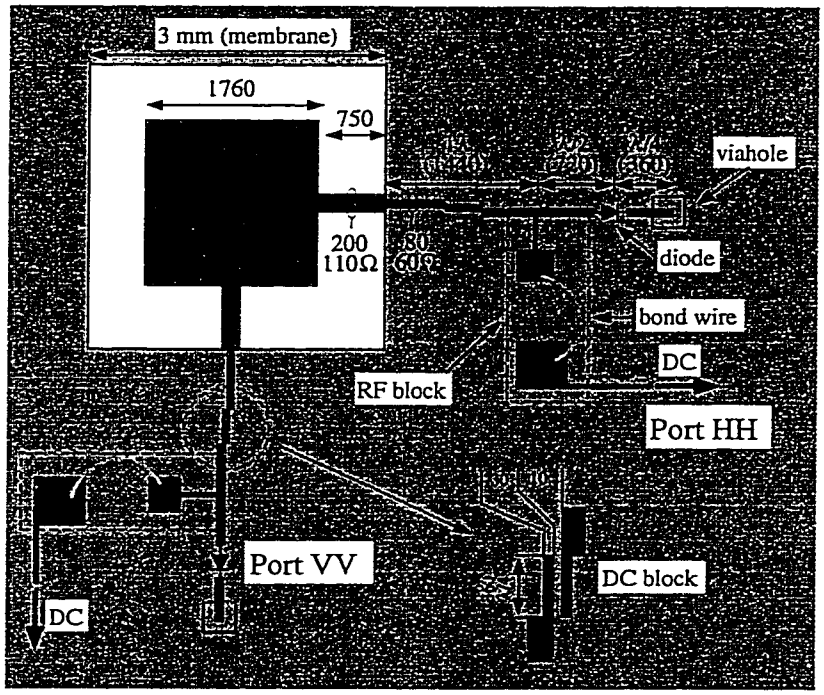

Figure A.6: Lay-out of the dual-polarized microstrip antenna used for radiation patterns measurements.

The design used to measure the radiation patterns and polarimetric isolation between the two ports of the dual-polarized microstrip antenna is the same as the design used to measure the input impedance. The feed lines are slightly modified to integrate a detector (Fig. A.6). The antenna is suspended on a membrane over a 150 μm-thick silicon substrate and is 1760 μm long and fed by a 110 Ω 750 μm-long microstrip line lying on the membrane, transforming into a 60 Ω microstrip line on silicon. A Schottky-diode detector (ALPHA DMK2784) is placed $1.5\lambda_g$ away from the silicon-membrane interface and the bias/low-frequency (1 kHz) detected voltage is fed/removed using a low-pass impedance network. The diode is connected to the ground plane with a via-hole, which is etched at the same time as membrane formation. The diodes were silver epoxied using Epo-Tek H20E and were biased at 50 μA. The diodes are DC isolated from each other with a $\lambda/4$ coupled-line filter. For

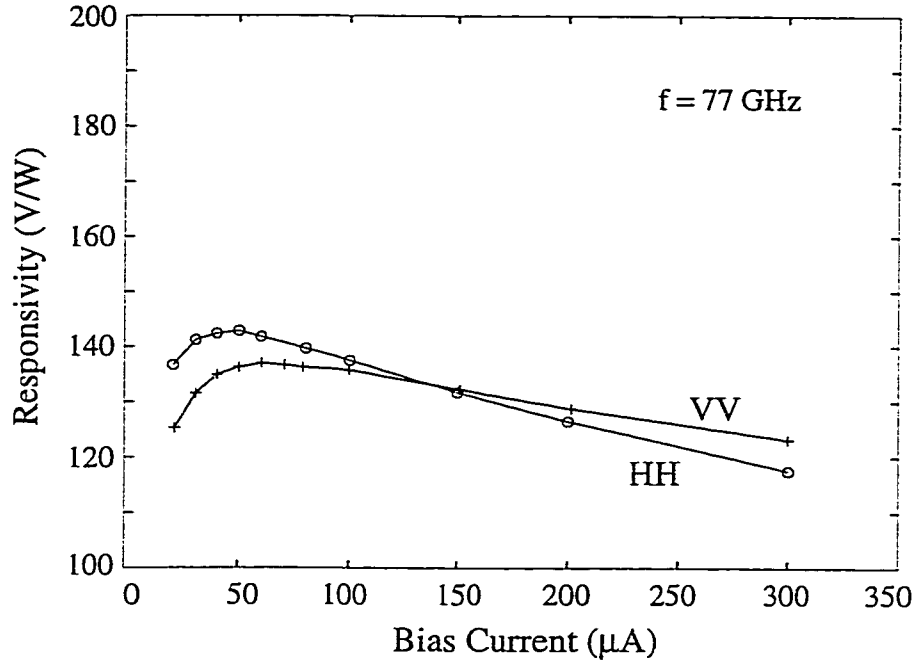

(a)

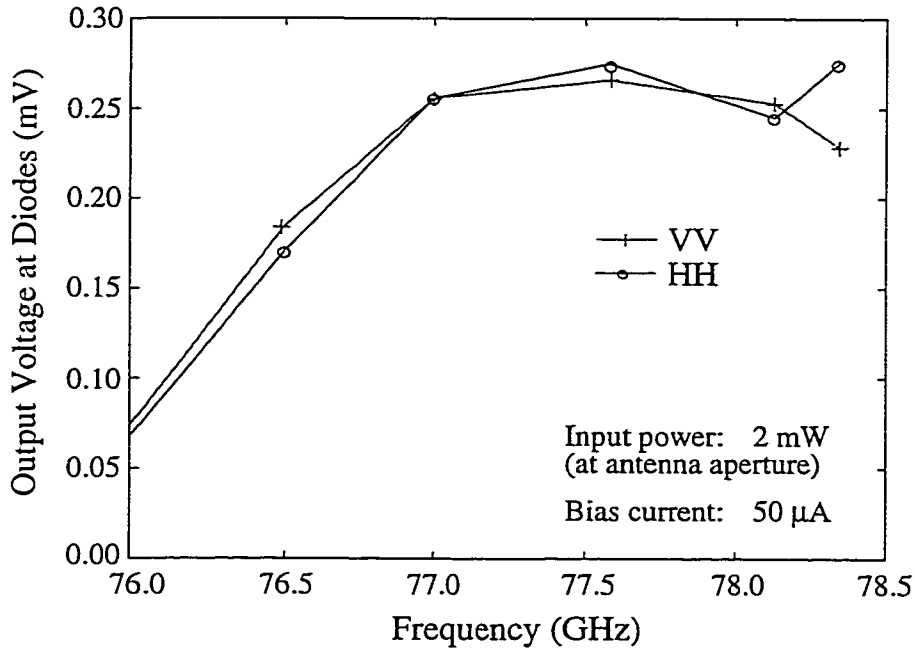

(b)

Figure A.7: Video responsivity of the Schottky diodes at 77 GHz (a) and measured peak power versus frequency (b).

convenience, the "horizontal" and "vertical" ports are called HH-port and VV-port, respectively (Fig. A.6).

A.3.2 Video Responsivity

The HH- and VV-diodes are characterized and compared as video detectors. The video responsivity is defined as the measured low frequency voltage in a 120 $k\Omega$ load divided by the total 77 GHz RF power incident on the antenna aperture. The measurement set-up in described in more details in Chapter 2. The video responsivity (Fig. A.7(a)) and received peak power versus frequency (Fig. A.7(b)) are measured. The maximum responsivity is obtained for a bias current of 50 μA for both diodes, and the maximum power received is the same for both diodes at 76-78 GHz. The diodes are therefore well balanced.

A.3.3 Polarimetric Isolation and Radiation Patterns

The diodes are biased for maximum detection (I_{bias}=50 μA) to measure the polarimetric isolation and the radiation patterns. The measured polarimetric isolation versus Φ-angle in the plane of the antenna is shown in Figure A.8. It is seen that the HH-port isolation at 76-78 GHz is -18 dB at 90^0 and dips to -20/-25 dB at 100^0 (Fig. A.8(a)). Similar result is noticed at the VV-port (Fig. A.8(b)). This is due to interference from the feeding transmission lines. This can be clearly seen on the measured E-plane patterns at 78 GHz (Figure A.9) for both ports. The H-plane, in contrast, does not suffer from feed line interference. This can be explained by radiation from feeding microstrip lines which are on a 150 μm thick silicon substrate ($0.13\lambda_d$ thick at 77 GHz) and couple quite a bit of power to the TM_0 mode.

A.4 Conclusion

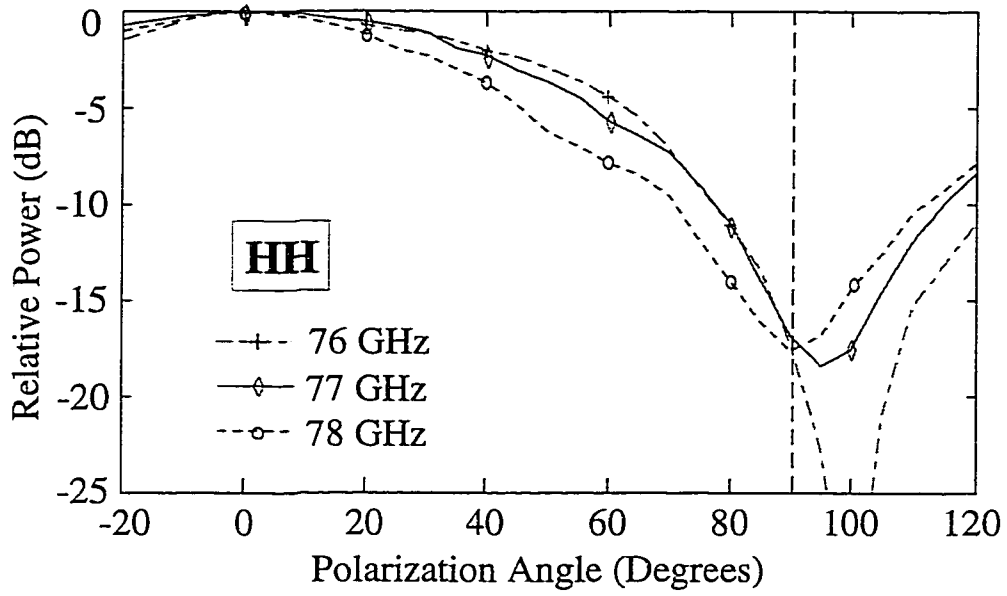

(a)

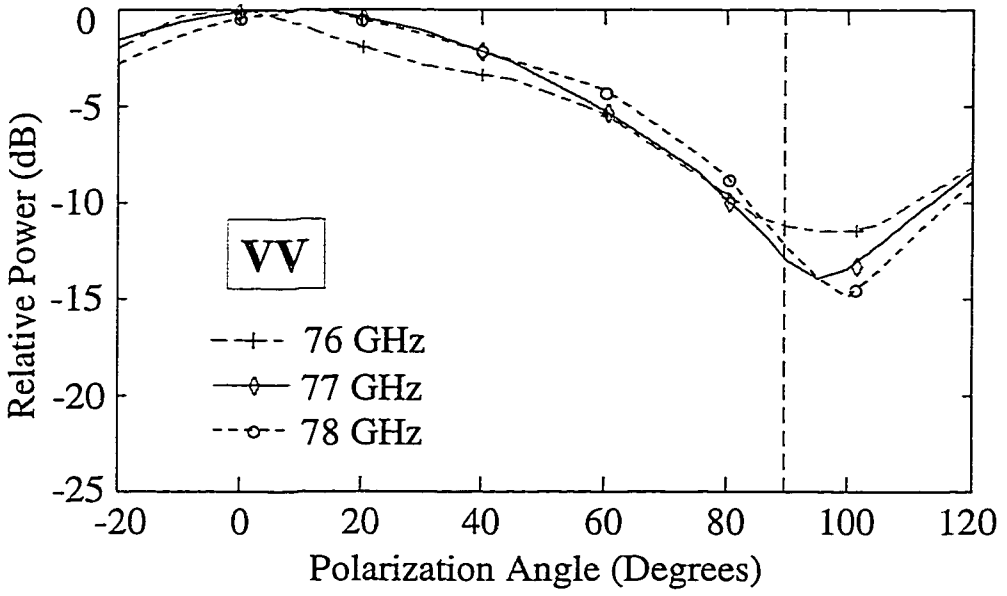

(b)

Figure A.8: Measured polarization sensitivity for both HH- and VV-ports at 76-78 GHz.

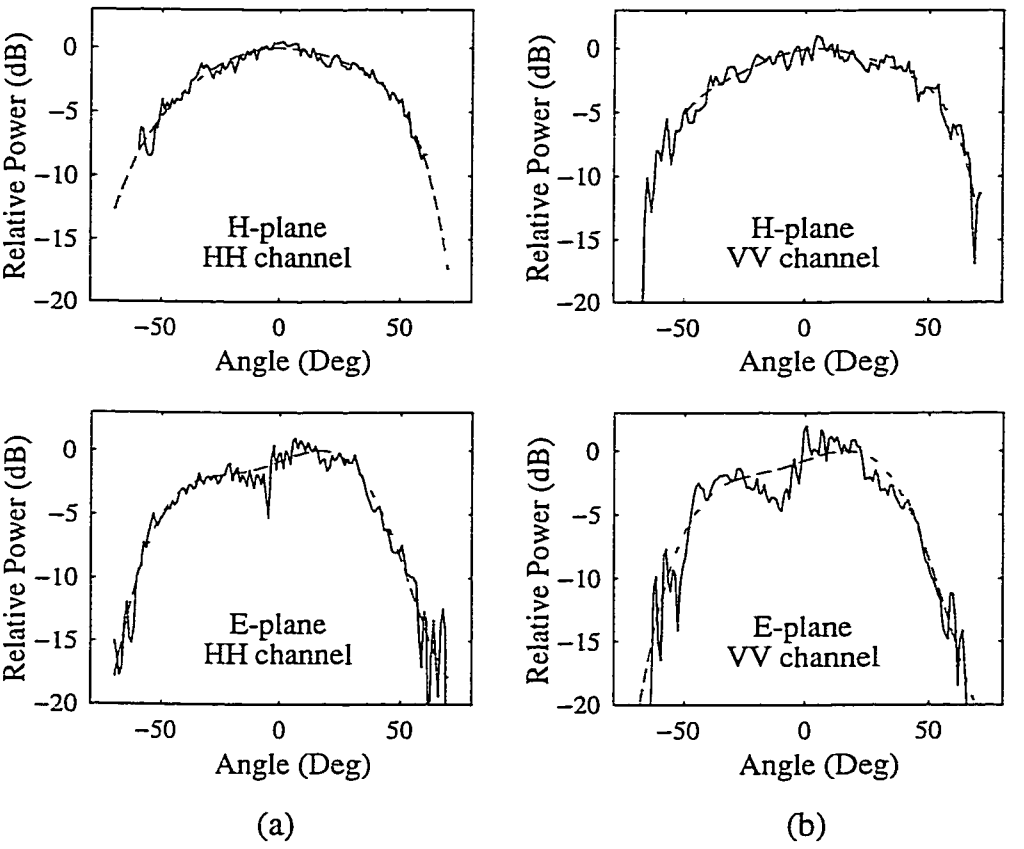

Figure A.9: Measured E-plane and H-plane patterns for both HH- and VV-ports at 78 GHz.

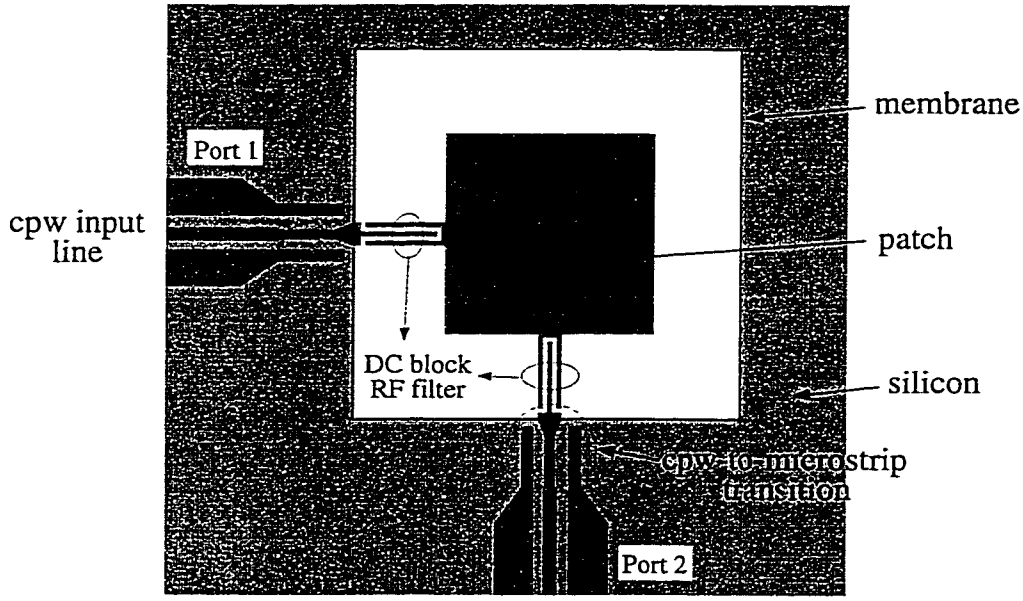

Figure A.10: Uniplanar cpw-fed microstrip antenna on membrane.

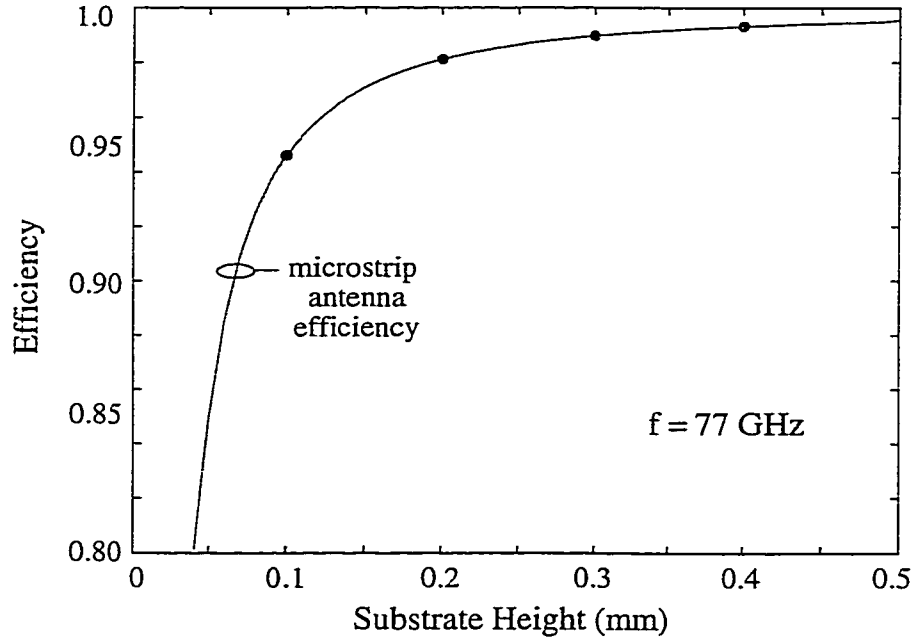

Figure A.11: Calculated radiation efficiency of a patch antenna and of an ideal dipole on a thin-film membrane ($\epsilon_r = 1.05$ substrate) versus substrate thickness at 77 GHz.

Single- and dual-polarized microstrip antennas suspended on thin dielectric membranes have been designed at 77 GHz for automotive applications. The measurements indicate a comfortable 2 GHz bandwidth, with a -18 dB isolation between the orthogonal ports. The measured co-polarization power versus frequency is constant to ± 1 dB over the 75-78 GHz range indicating relatively wideband operation of the membrane suspended antenna.

The performance of the antenna was limited by the feed-line radiation interference and future designs should correct this problem. This can be done by replacing the microstrip lines on silicon by finite ground coplanar waveguides (fgc), and using a wideband low-loss cpw-to-microstrip transition (Chapter 6) at the silicon/air interface (Fig. A.10). This solution results in a uniplanar design where the input ports are cpw-line, and the radiating elements are microstrip antennas. Another advantage is that thicker substrates can be used in order to optimize the microstrip antenna radiation efficiency. The radiation efficiency of a patch antenna on $\epsilon_r = 1.05$ substrates is close to a maximum for a substrate thickness of 300 μm, based on the quality factor calculation described in Chapter 4 (Fig. A.11). However, the model used to calculate the radiated and surface-wave powers is not very accurate at millimeter-wave frequencies, and is only useful for a quick estimate. Slot-fed designs also minimize feed line radiation problems as demonstrated in Chapter 5, since the feed lines are isolated from the patch antenna by a ground plane. This geometry was shown by Stotz *et al.* in a 3×1 aperture-coupled patch antenna array [43].

BIBLIOGRAPHY

BIBLIOGRAPHY

[1] W.H. Haydl, W. Heinrich, R. Bosch, M. Schlechtweg, P. Tasker, and J. Braunstein, "Design data for millimeter-wave coplanar circuits," *European Microwave Conf. Proc.*, pp. 223–228, 1993.

[2] M. Riaziat, R. Majidi-Ahy, and I. Feng, "Propagation modes and dispersion characteristics of coplanar waveguides," *IEEE Trans. on Microwave Theory Tech.*, vol. 38, no. 3, pp. 245–251, Mar. 1990.

[3] F. Brauchler, S.V. Robertson, J. East, and L.P.B. Katehi, "W-band finite ground coplanar (fgc) line circuit elements," *IEEE-MTT Int. Microwave Symp. Digest*, pp. 1845–1848, 1996.

[4] C. Zah, R.C. Compton, and D.R. Rutledge, "Efficiencies of elementary integrated-circuit feed antennas," *Electromagnetics*, vol. 3, pp. 239–254, 1983.

[5] D.M. Pozar, "Considerations for millimeter wave printed antennas," *IEEE Trans. on Antennas Propagat.*, vol. 31, no. 9, pp. 740–747, Sep. 1983.

[6] D.R. Jackson and N.G. Alexopoulos, "Microstrip dipoles on electrically thick substrates," *Int. J. Infrared and Millimeter Waves*, vol. 7, no. 1, pp. 1–26, Jan. 1987.

[7] D.B. Rutledge, D.P. Neikirk, and D.P. Kasilingam, *Infrared and Millimeter-Waves*, vol. 10, Academic Press, New York, 1983, Integrated-circuit antennas.

[8] G.M. Rebeiz, "Millimeter-wave and terahertz integrated circuit antenna," *Proceedings of the IEEE*, vol. 80, no. 11, pp. 1748–1770, Nov. 1992.

[9] H.J. Siweris, A. Werthof, H. Tischer, U. Schaper, A. Schäfer, L. Verweyen, T. Grave, G. Bock, M. Schlechtweg, and W. Kellner, "Low cost GaAs PHEMT MMICs for millimeter-wave sensor applications," *IEEE-MTT Int. Microwave Symp. Digest*, pp. 243–246, 1998.

[10] L. Verweyen, A. Bangert, H. Massler, T. Fink, M. Neumann, R. Osorio, T. Krems, T. Jakobus, W.H. Haydl, and M. Schlechtweg, "Compact integrated coplanar T/R-modules for automotive applications," *IEEE-MTT Int. Microwave Symp. Digest*, pp. 243–246, 1998.

[11] D. Ferling, M. Florjancic, A. Gutu-Nelle, H. Richter, W. Heinrich, F.J. Schmückle, and M. Schlechtweg, "Coplanar high gain millimeter wave amplifier module," *European Microwave Conf. Proc.*, pp. 206–211, 1998.

[12] M. Born and E. Wolf, *Principles of Optics*, Permagon Press, New York, 1959.

[13] D.B. Rutledge and M.S. Muha, "Imaging antenna arrays," *IEEE Trans. on Antennas Propagat.*, vol. 30, no. 4, pp. 535–540, Jul. 1982.

[14] T.H. Büttgenbach, "An improved solution for integrated array optics in quasi-optical mm and submm receivers: the hybrid antenna," *IEEE Trans. on Microwave Theory Tech.*, vol. 41, no. 10, pp. 1750–1761, Oct. 1993.

[15] D.F. Filipovic and G.M. Rebeiz, "Double-slot antennas on extended hemispherical and elliptical quartz dielectric lenses," *Int. J. Infrared and Millimeter Waves*, vol. 14, no. 10, pp. 1905–1924, Oct. 1993.

[16] D.F. Filipovic, S.S. Gearhart, and G.M. Rebeiz, "Double-slot antennas on extended hemispherical and elliptical silicon dielectric lenses," *IEEE Trans. on Microwave Theory Tech.*, vol. 41, no. 10, pp. 1738–1749, Oct. 1993.

[17] D.F. Filipovic, G.P. Gauthier, S. Raman, and G.M. Rebeiz, "Off-axis properties of silicon and quartz dielectric lens antennas," *IEEE Trans. on Antennas Propagat.*, vol. 45, no. 5, pp. 760–766, May 1997.

[18] D.F. Filipovic, *Analysis and design of dielectric-lens antennas and planar multiplier circuits for millimeter-wave applications*, Ph.D. thesis, Univ. of Michigan, 1995.

[19] C. Zah and D.R. Rutledge, "A polystyrene cap for matching a silicon lens at millimeter wavelengths," *Int. J. Infrared and Millimeter Waves*, vol. 6, no. 9, pp. 909–917, Sep. 1985.

[20] S. Raman and G.M. Rebeiz, "Single- and dual-polarized millimeter-wave slot-ring antennas," *IEEE Trans. on Antennas Propagat.*, vol. 44, no. 11, pp. 1438–1444, Nov. 1996.

[21] S. Raman, S. Barker, and G.M. Rebeiz, "A W-band dielectric-lens-based integrated monopulse radar receiver," *IEEE-MTT Int. Microwave Symp. Digest*, pp. 517–520, 1998.

[22] I.J. Bahl and P. Bhartia, *Microstrip Antennas*, Artech House, Dedham, MA, 1982.

[23] A.R. Kerr, P.H. Siegel, and R.J. Mattauch, "A simple quasi-optical mixer for 100-120 GHz," *IEEE-MTT Int. Microwave Symp. Digest*, pp. 96–98, 1977.

[24] J. Zmuidzinas and H.G. LeDuc, "Quasi-optical slot antenna SIS mixers," *IEEE Trans. on Microwave Theory Tech.*, vol. 40, no. 9, pp. 1797–1804, Sept. 1992.

[25] R.L. Rogers and D.P. Neikirk, "Radiation properties of slot and dipole elements on layered substrates," *Int. J. Infrared and Millimeter Waves*, vol. 10, no. 10, pp. 697–728, Oct. 1989.

[26] S.M. Wentworth, R.L. Rogers, J.G. Hestona, D.P. Neikirk, and T. Itoh, "Millimeter wave twin slot antennas on layered substrates," *Int. J. Infrared and Millimeter Waves*, vol. 11, no. 2, pp. 111–131, Feb. 1990.

[27] G. Eleftheriades and G.M. Rebeiz, "Self and mutual impedance of slot antennas on a dielectric half-space," *Int. J. Infrared and Millimeter Waves*, vol. 14, no. 10, pp. 1925–1946, Oct. 1993.

[28] D.N. Held and A.R. Kerr, "Conversion loss and noise of microwave and millimeter-wave mixers: Part I-Theory," *IEEE Trans. on Microwave Theory Tech.*, vol. 26, no. 2, pp. 49–54, Feb. 1978.

[29] Stycast is a trademark of Emerson and Cummings Inc., Canton, MA.

[30] Diode Mixer Analysis Program provided by Prof. S.A. Maas, Private Consultant.

[31] HP-EEsof Inc. Westlake Village, CA.

[32] Duroid is a trademark of the Rogers Corporation, Chandler, AZ.

[33] S.S. Gearhart and G.M. Rebeiz, "A monolithic 250 GHz Schottky-diode receiver," *IEEE Trans. on Microwave Theory Tech.*, vol. 42, no. 12, pp. 2504–2511, Dec. 1994.

[34] W.Y. Ali-Ahmad and G.M. Rebeiz, "An 86-106 GHz quasi-integrated low-noise Schottky receiver," *IEEE Trans. on Microwave Theory Tech.*, vol. 41, no. 4, pp. 558–564, Apr. 1993.

[35] T.M. Weller, L.P.B. Katehi, and G.M. Rebeiz, "Single and double folded-slot antennas on semi-infinite substrates," *IEEE Trans. on Antennas Propagat.*, vol. 43, no. 12, pp. 1423–1428, Dec. 1995.

[36] S.M. Mollenkopf, L.P.B. Katehi, and G.M. Rebeiz, "A low-cost 20-22 GHz MIC active receiver/radiometer," *IEEE Trans. on Microwave Theory Tech.*, vol. 43, no. 4, pp. 989–993, Apr. 1995.

[37] T.M. Weller, L.P.B. Katehi, and G.M. Rebeiz, "A 250-GHz microshield bandpass filter," *IEEE Microwave and Guided Wave Letters*, vol. 5, no. 5, pp. 153–155, May 1995.

[38] R.B. Marks and D.F. Williams, "A general waveguide circuit theory," *J. of Research of the National Institute of Standards and Technology*, vol. 97, pp. 533–562, Sep./Oct. 1992.

[39] S. Raman, *An integrated millimeter-wave monopulse radar receiver with polarimetric capabilities*, Ph.D. thesis, Univ. of Michigan, 1998, Appendix B, pp. 160-168.

[40] Janos Technology Inc., Box 25, Route 35, Townshend, VT 05353.

[41] M.N. Afsar and K.J. Button, "Millimeter-wave dielectric measurement of materials," *Proceedings of the IEEE*, vol. 73, no. 1, pp. 131–153, Jan. 1985.

[42] D.R. Jackson, J.T. Williams, A.K. Bhattacharyya, R.L. Smith, S.J. Buchheit, and S.A. Long, "Microstrip patch designs that do not excite surface waves," *IEEE Trans. on Antennas Propagat.*, vol. 41, no. 8, pp. 1026–1037, Aug. 1993.

[43] M. Stotz, G. Gottwald, H. Haspeklo, and J. Wenger, "Planar millimeter-wave antennas using SiNx-membranes on GaAs," *IEEE Trans. on Microwave Theory Tech.*, vol. 44, no. 9, pp. 1593–1595, Sept. 1996.

[44] R.F. Drayton, *The development and characterization of self-packages using micromachining techniques for high frequency circuit applications*, Ph.D. thesis, Univ. of Michigan, 1995, Chapter 5, pp. 102-123.

[45] G. Eleftheriades, *Analysis and design of integrated-circuit horn antennas for millimeter and submillimeter-wave applications*, Ph.D. thesis, Univ. of Michigan, 1993, Chapter 7, pp. 151-178.

[46] M.J. Vaughan, K.Y. Hur, and R.C. Compton, "Improvement of microstrip patch antenna radiation patterns," *IEEE Trans. on Antennas Propagat.*, vol. 42, no. 6, pp. 882–885, June 1994.

[47] D.M. Pozar and B. Kaufman, "Comparison of three methods for the measurement of printed antenna efficiency," *IEEE Trans. on Antennas Propagat.*, vol. 36, no. 1, pp. 136–139, Jan. 1988.

[48] PCAAD *Personal Computer Aided Antenna Design*, Version 2.1.

[49] D.M. Pozar and S.D. Targonski, "Improved coupling for aperture coupled microstrip antennas," *Electron. Letters*, vol. 27, no. 13, pp. 1129–1131, June 1991.

[50] E. Belohoubek and E. Denlinger, "Loss considerations for microstrip resonators," *IEEE Trans. on Microwave Theory Tech.*, vol. 23, no. 6, pp. 522–526, June 1975.

[51] D.R. Jackson and N.G. Alexopoulos, "Simple approximate formulas for input resistance, bandwidth, and efficiency of a resonant rectangular patch," *IEEE Trans. on Antennas Propagat.*, vol. 39, no. 3, pp. 407–410, Mar. 1991.

[52] L. Lewin, "Radiation from discontinuities in stripline," *IEE Proceedings Part C*, vol. 107, pp. 163–170, Feb. 1960.

[53] G.P. Gauthier, A. Courtay, and G.M. Rebeiz, "Microstrip antennas on synthesized low dielectric-constant substrates," *IEEE Trans. on Antennas Propagat.*, vol. 45, no. 8, pp. 1310–1314, Aug. 1997.

[54] D.M. Pozar, "A microstrip antenna aperture coupled to a microstripline," *Electron. Letters*, vol. 21, no. 2, pp. 49–50, Jan. 1985.

[55] P.L. Sullivan and D.H. Schaubert, "Analysis of an aperture coupled microstrip antenna," *IEEE Trans. on Antennas Propagat.*, vol. 34, no. 8, pp. 977–984, Aug. 1986.

[56] J.P. Papapolymerou, R.F. Drayton, and L.P.B. Katehi, "Micromachined patch antennas," *IEEE Trans. on Antennas Propagat.*, vol. 45, no. 2, pp. 275–283, Feb. 1998.

[57] Students' QuickField 3.4 Tera Analysis Co., P.O. Box 571086, Tarzana, CA 91357.

[58] V. Rathi, G. Kumar, and K.P. Ray, "Improved coupling for aperture coupled microstrip antennas," *IEEE Trans. on Antennas Propagat.*, vol. 44, no. 8, pp. 1196–1198, Aug. 1996.

[59] IE3D Version 4 Zeland Software Inc., 39120 Argonaut Way, Suite 499, Fermont, CA 94538.

[60] M. Houdart and C. Aury, "Various excitation of coplanar waveguide," *IEEE-MTT Int. Microwave Symp. Digest*, pp. 116–118, 1979.

[61] G.P. Gauthier, L.P. Katehi, and G.M. Rebeiz, "W-band finite ground coplanar waveguide (FGCPW) to microstrip line transition," *IEEE-MTT Int. Microwave Symp. Digest*, pp. 107–109, 1998.

[62] K.E. Peterson, "Silicon as a mechanical material," *Proceedings of the IEEE*, vol. 70, no. 6, pp. 420–457, May 1982.

[63] R.W. Jackson, "Mode conversion at discontinuities in finite-width conductor-backed coplanar waveguide," *IEEE Trans. on Microwave Theory Tech.*, vol. 37, no. 10, pp. 1582–1589, Oct. 1989.

[64] J.P. Raskin, G.P. Gauthier, L.P. Katehi, and G.M. Rebeiz, "Mode conversion at cpw-to-microstrip transition discontinuities," *submitted to IEEE Trans. on Microwave Theory Tech.*, Sep. 1998.

[65] R.W. Jackson and D.W. Matolak, "Surface-to-surface transition via electromagnetic coupling of coplanar waveguides," *IEEE Trans. on Microwave Theory Tech.*, vol. 35, no. 11, pp. 1027–1032, Nov. 1987.

[66] D. Pavlidis and H.L. Hartnagel, "The design and performance of three-line microstrip couplers," *IEEE Trans. on Microwave Theory Tech.*, vol. 24, no. 10, pp. 631–640, Oct. 1976.

[67] S. Yamamoto, T. Azakami, and K. Itakura, "Coupled strip transmission line with three center conductors," *IEEE Trans. on Microwave Theory Tech.*, vol. 14, no. 10, pp. 446–461, Oct. 1966.

[68] R.J. Wenzel, "Exact design of TEM microwave networks using quarter-wave lines," *IEEE Trans. on Microwave Theory Tech.*, vol. 12, no. 1, pp. 94–111, Jan. 1964.

[69] G. Strauss, P. Ehret, and W. Menzel, "On-wafer measurement of microstrip-based MMIC's," *IEEE-MTT Int. Microwave Symp. Digest*, pp. 1399–1402, 1996.

[70] M.J. Vaughan, R.C. Compton, S. Duncan, D. Tu, and S. Weinreb, "Monolithic, W-band, voltage-controlled oscillator," *IEEE-MTT Int. Microwave Symp. Digest*, pp. 337–340, 1996.

[71] H. Wang, L. Tran, J. Cowles, E. Lin, P. Huang, T. Block, D. Streit, and A. Oki, "Monolithic 77- and 94-GHz InP-based HBT MMIC VCOs," *IEEE-RFIC Symp. Digest*, pp. 91–94, 1997.

[72] A. Bangert, M. Schlechtweg, W. Reinert, W.H. Haydl, A. Hülsmann, and K. Köhler, "Monolithic integrated 75 GHz oscillator with high output power using a pseudomorphic HFET," *IEEE-MTT Int. Microwave Symp. Digest*, pp. 135–138, 1994.

[73] Millitech Corp., "Crash avoidance FLR sensors," *Microwave Journal*, vol. 37, no. 7, pp. 122–126, Jul. 1994.

[74] H. Dämbkes, B. Adelseck, L.P. Schmidt, and J. Schroth, "GaAs MMIC based components and frontends for millimeter-wave communication and sensor systems," *IEEE Microwave Systems Conference Proc.*, pp. 83–86, 1995.

[75] S.S. Gearhart, C.C. Ling, and G.M. Rebeiz, "Integrated millimeter-wave corner-cube antennas," *IEEE Trans. on Antennas Propagat.*, vol. 39, no. 7, pp. 1000–1006, Jul. 1991.

IMAGE EVALUATION
TEST TARGET (QA-3)

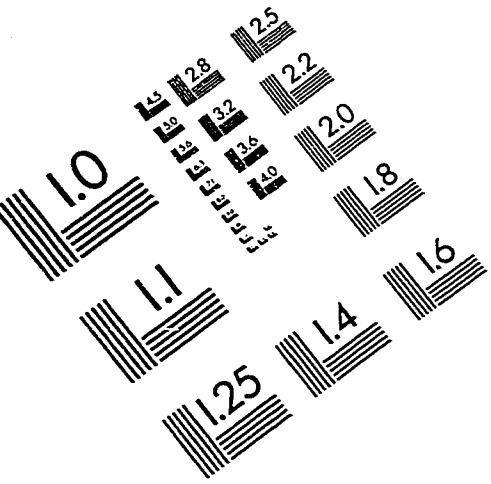

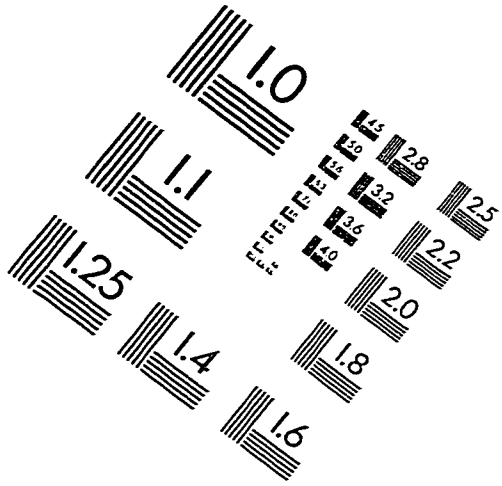

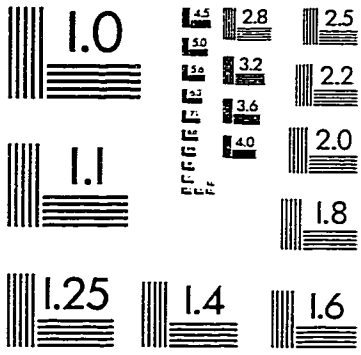

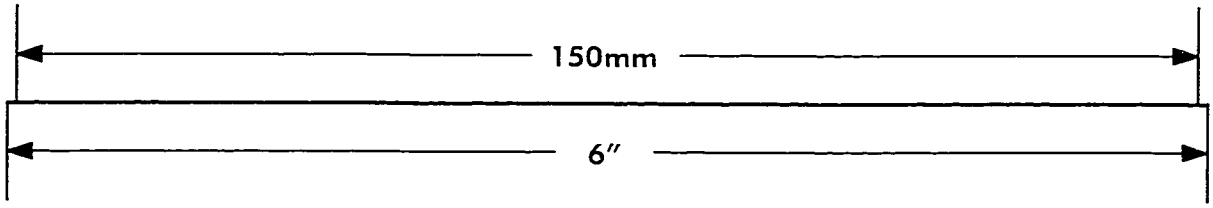

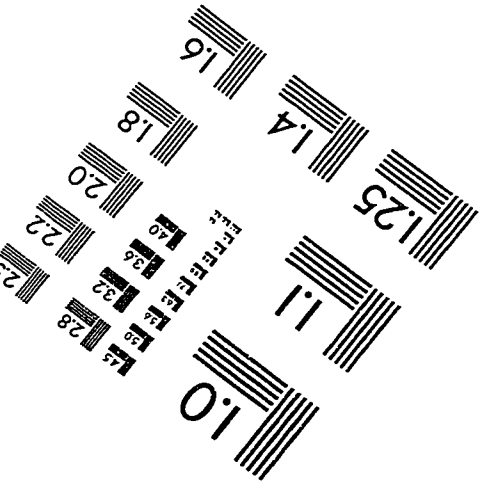

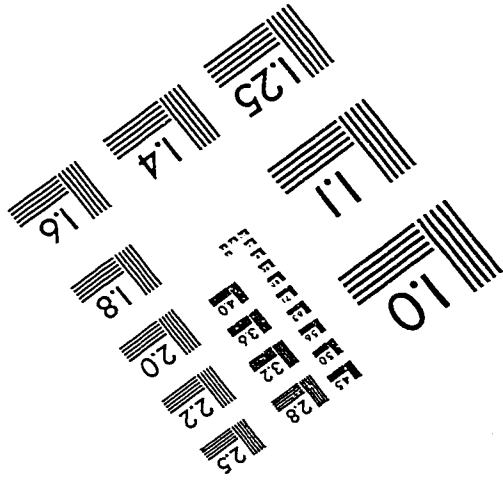

APPLIED IMAGE, Inc
1653 East Main Street
Rochester, NY 14609 USA
Phone: 716/482-0300
Fax: 716/288-5989